International Journal of Biomedical Imaging

# Recent Advances in Molecular Imaging

Guest Editors: Jie Tian, Wenxiang Cong, Jing Bai, Ming Jiang, and Wei Liang

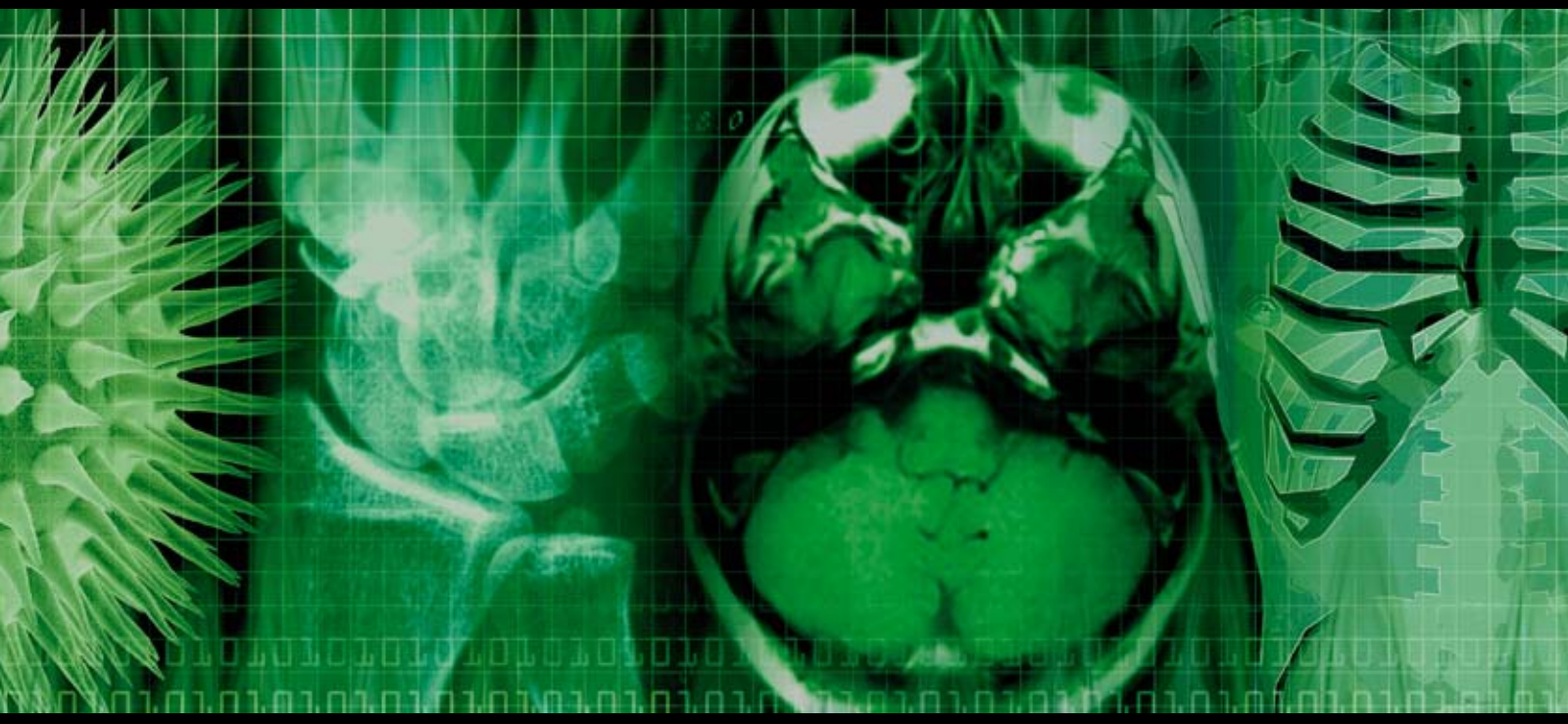

# Recent Advances in Molecular Imaging

International Journal of Biomedical Imaging

# Recent Advances in Molecular Imaging

Guest Editors: Jie Tian, Wenxiang Cong, Jing Bai, Ming Jiang, and Wei Liang

# Contents

**The Advantage of PET and CT Integration in Examination of Lung Tumors**, Guangming Lu, Zhongqiu Wang, Hong Zhu, Linfeng Chang, Yingxin Chen, Jiang Wu, and Yane Zhao
Volume 2007, Article ID 17131, 5 pages

Hindawi Publishing Corporation
International Journal of Biomedical Imaging
Volume 2007, Article ID 73198, 1 page
doi:10.1155/2007/73198

# *Editorial*
# Recent Advances in Molecular Imaging

**Jie Tian,[1,2] Wenxiang Cong,[3] Jing Bai,[4] Ming Jiang,[3,5] and Wei Liang[6]**

[1] *Institute of Automation, Chinese Academy of Sciences, Beijing 100080, China*
[2] *Life Science Center, Xidian University, Xian, Shaanxi 710071, China*
[3] *Biomedical Imaging Division, VT-WFU School of Biomedical Engineering and Sciences, Virginia Polytechnic Institute & State University, Blacksburg, VA 24061, USA*
[4] *Department of Biomedical Engineering, Tsinghua University, Beijing 100084, China*
[5] *LMAM, School of Mathematical Sciences, Peking University, Beijing 100871, China*
[6] *Institute of Biophysics, Chinese Academy of Sciences, Beijing 100101, China*

Received 1 October 2007; Accepted 1 October 2007



Molecular imaging is a newly emerging and rapidly developing biomedical imaging field in which the modern tools are being married to depict noninvasive in vivo cellular and molecular processes sensitively and specifically, such as monitoring multiple molecular events, cell trafficking and targeting. The goals of this field are to develop technologies and instruments for studying biological and medical processes as well as diagnosing and managing diseases better. Although rapid progress in the fundamentals and applications make molecular imaging become an important tool for biomedical research in recent years, many difficult problems and challenges remain. Discussing the problems and challenges in detail and illustrating recent progress and future direction, the special issue collects the high-quality, peer-reviewed, original research papers in the area of molecular imaging.

Novel molecular imaging theories and algorithms, new molecular probes, multimodality molecular imaging prototype systems and experiments, and final clinical applications are introduced mainly in this special issue. In molecular imaging theories and algorithms, genetic algorithm-based optimization tool is used to improve the accuracy of the diffusion model in strongly absorbing media by adjusting the optical parameters. Furthermore, a penalized linear and nonlinear combined conjugate gradient method, a fast preiteration algorithm based on the generalized inverse matrix, and a Monte-Carlo-based network method are also proposed for light source reconstruction in optical tomography. Considering the importance of molecular probes, synthesis and bioconjugation of gold nanoparticles as potential molecular probes for light-based imaging techniques are described in this special issue, and the nitroimidazole-based thioflavin-T derivatives as cerebral ischemia markers are evaluated in vivo. In order to test the feasibility and effectiveness of imaging theories, algorithms and probes, molecular imaging prototype systems should be designed, constructed and employed for small animal or phantom imaging. Thus, multimodality fusion near-infrared optical tomography Systems with highly sensitive CCD camera and photomultiplier tube can be consulted respectively in this special issue. Furthermore, a novel confocal optical system design and a dual laser confocal scanner have been developed for molecular imaging applications of biochip. In clinical applications, the advantage of PET and CT integration in examination of lung tumors is analyzed. Moreover, several innovative processing methods of molecular image are also presented in this special issue. In conclusion, this special issue covers recent important advances in molecular imaging field.

## ACKNOWLEDGMENTS

This work is supported in part by the NBRPC under Grant 2006CB705700, PCSIRT (IRT0645), and CAS Hundred Talents Program. The editors of this special issue express their sincere thanks to the contributing authors and reviewers for making this publication possible and successful.

*Jie Tian*
*Wenxiang Cong*
*Jing Bai*
*Ming Jiang*
*Wei Liang*

Hindawi Publishing Corporation
International Journal of Biomedical Imaging
Volume 2007, Article ID 38168, 6 pages
doi:10.1155/2007/38168

*Research Article*

# Improving the Accuracy of the Diffusion Model in Highly Absorbing Media

**Alexander X. Cong, Haiou Shen, Wenxiang Cong, and Ge Wang**

*Biomedical Imaging Division, School of Biomedical Engineering and Sciences,*
*Virginia Polytechnic Institute and State University, 1880 Pratt Drive, Blacksburg, VA 24061, USA*

Received 14 April 2007; Accepted 28 June 2007

Recommended by Wei Liang

The diffusion approximation of the Boltzmann transport equation is most commonly used for describing the photon propagation in turbid media. It produces satisfactory results in weakly absorbing and highly scattering media, but the accuracy lessens with the decreasing albedo. In this paper, we presented a method to improve the accuracy of the diffusion model in strongly absorbing media by adjusting the optical parameters. Genetic algorithm-based optimization tool is used to find the optimal optical parameters. The diffusion model behaves more closely to the physical model with the actual optical parameters substituted by the optimized optical parameters. The effectiveness of the proposed technique was demonstrated by the numerical experiments using the Monte Carlo simulation data as measurements.



## 1. INTRODUCTION

The optical tomography techniques such as bioluminescence tomography (BLT), fluorescent tomography (FMT), and diffusion optical tomography (DOT) have attracted increasing research attentions in recent years. One of the common core issues of optical imaging modalities is how to model the light propergation in biological tissues properly. Monte Carlo simulation, which has numerous successful applications in other fields, was introduced to study the light interaction with tissue [1, 2]. Although it is a rigorous model for forward problem of photon transport [2], due to its stochastic nature, the excessive computational requirement makes it an improper choice for inverse problems. On the other hand, the Boltzmann transport equation is able to model the photon propergation deterministicly and accurately in tissue [3], but it too has a high computational complexity. Several methods were proposed to solve the transport equation, such as discrete ordinates [4, 5] and spherical harmonics expansion [6], but applying transport equation in 3D remains challenging in pratice. To reduce the complexity, diffusion approximation (DA) was introduced and widely applied as a photon propergation model in various optical tomography modalities [7–9]. DA is computationally efficient and almost as accurate as the transport equation in weakly absorbing media. Unfortunately, for albedos $\mu_s'/\mu_a < 10$, DA is no longer able to describe the photon propagation accurately [10, 11]. The relatively strong photon absorptions are often resulted from the shorter wavelength of the broad emission spectrum of a reporter gene, such as the luciferase used in BLT, which has emission peaks between 538 to 570 nm [12]. It was reported that performing BLT at a shorter wavelength helps to reduce the ill posedness of the reconstruction [11]. Therefore, it is important that photon propagation in strongly absorbing media could be modeled.

In this paper, we proposed an optical parameter adjustment technique to alleviate the inaccuracy of DA in highly absorbing media. In our approach, we make the diffusion model adjustable in the sense that the optical parameters, which are usually considered as the known properties, are interpreted as variables. The accuracy of the model is no longer solely controlled by the formulation of DA, but also by the adjustable optical parameters. The optical parameters that minimize the error between the solution of DA and the simulated MC data make the model more accurate than use the intrinsic optical properties directly. This technique is discussed in Section 2.

## 2. SIMULATION METHODS

In this section, we give a brief overview of the two simulation methods used in the numerical studies: the Monte

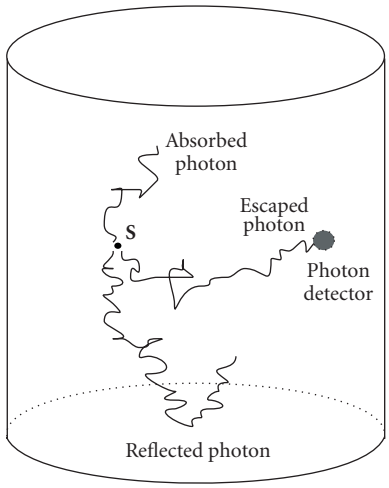


Figure 1: The Monte Carlo process of photon propagation in tissue.

Carlo simulation and the finite element solution of the diffusion equation, and discuss the optical parameters adjustment technique.

### 2.1. Monte Carlo simulation

Monte Carlo (MC) simulation models each individual photon's physical interactions with the medium as a stochastic process. As a large number of such stochastic processes of photon propagation are simulated, the signal detected is statistically meaningful and very close to the physical experiment counterpart. MC result can be legitimately considered as the low-noise version of the actual physical measurement. Therefore, we use MC method to produce measurements in numerical experiments. The Monte Carlo process consists of three parts: the photon absorption, the photon scattering and the internal reflection at the boundaries, as illustrated in Figure 1. The absorption of photon for each step can be expressed by [2, 3, 13]

$$\Delta W = \frac{\mu_a}{\mu_a + \mu_s} W, \tag{1}$$

where $W$ is the weight of the photon packet. The scattering of the photon is governed by Henyey-Greenstein (HG) phase function, which is considered as the most appropriate phase function for the photon propergation in tissue. The HG phase function is given by [2, 3]

$$p(\cos\,\theta) = \frac{1 - g^2}{2\left(1 + g^2 - 2g\cos\theta\right)^{3/2}}, \tag{2}$$

where $\theta$ is the deflection angle, and $g$ the anisotropy. The internal reflectance rate due to the refrective index mismatch at the tissue boundary for unpolarized incident light is given by the Fresnel's formulas [2, 3]:

$$R(\vartheta_i) = \frac{1}{2}\left[\frac{\sin^2(\vartheta_i - \vartheta_t)}{\sin^2(\vartheta_i + \vartheta_t)} + \frac{\tan^2(\vartheta_i - \vartheta_t)}{\tan^2(\vartheta_i + \vartheta_t)}\right], \tag{3}$$

where $\vartheta_i$ and $\vartheta_t$ are the incident and transmit angles, respectively. The incident and transmit angles obey the Snell's law

$$\frac{\sin\vartheta_i}{\sin\vartheta_t} = \frac{n_t}{n_i}, \tag{4}$$

where $n_i$ and $n_t$ are the refractive indices for both sides of the boundary, respectively.

We programmed MCsim [14], a Monte Carlo simulator, for the photon propagation for the numerical experiment. Our MC simulator can handle several types of 3D geometrical phantoms such as cylinders and ellipsoids. By combining cylinders and ellipsoids, which can represent different mouse organs, the heterogeneous phantom mimicking the real mouse is created. The MC simulation based on such heterogeneous numerical phantom is similar to the in vivo mouse experiment. The efficiency of the MC simulation is enhanced through the parallel computing and fast random array generateration.

### 2.2. Diffusion model

The transport equation accurately characterizes the photon propergation in biological tissue. Due to its complexity in 3D, the diffusion approximation of the transport equation is often used instead in tissue with high albedo. The diffusion equation in steady state is given by [3, 8]

$$-\nabla\cdot\left(D(\mathbf{r})\nabla\phi(\mathbf{r})\right) + \mu_a\phi(\mathbf{r}) = S(\mathbf{r}), \quad \mathbf{r}\in\Omega \tag{5}$$

and the Robin boundary condition is applied [8, 15]:

$$\phi(\mathbf{r}) + 2\Theta(\mathbf{r})D(\mathbf{r})\mathbf{n}\cdot\nabla\phi(\mathbf{r}) = 0, \quad \mathbf{r}\in\partial\Omega, \tag{6}$$

where $\mathbf{r}$ is the position vector, $\phi$ the photon fluence, $S$ the source power density, $\Omega$ the internal region, $\mathbf{n}$ the normal to the boundary $\partial\Omega$, and $\Theta$ the boundary mismatch factor, which is given by $(1+R)/(1-R)$, and $R$ can be approximated by $R \approx -1.4399n_i^{-2} + 0.7099n_i^{-1} + 0.6681 + 0.0636n_i$ [16]. $\mu_a$ and $D$ are the absorption and diffusion coefficient, respectively. $D$ can be decomposed to the expression of $\mu_a$ and the reduced scattering coefficient $\mu_s'$:

$$D = \frac{1}{3\left(\mu_a + \mu_s'\right)}. \tag{7}$$

To solve the diffusion equation, we apply the finite element method and transform the problem into a system of discrete linear equations [8]

$$\mathbf{A}\phi = \mathbf{S}, \tag{8}$$

where $\mathbf{A}$ is the weight matrix and $\mathbf{S}$ the source power distribution vector. We take the boundary fluence $\phi(\mathbf{r})$, $\mathbf{r}\in\partial\Omega$ as measurement to compare with the MC simulated measurement.

### 2.3. Optical parameters adjustment

The simulation of photon progation in tissue not only requires an appropriate model, the optical parameters $\mu_a$ and

$\mu_s'$ also play an important role. As we mentioned before, the diffusion model that uses the tissue's intrinsic optical properties as optical parameters is not suitable to describe the photon propagation in strongly absorbing media. However, in pratice we are often only interested in how the photons propagate in tissue without noticing the optical parameters used. For example, the BLT and FMT focus on the reconstruction of the light source distribution. Thus, the optical parameters can be taken as variables to improve the accuracy of the DA model. In this perspective, the accuracy improvement task becomes a typical parameter estimation problem: finding the best parameters that minimize the error of DA at the surface. Therefore, by optimizing the optical parameters, the solution of DA may fit the real measurement better and consequently improve the accuracy of the model.

Before we can find the optimal optical parameters, we first define the error metric, which is simply the average of the relative errors

$$\varepsilon(\mu_a, \mu_s') = \frac{\sum_d |(\phi - \phi')/\phi|}{n_d}, \tag{9}$$

where $\varepsilon$ represents the error, $\phi$ the MC simulated power density (i.e., fluence) at a detector, $\phi'$ the diffusion model finite element solution of surface power densities at each detector, $d$ the detectors, and $n_d$ the number of detectors. This simple error metric evenly weights the strong and weak signals, therefore, the optimization result does not depend on the location of the light source.

It is clear that the error $\varepsilon$ can be expressed as a function of the optical parameters $\mu_a$ and $\mu_s'$. The optimal optical parameters are found by minimizing the error, as in the following equation:

$$\{\mu_a^{\text{adj}}, \mu_s'^{\text{adj}}\} = \arg\min_{\mu_a, \mu_s'} |\varepsilon(\mu_a, \mu_s')|. \tag{10}$$

To solve this parameter estimation in (10), we use a genetic algorithm (GA). The major advantages of GA over the deterministic gradient methods are the initial values have very little impact on the optimization result, and the solution will not trapped in a local optima [17]. Although there is no way to know if GA reaches the exact global optima, this stochastic optimization method always produces a sufficiently good solution if a large number of generations (i.e., iterations) and a proper population size are applied. The optimized optical parameters $\mu_a^{\text{adj}}$ and $\mu_s'^{\text{adj}}$ help to improve the accuracy of the diffusion equation (5), as shown in Section 3.

## 3. NUMERICAL EXPERIMENTS AND RESULTS

### 3.1. Optical parameter optimization

We performed the optical parameter optimization on a sphere with 7 mm radius. In Cartesian coordinate, the center of the sphere was the origin. In order to obtain the finite element-based solution of diffusion approximation (DA), the sphere was discretized into 5539 nodes and 28 607 tetrahedra. For the convenience of comparing MC simulation data with the finite element solution of DA, all 1452 surface nodes were used as detectors. For the Monte Carlo simulation, each detector integrated the escaping photons within 0.7 mm radius, while the solution of DA was produced directly at each surface node. The measurement was normalized and served as a description of the boundary power distribution rather than the actual power density.

Table 1: GA configration parameters.

| | |
|---|---|
| Population size | 50 |
| Penerations | 200 |
| Crossover rate | 80% |
| Mutation rate | 10% |
| Elitism | best 2 |

Table 2: Optical parameters optimization results. The unit was in $\text{mm}^{-1}$.

| $\mu_a$ | $\mu_s'$ | $\mu_a^{\text{adj}}$ | $\mu_s'^{\text{adj}}$ |
|---|---|---|---|
| 0.20 | 1.05 | 0.375366 | 0.213276 |
| 0.35 | 1.05 | 0.423532 | 0.453873 |

We placed a single isotropic point source 1 mm away from the origin, and set the source power to 0.313 picowatt, which is equal to the energy of a million photons per second under 635 nm wavelength. At this source location, we performed the optical parameter adjustment for two media: medium one had $\mu_a = 0.2\,\text{mm}^{-1}$ and medium two had $\mu_a = 0.35\,\text{mm}^{-1}$, the $\mu_s' = 1.05\,\text{mm}^{-1}$ and the tissue refractive indices are 1.37 for both materials. The albedo of these two media were 5.25 and 3, respectively. We expected that the solutions of DA would have noticeable inaccuracy in these media. We used the genetic algorithm toolbox (*gatool*) in MATLAB to solve (10). The important parameters used in GA are listed in Table 1.

The resultant optimal optical parameters are listed in Table 2.

### 3.2. Accuracy improvement results

Using the optimized parameters in Table 2, the results of the accuracy improvements of DA are plotted in Figures 2 and 3, with respect to the two media.

We tested the effectiveness of the optimized optical parameters by solving the DA with different light source locations in the sphere. The accuracy enhancement results regarding different light source locations are listed in Table 3. The error metric in Table 3 was according to (9). The results show that the accuracy improvement effect was stable for different light source locations, and has little dependency on the location of the light source where the optical parameter optimization was performed.

To further test the effectiveness of the proposed method, we constructed a heterogeneous phantom, as in Figure 4. The outer cylinder had a height of 20 mm and a radius of 10 mm. The geometrical center of the cylinder was at the origin. The inner sphere had a radius of 4 mm and its geometrical center was 2 mm away from the origin along the $x$-axis. The absorption coefficient of the cylinder and the sphere were 0.2

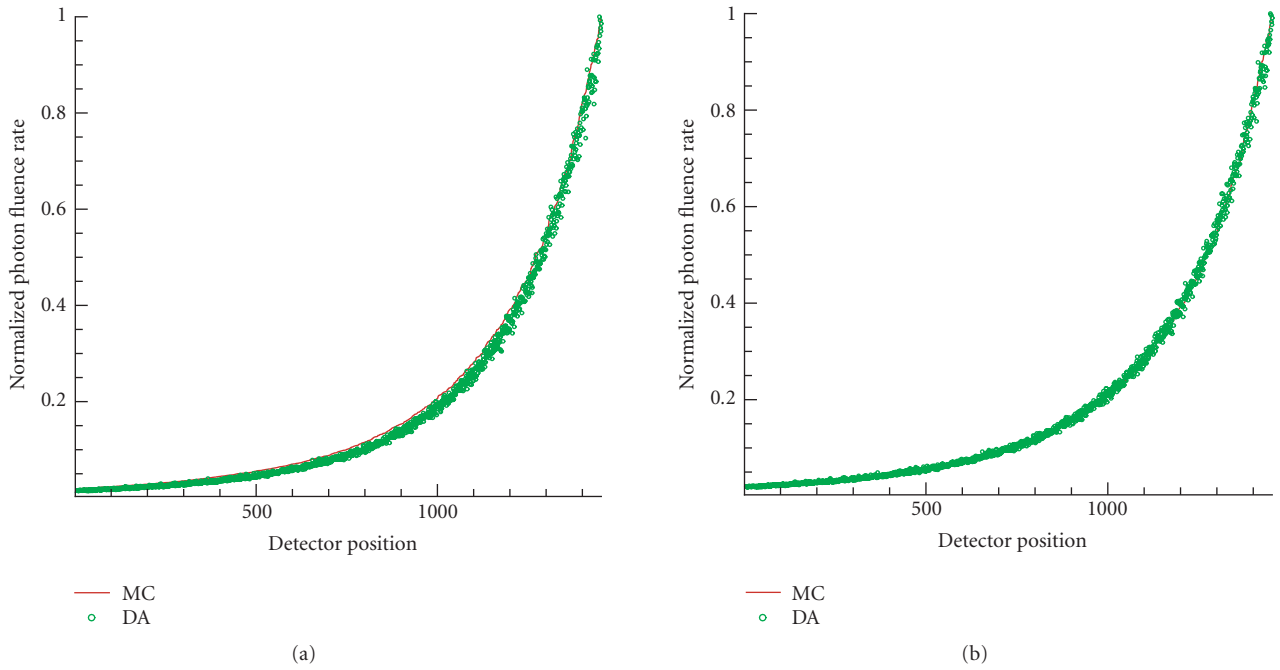


Figure 2: The comparison between solutions of DA using the the unadjusted and the optimal optical parameters in a medium with $\mu_a = 0.2\,\text{mm}^{-1}$ and $\mu_s' = 1.05\,\text{mm}^{-1}$. The light source was 1 mm from the origin. (a) Solution of DA with unadjusted optical parameters versus MC data. (b) Solution of DA with optimized optical parameters versus MC data. The detector positions were sorted in the increasing order of the fluence rate of MC data.

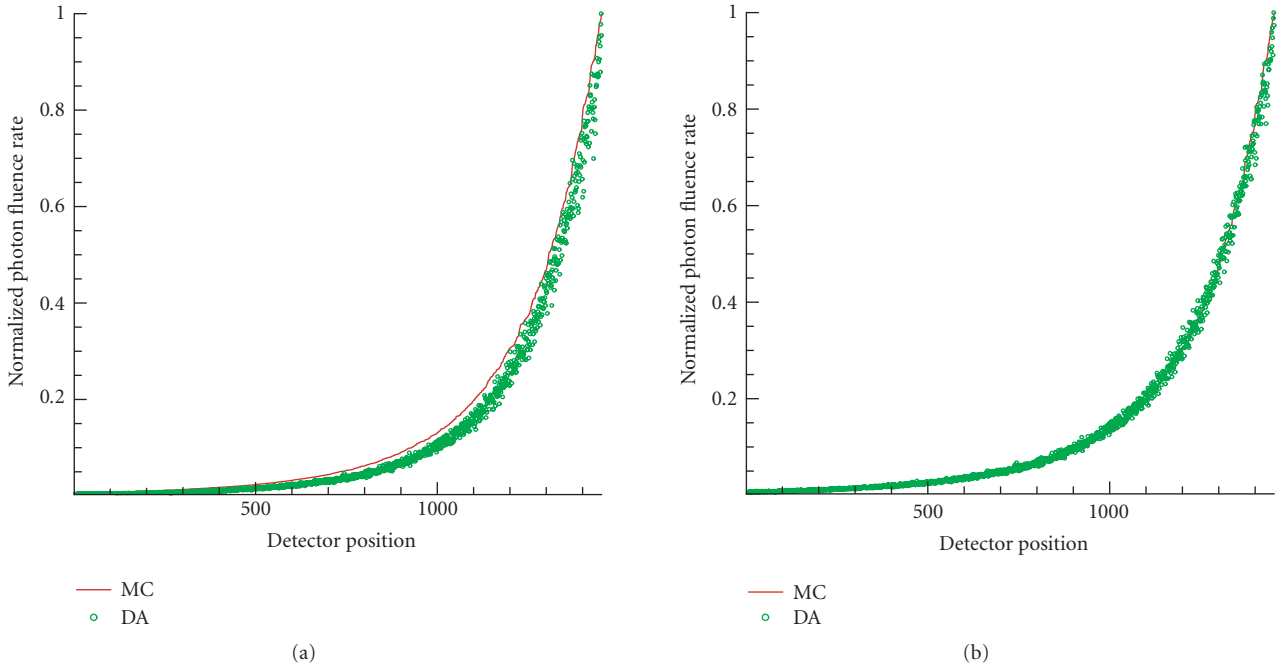


Figure 3: The comparison between solutions of DA using the the unadjusted and the optimal optical parameters in a medium with $\mu_a = 0.35\,\text{mm}^{-1}$ and $\mu_s' = 1.05\,\text{mm}^{-1}$. The light source was 1 mm from the origin. (a) Solution of DA with unadjusted optical parameters versus MC data. (b) Solution of DA with optimized optical parameters versus MC data. The detector positions were sorted in the increasing order of the fluence rate of MC data.

Table 3: Accuracy improvements of DA regarding to different light source locations. $d$ is the distance from the origin, $\varepsilon$ the error without optical parameter optimization, and $\varepsilon^{\text{adj}}$ the improved error.

| $d$ (mm) | $\mu_a = 0.2\,\text{mm}^{-1}$ | | $\mu_a = 0.35\,\text{mm}^{-1}$ | |
|---|---|---|---|---|
| | $\varepsilon$ | $\varepsilon^{\text{adj}}$ | $\varepsilon$ | $\varepsilon^{\text{adj}}$ |
| 1 | 0.09 | 0.0406 | 0.2361 | 0.0766 |
| 2 | 0.1665 | 0.1008 | 0.3801 | 0.1393 |
| 3 | 0.3151 | 0.1066 | 0.5784 | 0.14 |
| 4 | 0.3944 | 0.1074 | 0.6558 | 0.1183 |
| 5 | 0.373 | 0.0947 | 0.6567 | 0.1608 |

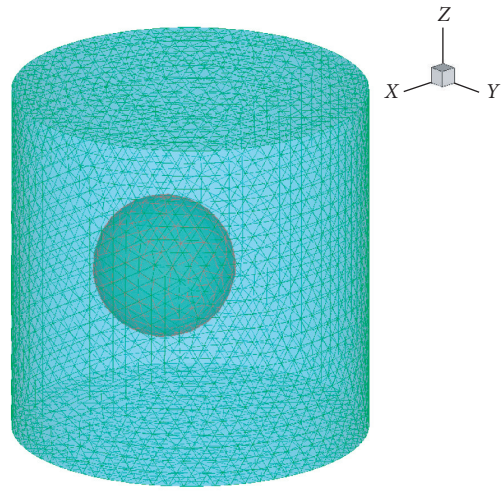


Figure 4: The finite element model of the heterogeneous phantom.

and 0.35 $\text{mm}^{-1}$, respectively. The reduced scattering coefficients were 1.05 $\text{mm}^{-1}$ and the refractive indices were 1.37 for both media. The light source was placed at the center of the sphere. Using the optimized optical parameter in Table 2, the error was reduced from 0.3951 to 0.2201.

## 4. DISCUSSION AND CONCLUSIONS

We have present a technique for improving the accuracy of the diffusion model by adjusting optical parameters. Instead of using the accurate tissue optical parameters to produce inaccurate result in highly absorbing media, the optimized optical parameters give better accuracy in such media. GA is used for parameter optimization, which effectively avoid the solution to be trapped in a local optima. Our simulation results show significant error reduction for media with different photon absorptions, and the results have little dependency on the light source location. If the actual optical parameters of the medium are known, the Monte Carlo simulation could generate the measurement data as if obtained from the physical phantom or real mouse experiment, so that the optical parameters optimization technique can be performed purely numerically. In the case that the optical properities are unknown, the proposed technique still applies by replacing the Monte Carlo simulation by the actual physical experiment. However, we emphasize that even though the accuracy of the normalized power distribution is improved with this technique, the solution of DA using the optimized optical parameters does not reflect the actual power. Thus, the calibration process is required to convert the normalized power distribution to the actual power. The optical parameter optimization technique permits diffusion model to work under highly absorption media, so that DA works well over a wider range of applications. For the the in vivo optical tomography such as BLT and FMT, the DA photon propagation model for each mouse organ or tissue is improved numerically prior to the reconstruction, the reconstruction algorithm based on the improved DA model is expected to have improved source localization and intensity accuracy.

## ACKNOWLEDGMENT

This work was supported by the National Institutes of Health under Grants EB001685 and EB006036.

## REFERENCES

[1] S. R. Arridge and J. C. Hebden, "Optical imaging in medicine—II: modelling and reconstruction," *Physics in Medicine and Biology*, vol. 42, no. 5, pp. 841–853, 1997.

[2] L. Wang, S. L. Jacques, and L. Zheng, "MCML—Monte Carlo modeling of light transport in multi-layered tissues," *Computer Methods and Programs in Biomedicine*, vol. 47, no. 2, pp. 131–146, 1995.

[3] A. J. Welch and M. J. C. van Gemert, Eds., *Optical-Thermal Response of Laser-Irradiated Tissue*, Plenum Press, New York, NY, USA, 1995.

[4] G. S. Abdoulaev and A. H. Hielscher, "Three-dimensional optical tomography with the equation of radiative transfer," *Journal of Electronic Imaging*, vol. 12, no. 4, pp. 594–601, 2003.

[5] T. Tarvainen, M. Vauhkonen, V. Kolehmainen, and J. P. Kaipio, "Finite element model for the coupled radiative transfer equation and diffusion approximation," *International Journal for Numerical Methods in Engineering*, vol. 65, no. 3, pp. 383–405, 2006.

[6] A. D. Klose and E. W. Larsen, "Light transport in biological tissue based on the simplified spherical harmonics equations," *Journal of Computational Physics*, vol. 220, no. 1, pp. 441–470, 2006.

[7] S. R. Arridge, "Optical tomography in medical imaging," *Inverse Problems*, vol. 15, no. 2, pp. R41–R49, 1999.

[8] W. Cong, G. Wang, D. Kumar, et al., "Practical reconstruction method for bioluminescence tomography," *Optics Express*, vol. 13, no. 18, pp. 6756–6771, 2005.

[9] A. X. Cong and G. Wang, "A finite-element-based reconstruction method for 3D fluorescence tomography," *Optics Express*, vol. 13, no. 24, pp. 9847–9857, 2005.

[10] T. Durduran, A. G. Yodh, B. Chance, and D. A. Boas, "Does the photon-diffusion coefficient depend on absorption?" *Journal of the Optical Society of America A*, vol. 14, no. 12, pp. 3358–3365, 1997.

[11] A. D. Klose, "Transport-theory-based stochastic image reconstruction of bioluminescent sources," *Journal of the Optical Society of America A*, vol. 24, no. 6, pp. 1601–1608, 2007.

[12] B. W. Rice, M. D. Cable, and M. B. Nelson, "In vivo imaging of light-emitting probes," *Journal of Biomedical Optics*, vol. 6, no. 4, pp. 432–440, 2001.

[13] M. Testorf, U. Österberg, B. Pogue, and K. Paulsen, "Sampling of time- and frequency-domain signals in Monte Carlo simulations of photon migration," *Applied Optics*, vol. 38, no. 1, pp. 236–245, 1999.

[14] MCsim, http://alexcong.googlepages.com/resouces.

[15] B. W. Pogue, S. Geimer, T. O. McBride, S. Jiang, U. L. Österberg, and K. D. Paulsen, "Three-dimensional simulation of near-infrared diffusion in tissue: boundary condition and geometry analysis for finite-element image reconstruction," *Applied Optics*, vol. 40, no. 4, pp. 588–600, 2001.

[16] M. Schweiger, S. R. Arridge, M. Hiraoka, and D. T. Delpy, "The finite element method for the propagation of light in scattering media: boundary and source conditions," *Medical Physics*, vol. 22, no. 11, pp. 1779–1792, 1995.

[17] K. F. Man, K. S. Tang, and S. Kwong, "Genetic algorithms: concepts and applications [in engineering design]," *IEEE Transactions on Industrial Electronics*, vol. 43, no. 5, pp. 519–534, 1996.

Hindawi Publishing Corporation
International Journal of Biomedical Imaging
Volume 2007, Article ID 23219, 6 pages
doi:10.1155/2007/23219

*Research Article*

# A Fast Reconstruction Algorithm for Fluorescence Optical Diffusion Tomography Based on Preiteration

**Xiaolei Song,[1] Xiaoyun Xiong,[2] and Jing Bai[1]**

[1] *Department of Biomedical Engineering, Tsinghua University, Beijing 100084, China*
[2] *Department 2, College of Electronic Engineering, University of Electronic Science and Technology of China, Chengdu, Sichuan 610054, China*

Received 12 October 2006; Accepted 12 February 2007

Recommended by Jie Tian

Fluorescence optical diffusion tomography in the near-infrared (NIR) bandwidth is considered to be one of the most promising ways for noninvasive molecular-based imaging. Many reconstructive approaches to it utilize iterative methods for data inversion. However, they are time-consuming and they are far from meeting the real-time imaging demands. In this work, a fast preiteration algorithm based on the generalized inverse matrix is proposed. This method needs only one step of matrix-vector multiplication online, by pushing the iteration process to be executed offline. In the preiteration process, the second-order iterative format is employed to exponentially accelerate the convergence. Simulations based on an analytical diffusion model show that the distribution of fluorescent yield can be well estimated by this algorithm and the reconstructed speed is remarkably increased.



## 1. INTRODUCTION

With the discovery of biocompatible, specific fluorescent probes and the development of imaging technologies, the potential of fluorescence tomography as a means for molecularly based noninvasive imaging of biological tissues has received in recent years increased attention [1–3]. Fluorescent beacons emitting in the near-infrared (NIR) bandwidth are always preferred, since hemoglobin and water absorb minimally in this spectral window so as to allow photons to penetrate for several centimeters in tissues [4].

Using preferentially accumulated fluorescent probes as indicators or contrast agents, fluorescence optical diffusion tomography (FODT) is performed by launching light at the probes' excitation wavelength into the tissue. The fluorescent beacon absorbs the incident light, and emits light at a longer wavelength when it drops to the ground state. Then the emission is measured by an array of detection devices at the surface of the body. However, as the strong diffusion of NIR in biological tissues, reconstruction of very large unknown inside characteristics from the limited detected data at the boundary is one of the main difficulties in FODT. Many reconstructive approaches utilize iterative methods for data inversion, such as the algebraic reconstruction technique (ART) [5], Newton's or Newton-type optimization methods [6, 7], and Bayesian nonlinear least-square method [8, 9]. They are always time-consuming and far from meeting the real-time imaging demands.

In this study, a fast algorithm based on the preiteration is applied to the inversion process of fluorescence tomography. For simulating the photon's propagation in tissues with fluorescent beacons inside, a previously reported DPDW model based on Born approximation is simply introduced at the beginning. Then, the preiteration fast algorithms are presented in detail, emphasizing the second-order method. After that, the simulation using the second-order form is investigated and the results are shown. Finally, we analyze the computation burden and convergence property of the second-order iteration form and give the conclusion.

## 2. DPDW MODEL

Often a couple of diffusion equations in frequency-domain is employed to describe the propagation of both excited light and fluorescent light in diffusive medium, that is [6, 7, 10]

$$\nabla\left[D_x(\mathbf{r})\nabla\Phi_x(\mathbf{r},\omega)\right] - \left[\mu_{a_x}(\mathbf{r}) + \frac{j\omega}{c}\right]\Phi_x(\mathbf{r},w) = -\delta(\mathbf{r}-\mathbf{r}_{s_k}),$$

$$\nabla\left[D_m(\mathbf{r})\nabla\Phi_m(\mathbf{r},\omega)\right]-\left[\mu_{a_m}(\mathbf{r})+\frac{j\omega}{c}\right]\Phi_m(\mathbf{r},w)$$
$$=-\Phi_x(\mathbf{r},\omega)\eta(\mathbf{r})\frac{1-j\omega\tau(\mathbf{r})}{1+\left[\omega\tau(\mathbf{r})\right]^2}, \tag{1}$$

where $\Phi_{x,m}$ is the photon density for excitation (subscript $x$) or fluorescent light (subscript $m$), $D_{x,m}(\mathbf{r})$ is the diffusion coefficient, and $\mu_{a_{x,m}}(\mathbf{r})$ is the absorption coefficient. Based on this model, the fluorescence lifetime $\tau(\mathbf{r})$ and the yield $\eta(\mathbf{r})$ can be estimated through the boundary measurements. Equation (1) can be solved by analytical or numerical methods. In this paper, we use an analytical model of Born approximation for specific medium geometry to demonstrate the inversion algorithm. In fact, the fast algorithm could also be applied to arbitrary geometries, where the model is discretized by numerical methods [7, 10] or the Kirchhoff approximation [5].

In the frequency-domain model, an amplitude-modulated incident point source of photons into a diffusive medium produces a diffuse photon density wave (DPDW) [11–13]. Let an intensity-modulated point source of amplitude $\Theta_0$ be located at $\mathbf{r}_s$ in a homogeneous infinite medium. Then the spatial part of the originating DPDW at position $\mathbf{r}$ is [11] $U_0(\mathbf{r}_s-\mathbf{r},k)=\Theta_0\exp[ik(\mathbf{r}_s-\vec{r})]/[4\pi D(\mathbf{r}_s-\mathbf{r})]$, with the wave number $k=[(-\nu\mu_a+i\omega)/D]^{1/2}$, and $D=\nu/3\mu_s'$ is the diffusion coefficient with the reduced scattering coefficient $\mu_s'$ and the speed of light in the medium $\nu$. Here, $\omega$ is the angular modulation frequency of the source. Treating fluorescent beacons as two-level quantum systems and assuming that there are no saturation or photon quenching effects, the fluorescent photon density $\delta u_{fl}$, measured at a detector position $r_{di}$ due to a localized probe with volume $d^3r_k$ embedded within the medium, is [11]

$$\delta u_{fl}(\mathbf{r}_k,\mathbf{r}_{sj},\mathbf{r}_{di})$$
$$=U_0(\mathbf{r}_{sj}-\mathbf{r}_k,k^{\lambda_1})\frac{\eta(\mathbf{r}_k)}{1-i\omega\tau(\mathbf{r}_k)}\frac{\nu}{D^{\lambda_2}}G(\mathbf{r}_{di}-\mathbf{r}_k,k^{\lambda_2})d^3r_k, \tag{2}$$

with the excited source at $\mathbf{r}_{sj}$. Here, $\lambda_1$ and $\lambda_2$ represent the excited light wavelength and the fluorescent wavelength in the near-infrared section, respectively. $G(\mathbf{r}_d-\mathbf{r},k^{\lambda_2})=\exp(ik^{\lambda 2}|\mathbf{r}_d-\mathbf{r}|)/4\pi|\mathbf{r}_d-\mathbf{r}|$ is Green's function solution to the diffusion equation and represents the variance of fluorescent DPDW from fluorescent probe to the detector.

For a weakly absorbing spatial distribution of fluorescent probes, the detected fluorescent DPDW at $\mathbf{r}_{di}$ can be found by integrating overall fluorescent sources [11, 12]. In the reconstruction, for the measurement at positions $\mathbf{r}_{di}$ $(i=1,2,\ldots,M_i)$, the integral can be digitized as

$$U_{fl}(\mathbf{r}_{sj},\mathbf{r}_{di})=\sum_{l=1}^{N}\delta u_{fl}(\mathbf{r}_l,\mathbf{r}_{sj},\mathbf{r}_{di})d^3r_l \tag{3}$$

due to the sources $r_{sj}$ $(j=1,2,\ldots,M_j)$. As only one of the sources is working at a time, the total number of measurements is $M=M_i\times M_j$. In fluorescence tomography, continuous-wave (CW) mode is always chosen, that is, $\omega=0$, and only $\eta$ is reconstructed. Then substituting (2) in (3) will lead to the following matrix equation:

$$U=AX, \tag{4}$$

where $U$ represents an $M\times 1$ column vector of the detected data, $X$ is a column vector of unknown values of fluorescent yield $\eta$ at $N$ reconstructed points, and matrix $A$ indicates the obtained $M\times N$ weighted coefficients.

## 3. PREITERATION INVERSE ALGORITHM

As in FODT, the inside reconstructed points number $N$ is always much bigger than $M$, the measurement number at the boundary, the equation series (4) is always ill-posed and indefinite. In this case, the direct inverse matrix of $A$ does not exist. However, its generalized inverse can be employed to solve (4).

### 3.1. Preiteration algorithm based on generalized inverse

If the Moore-Penrose inverse of $A$ exists and is known as $A^+$, the unique solution of (4) which has the minimum norm and the least square can be obtained simply by [14]

$$X=A^+U. \tag{5}$$

There are several direct methods to calculate the generalized inverse $A^+$, for example, regularized SVD method. However, the iterative method is always preferred in computerized calculation, especially for large datasets, as it is easy to be programed and occupies much less ram than direct methods.

Supposing the residual error series $\hat{R}_k=I-A\hat{S}_k$ ($I$ is the unit matrix of $M\times M$), series

$$\hat{S}_{k+1}=\hat{S}_k+S_0(I-A\hat{S}_k) \tag{6}$$

will be convergent to $A^+$ when $k\to\infty$ [14]. Here $S_0$ can be chosen as $\alpha A^T$ [15], with $\alpha=1/\lambda_{\max}$. And $\lambda_{\max}$ is the maximum eigenvalue of $A\cdot A^T$, where $A^T$ is the transposed matrix of $A$.

From the analysis above, a two-step reconstructed algorithm can be formed.

(1) Offline preiterative step: the approximation of generalized inverse $A^+$ is calculated by several iterative steps of (6).
(2) Online reconstruction: when the weighted matrix $A$ keeps unchanged or the variation can be ignored, for updated detection $U$ the unknown character $X$ can be reconstructed simply through (5).

This preiteration method has already been applied to the image reconstruction in electrical impedance tomography (EIT) [15] which also belongs to the so-called "soft field" imaging as FODT, and it is proved that Landweber iteration method, which can produce higher quality reconstructed image than other direct regularized methods, is in fact a modification of the above preiteration algorithm [16]. However,

compared with Landweber method, the preiteration method remarkably improves the reconstructing speed by performing the time-consuming iterative process offline.

### 3.2. Second-order iteration form

However, the first-order preiteration algorithm with form equation (6) needs the same iteration steps as the Landweber method to produce the same quality images [15]. So just like the slow convergence of Landweber, for larger-sized dataset in FODT, iteration form of (6) is also very time-consuming even in the preiteration process. In order to speed up the iteration process, the second-order iterative format

$$S_{k+1} = S_k(2I - AS_k) \tag{7}$$

is used in our work.

To prove the convergence of the second-order form equation (7), we examined the convergence of $S_k$ and the residual error $R_k$ as follows.

First, by including (7), the iterative formula of $R_k$ can be obtained as

$$\begin{aligned} R_{k+1} &= I - AS_{k+1} = I - AS_k(2I - AS_k) \\ &= (I - AS_k)^2 = R_k^2. \end{aligned} \tag{8}$$

Then it can be inferred that

$$R_k = R_{k-1}^2 = R_{k-2}^4 = \cdots = R_0^{2^k}. \tag{9}$$

According to (7) and (9), $S_{k+1}$ can be written as a function of $R_0$ and $S_0$ in the formula

$$\begin{aligned} S_{k+1} &= S_k(I + R_k) = S_{k-1}(I + R_{k-1})(I + R_0^{2^k}) \\ &= S_0(I + R_0)(I + R_0^2)\cdots(I + R_0^{2^{k-1}})(I + R_0^{2^k}) \\ &= S_0(I - R_0)^{-1}(I - R_0^{2^{k+1}}), \end{aligned} \tag{10}$$

if $\rho(R_0) < 1$, let $k \to \infty$, it yields

$$S_\infty = \lim_{k\to\infty} S_k = S_0(I - R_0)^{-1}, \tag{11}$$

where $S_\infty$ can be proved as the generalized inverse matrix of $A$ [14].

However, with the first-order iteration form equation (6), residual error $\hat{R}_k = I - A\hat{S}_k$ for $k$ times iteration can be expressed as

$$\hat{R}_k = I - A(\hat{S}_{k-1} + S_0\hat{R}_{k-1}) = \hat{R}_0\,\hat{R}_{k-1}. \tag{12}$$

Then it can be inferred that

$$\hat{R}_k = \hat{R}_0^2\,\hat{R}_{k-2} = \cdots = \hat{R}_0^{k+1}. \tag{13}$$

By comparing (9) and (13), the difference between the convergence speed of the two iteration forms can be found. If the same value of $S_0$ is selected, $S_k$ can be directly obtained in the $k$th step *via* the second-order form as (7) while it requires $(2^k - 1)$-step first-order iteration of (6).

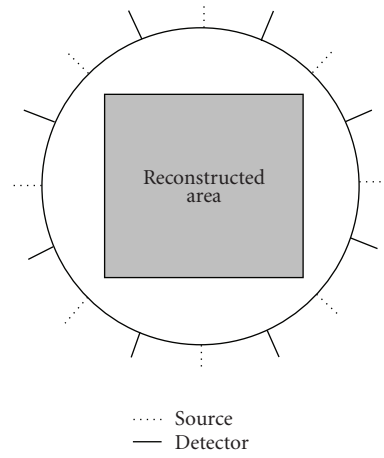


Figure 1: An illustration of system geometry. The excited sources and detectors are posed alternately around the circle of 50 mm diameter with equal intervals between each other. The power of the incident sources is 3 mw each.The reconstructed area is the central square slab of 0.1 cm thickness with each side of 32 mm. The solid lines represent the positions of the excited sources and the dotted lines represent the detectors.

## 4. SIMULATION AND RESULTS

The simulation in this paper is performed in CW mode (i.e., $\omega = 0$) and under the assumption of homogenous and approximately infinite medium. The algorithm can also be applied to arbitrary geometries linearized by analytical approximation or finite element method.

The measurement geometry for simulations is illustrated in Figure 1. The optical properties of the media are $\mu_s' = 10\,\text{cm}^{-1}$ and $\mu_a = 0.03\,\text{cm}^{-1}$ everywhere for both the excitation and emission wavelengths. The original fluorescent yield $\eta$ is $0.05\,\text{cm}^{-1}$ in the presence of the fluorescent probes. All the simulations were done in Matlab environment (version 7.0.1) on a 2.79 GHz Intel Pentium IV personal computer. The simulated measurement vector $U$ is computer-generalized by the product of coefficient matrix $A$ and the original distribution of $X$.

In the offline preiteration step, the approximation of $A^+$ is obtained by the iteration of (7) with proper iterative number $K$. However, in the simulation the iterative method is found to have the semiconvergence property. This is probably due to the accumulated round-off error in the computation. So the optimal iteration number should be determined according to experience or prior information about the system. In our simulation, a pretest with a known distribution of fluorescence yield $X$ is performed to choose $K$ for the particular imaging system. And the mean squared error (MSE) between the original $X$ and the reconstructed $\hat{X}$ is used as a criterion of the reconstructed quality. We investigated how the MSE changed against iteration times for several imaging systems with different sizes ($M$ measurements and $N$ voxels). Figure 2 shows that there is a relative flat segment where MSE changes very slowly before the iterative number begins to rise significantly. So the proper iteration number can be

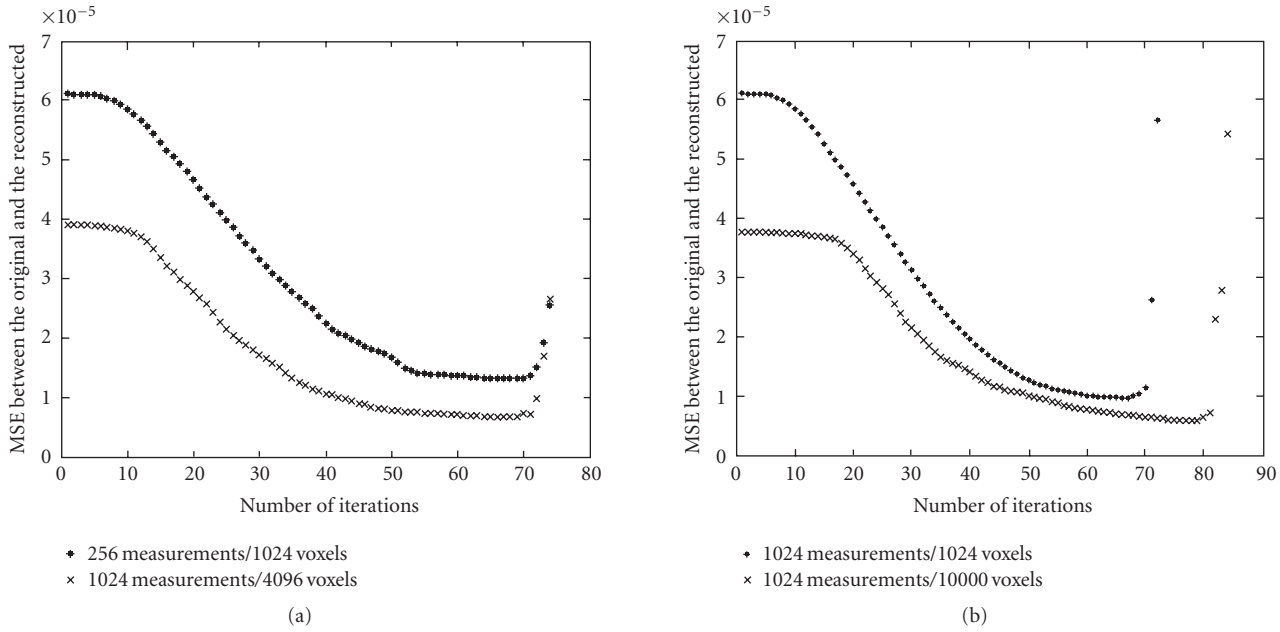


FIGURE 2: Number of iterations versus MSE (mean squared error) between the original and the reconstructed. (a) shows the MSE for datasets of $256 * 1024$ and $1024 * 4096$. Although the size is different, the iterative number where the MSE increases is the same, since they have the same value of $n/m$. Two datasets in (b) have the same number of measurements 1024, however, the MSE with 10000 voxels increases much later than the one with 1024 measurements.

chosen in this iteration number range. Figure 2 is obtained in a noise-free environment. However, it is also found that when noise exists, the MSE rises earlier than in a noise-free system. For different levers of noise, the iteration numbers where MSE rises are different.

With the iterative result $S_k$ and the simulated detection $U$, the distribution of fluorescent yield can be well reconstructed simply by $X_k = S_k U$. In our simulation, $X_k$ is then modified by including a nonlinear function $f$ to constrain the reconstructed values to $[0, 0.05]$, that is

$$f(X_k) = \begin{cases} 0, & X_k \le 0, \\ X_k, & \text{otherwise}, \\ 0.05, & X_k > 0.05. \end{cases} \tag{14}$$

In the simulation, occasions of single-probe as well as multiprobe are reconstructed for several different dataset sizes. It is proved that the distribution of the fluorescent yield $\eta$ can be well estimated by the fast algorithm (Figure 3). It can be seen that the algorithm works well when the measurement number is much less then the reconstructed number.

For different imaging subjects, the weighted matrix $A$ may need to be updated, so it would be desirable to know how the inversion time of the preiteration changes with different-sized datasets. According to the results of convergence of the iteration in Figure 2, 60-time iterations are chosen for all of the following datasets in order to compare the reconstructed timescales. The results are shown in Table 1. It can be inferred that for the same number of measurements $M$, the computing time is approximately proportional to the number of reconstructed voxels $N$. However, if $N$ remains constant, when $M$ rises to $l \cdot M$, the computing time will increase to nearly $l^2$ times of the original.

## 5. DISCUSSION AND CONCLUSIONS

With the preiteration method, we have demonstrated reconstruction of fluorescence concentration by using simulation data based on the analytical model with first-order Born approximation. Although in this paper, the fast algorithm is simply demonstrated with the analytical solution for specific medium geometry, it could also be applied to arbitrary geometries, where the model in (1) is discretized by numerical methods [7, 10] or the Kirchhoff approximation [5].

In the simulation, a pretest should be done to determine the proper iteration number. A relationship between the convergence property and the dataset size is also obtained through the investigations and it can be found from Figure 2 that in noise-free environment, the number of iterations when the MSE begins to rise mainly depends on the ratio of the voxels number $N$ and the number of measurements $M$, but not on the absolute value of them. This result will be helpful for the determination of the proper iteration number. For example, the convergence property of large dataset can be predicted from a smaller one with the same $N/M$. For a system with fixed measurement size, the larger the reconstructed mesh number is, the later will the MSE curve begin to rise.

The computation burden of the second-order iteration is further investigated in our work. It can be inferred from

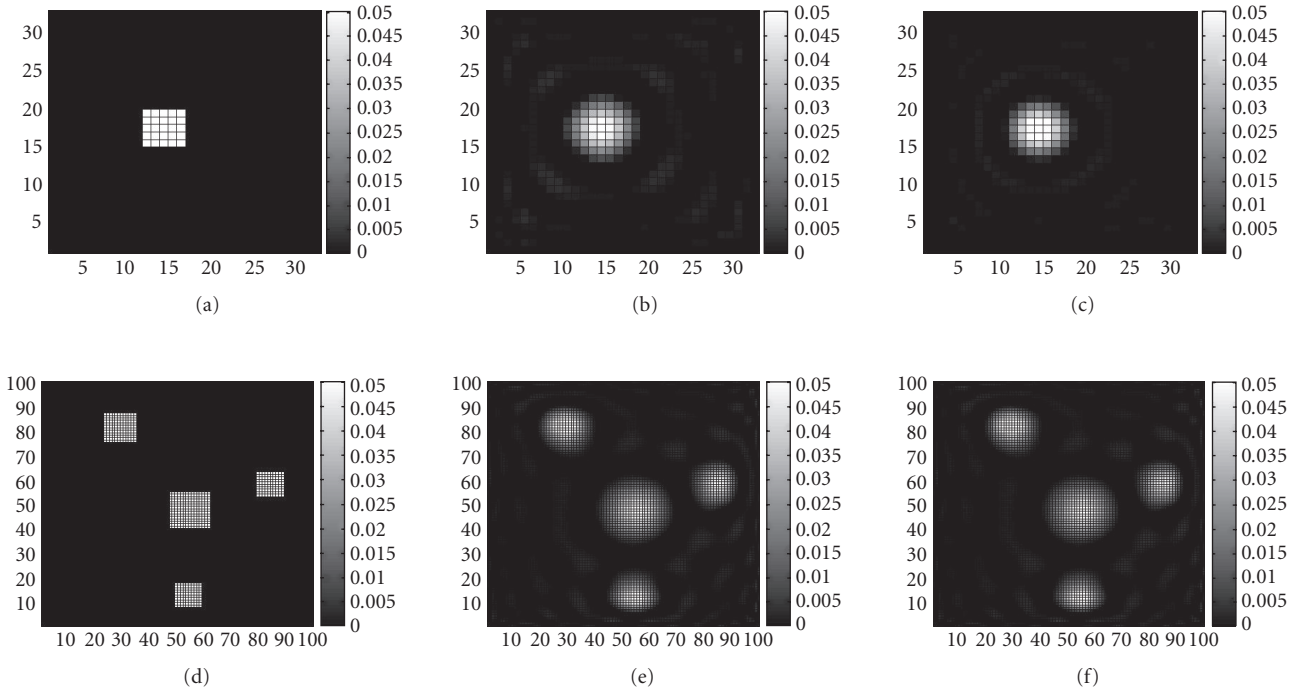


Figure 3: The original images and the reconstructions for single and multiprobe configurations with different datasets. (a) is the original distribution of the fluorescent yield $\eta$ with $32 * 32$ voxels. (b) and (c) separately show the reconstruction of (a) with 256 measurements and 1024 measurements. (d) is the original $\eta$ with image size of $100 * 100$ voxels. (e) and (f) show the reconstructions with 1024 measurements and 2048 measurements, respectively. For all of (b), (c), (e), (f), the iteration time in the preiteration step is 60.

Table 1: Computation time for 60 iterations.

| $m$ | $n$ | | |
|---|---|---|---|
| | 1024 | 4096 | 10000 |
| 256 | 4.2321 s | 16.4102 s | 39.2953 s |
| 512 | 16.0307 s | 61.5063 s | 147.5493 s |
| 1024 | 61.6572 s | 238.5744 s | 565.6728 s |

(7) that one iteration needs $2M^2 \cdot N$ times multiplication. So the computation burden is proportional to the number of reconstructed points $N$ when measurement number $M$ stays unchanged and to $M^2$ when $N$ is constant. This result is well proved in the simulation by the listed computing time for different numbers of measurements and voxels in Table 1.This feature should be very suitable for imaging systems where the number of voxels is always much larger than measurement number such as FODT. The results of both convergence property and computation burden indicate that the algorithm is very suitable for imaging systems in which the boundary measurement number is much less than the inside reconstructed voxels. In addition, the reconstructed images in Figure 3 showed that the algorithm works well for these kinds of system.

The most promising feature of the algorithm is the rapid reconstruction speed. It significantly accelerates the reconstruction process in the following two aspects. First, when the weighted matrix stays constant or the variance can be ignored, by allowing the time-consuming iteration to be performed offline, it provides great computational facility, which is just a unique matrix vector multiplication. Second, in the preiteration step, it is the second-order iteration form of (7) that exponentially improves the speed of the iterative process, which makes the algorithm feasible in practice and can be finally applied to FODT with datasets of large size. For example, to reconstruct the same quality images with 60 iterations of (7) (the reconstructed images are shown in Figure 3 and the computing time is shown in Table 1), it will cost about $2^{60}$ iterative steps using Landweber method or the first-order iterative form, requiring days for the reconstruction. So the first-order form is not practical for FODT of large-sized datasets even in the preiteration step. Therefore, the results demonstrate that the time efficiency of both the preiteration process and the online reconstruction is the most important advantage of the algorithm. It will be helpful to promote the development of real-time image reconstruction systems and dynamic monitoring of molecular activity.

## ACKNOWLEDGMENTS

This work is partially supported by the National Nature Science Foundation of China, the Tsinghua-Yue-Yuen Medical Science Foundation, the National Basic Research Program of China, and the Special Research Fund for the Doctoral Program of Higher Education of China.

## REFERENCES


[1] U. Mahmood, C.-H. Tung, A. Bogdanov Jr., and R. Weissleder, "Near-infrared optical imaging of protease activity for tumor detection," *Radiology*, vol. 213, no. 3, pp. 866–870, 1999.

[2] V. Ntziachristos, C.-H. Tung, C. Bremer, and R. Weissleder, "Fluorescence molecular tomography resolves protease activity in vivo," *Nature Medicine*, vol. 8, no. 7, pp. 757–760, 2002.

[3] R. Weissleder, C.-H. Tung, U. Mahmood, and A. Bogdanov Jr., "In vivo imaging of tumors with protease-activated near-infrared fluorescent probes," *Nature Biotechnology*, vol. 17, no. 4, pp. 375–378, 1999.

[4] V. Ntziachristos, J. Ripoll, and R. Weissleder, "Would near-infrared fluorescence signals propagate through large human organs for clinical studies?" *Optics Letters*, vol. 27, no. 5, pp. 333–335, 2002.

[5] J. Ripoll, M. Nieto-Vesperinas, R. Weissleder, and V. Ntziachristos, "Fast analytical approximation for arbitrary geometries in diffuse optical tomography," *Optics Letters*, vol. 27, no. 7, pp. 527–529, 2002.

[6] D. Y. Paithankar, A. U. Chen, B. W. Pogue, M. S. Patterson, and E. M. Sevick-Muraca, "Imaging of fluorescent yield and lifetime from multiply scattered light reemitted from random media," *Applied Optics*, vol. 36, no. 10, pp. 2260–2272, 1997.

[7] H. Jiang, "Frequency-domain fluorescent diffusion tomography: a finite-element-based algorithm and simulations," *Applied Optics*, vol. 37, no. 22, pp. 5337–5343, 1998.

[8] M. J. Eppstein, D. J. Hawrysz, A. Godavarty, and E. M. Sevick-Muraca, "Three-dimensional, Bayesian image reconstruction from sparse and noisy data sets: near-infrared fluorescence tomography," *Proceedings of the National Academy of Sciences of the United States of America*, vol. 99, no. 15, pp. 9619–9624, 2002.

[9] A. B. Milstein, S. Oh, K. J. Webb, et al., "Fluorescence optical diffusion tomography," *Applied Optics*, vol. 42, no. 16, pp. 3081–3094, 2003.

[10] A. X. Cong and G. Wang, "A finite-element-based reconstruction method for 3D fluorescence tomography," *Optics Express*, vol. 13, no. 24, pp. 9847–9857, 2005.

[11] M. A. O'Leary, D. A. Boas, X. D. Li, B. Chance, and A. G. Yodh, "Fluorescence lifetime imaging in turbid media," *Optics Letters*, vol. 21, no. 2, pp. 158–160, 1996.

[12] X. D. Li, M. A. O'Leary, D. A. Boas, B. Chance, and A. G. Yodh, "Fluorescent diffuse photon density waves in homogeneous and heterogeneous turbid media: analytic solutions and applications," *Applied Optics*, vol. 35, no. 19, pp. 3746–3758, 1996.

[13] V. Ntziachristos and R. Weissleder, "Experimental three-dimensional fluorescence reconstruction of diffuse media by use of a normalized Born approximation," *Optics Letters*, vol. 26, no. 12, pp. 893–895, 2001.

[14] Y. P. Cheng, K. Y. Zhang, and Z. Xu, *Matrix Theory*, Northwestern Polytechnic University Press, Xi'an, China, 2nd edition, 2000.

[15] H. Wang, C. Wang, and W. Yin, "A pre-iteration method for the inverse problem in electrical impedance tomography," *IEEE Transactions on Instrumentation and Measurement*, vol. 53, no. 4, pp. 1093–1096, 2004.

[16] W. Q. Yang, D. M. Spink, T. A. York, and H. McCann, "An image-reconstruction algorithm based on Landweber's iteration method for electrical-capacitance tomography," *Measurement Science and Technology*, vol. 10, no. 11, pp. 1065–1069, 1999.

Hindawi Publishing Corporation
International Journal of Biomedical Imaging
Volume 2007, Article ID 25182, 9 pages
doi:10.1155/2007/25182

*Research Article*

# Molecular Image Segmentation Based on Improved Fuzzy Clustering

**Jinhua Yu and Yuanyuan Wang**

*Department of Electronic Engineering, Fudan University, Shanghai 200433, China*

Received 18 January 2007; Revised 28 April 2007; Accepted 17 July 2007

Recommended by Jie Tian

Segmentation of molecular images is a difficult task due to the low signal-to-noise ratio of images. A novel two-dimensional fuzzy C-means (2DFCM) algorithm is proposed for the molecular image segmentation. The 2DFCM algorithm is composed of three stages. The first stage is the noise suppression by utilizing a method combining a Gaussian noise filter and anisotropic diffusion techniques. The second stage is the texture energy characterization using a Gabor wavelet method. The third stage is introducing spatial constraints provided by the denoising data and the textural information into the two-dimensional fuzzy clustering. The incorporation of intensity and textural information allows the 2DFCM algorithm to produce satisfactory segmentation results for images corrupted by noise (outliers) and intensity variations. The 2DFCM can achieve $0.96 \pm 0.03$ segmentation accuracy for synthetic images under different imaging conditions. Experimental results on a real molecular image also show the effectiveness of the proposed algorithm.



## 1. INTRODUCTION

Molecular imaging techniques such as positron emission imaging, fluorescent imaging, and isotope radiation imaging have undergone explosive growth over the past few decades. It will allow clinicians not only to measure concentrations of interesting molecules quantitatively, but also to visualize the interactions of molecular markers in vivo, thus extending the emphasis of radiological imaging beyond the anatomical and functional levels [1]. Integrations of molecular information specific to each patient with anatomical information obtained by conventional imaging methods such as the magnetic resonance imaging (MRI), X-ray computed tomography (CT), and ultrasound (US) will undoubtedly enhance the ability to fight disease. Image segmentation is a preliminary and crucial step for subsequent image applications such as quantification of molecular concentration, image registration, and integration. However, molecular images often suffer from a low signal-to-noise ratio (SNR); this will lead to difficulties with its segmentation.

The fuzzy clustering algorithm, more widely used as fuzzy C-means algorithm (FCM) [2], has been successfully utilized in medical image segmentation [3–6]. The most important feature of the FCM is that it allows each pixel to belong to multiple clusters according to its degree of membership in each cluster, which makes the clustering methods able to retain more information from the original image as compared to the case of hard segmentation. FCM works well on images with low levels of noise, but there are two disadvantages of the FCM used in segmentation of noise-corrupted images. One is that the FCM does not incorporate the information about the spatial context, which makes it sensitive to the noise and other imaging artifacts. The other is that the cluster assignment is based solely on the distribution of the pixel intensity, which makes it sensitive to intensity variations due to the illumination or the object geometry [7]. In order to improve the robustness of conventional FCM, many algorithms have been presented in the literatures. These methods can be divided into two main groups: imposing spatial constraints to clustering algorithms [3, 5–7] and introducing other features or dissimilarity index that is insensitive to intensity variations in the objective function of FCM [5, 7].

This paper presents a novel algorithm based on fuzzy logic for molecular image segmentation. In this algorithm, two factors to improve the robustness of conventional FCM are considered. Due to the low SNR of molecular images, image denoising is taken for a prelude to the segmentation. A denoising method which combines a Gaussian noise filter with an anisotropic diffusion (AD) technique is presented to alleviate noise in molecular images. Since the Gabor wavelet

representation of molecular images is relatively robust to intensity variations, a texture characterization method derived from Gabor filters bank is presented to extract texture information from images. Spatial constraints provided by the denoising data and texture information provided by the Gabor wavelet are embedded in the objective function of a novel two-dimensional fuzzy clustering (2DFCM) algorithm.

The remainder of this paper is organized as follows. Section 2 proposes the denoising method. Section 3 introduces the multichannel Gabor filters and the texture feature characterization. In Section 4, we present in detail the new two-dimensional FCM algorithm (2DFCM) which integrates both intensity information and texture information. The experimental comparisons are presented in Section 5. Section 6 concludes the paper.

## 2. MOLECULAR IMAGE DENOISING

Gaussian noise is the most common noise broadly existed in signal processing sciences. Ling and Bovik [8] proposed a method to smooth molecular images by assuming that the noise follows an additive Gaussian model. Following Ling and Bovik's notion, we also assume that molecular images are corrupted by a zero-mean Gaussian white noise.

The FIR filter is well known for its ability to remove Gaussian noise from signals but it does not work very well in the image processing since it blurs edges within the image. The Gaussian noise filter (GNF) [9], combining a nonlinear algorithm and a technique for automatic parameter tuning, is a valid method for estimation and filtering of Gaussian noise. The GNF used in this paper can be summarized as follows. Let $X = \{x_1, x_2, \ldots, x_n\}$ be a set of $n$ data points in the noisy image. The output $Y = \{y_1, y_2, \ldots, y_n\}$ is defined as

$$y_i = x_i + \frac{1}{N_R} \sum_{x_r \in N_i} \varsigma(x_r, x_i), \quad i = 1, \ldots, n, \tag{1}$$

$$\zeta(x_i, x_j) = \begin{cases} x_i - x_j, & |x_i - x_j| \le p, \\ \left(\dfrac{3p - |x_i - x_j|}{2}\right) \operatorname{sgn}(x_i - x_j), & p < |x_i - x_j| \le 3p, \\ 0, & |x_i - x_j| > 3p, \end{cases} \tag{2}$$

where $N_i$ stands for the neighborhood configuration with respect to a center pixel $x_i$, and $N_R$ is the cardinality of $N_i$. The automatic tuning of the parameter $p$ is a key step in GNF. Let MSE($k$) denote the mean square error between the noisy image filtered with $p = k$ and the same image filtered with $p = k - 1$. A heuristic estimate of the optimal parameter value is

$$\hat{p} = 2(k_m - 2), \tag{3}$$

where

$$\mathrm{MSE}(k_m) = \mathrm{MAX}\{\mathrm{MSE}(k)\}. \tag{4}$$

The GNF can remove intensity spikes due to the Gaussian noise. However, it has limited effect on suppressing little intensity variations caused by the neighboring smoothing. Since the conventional FCM is a method based on the statistical feature of the image intensity, a piecewise-smooth intensity distribution will be greatly beneficial to it. We pursue a more desirable denoising result by following the GNF with an anisotropic diffusion filter. Yu and Acton [10] provided an improved anisotropic diffusion filter called speckle reducing anisotropic diffusion (SRAD) which outperforms the traditional Perona-Malik nonlinear diffusion [11]. Although SRAD is proposed for the speckle reduction in synthetic aperture radar (SAR) or ultrasound images, its advantages in mean preservation, variance reduction, and edge localization are also preferable for molecular images. The SRAD used in this paper can be formulated as a diffusive process:

$$c(q) = \frac{1}{1 + [q^2(x, y; t) - q_0^2(t)]/[q_0^2(t)(1 + q_0^2(t))]}, \tag{5}$$

where $c(q)$ represents the diffusion coefficient, $q(x, y; t)$ is the instantaneous coefficient of variation served as the edge detector in the noise image. $q(x, y; t)$ combines a normalized gradient magnitude operator and a normalized Laplacian operator:

$$q(x, y; t) = \sqrt{\frac{(1/2)(|\nabla Y|/Y)^2 - (1/4^2)(\nabla^2 Y/Y)^2}{[1 + (1/4)(\nabla^2 Y/Y)]^2}}, \tag{6}$$

where $\nabla$ is the gradient operator and $Y$ is the image filtered by GNF. $q_0(t)$ is the scale function serving as the diffusion threshold which can be approximated by using a heuristic constant $q_0$ with the exponential decay function

$$q_0(t) \approx q_0 \exp[-\rho t]. \tag{7}$$

Here $\rho$ is a constant typically set to 1/6. Suppose that the output of the SARD with $Y = \{y_1, y_2, \ldots, y_n\}$ as the input can be represented by $X^* = \{x_1{}^*, x_2{}^*, \ldots, x_n{}^*\}$.

To clearly illustrate the denoising effect of GNF plus SRAD, Figure 1 shows a group of filtering results of GNF alone, SRAD alone, GNF plus SRAD, and the anisotropic median-diffusion (AMD) [8] on a synthetic molecular image. From the filtering results comparison, it is seen that the denoising method of integrating GNF with SRAD can overcome the intensity fluctuation effect of GNF and the "blocky" effect of SRAD and MAD.

## 3. TEXTURE CHARACTERIZATION

A molecular image illustrates the distribution of a certain molecule [8]. Since the photon has different transportation characteristics in different turbid tissues, a molecular image can be divided into several separate regions with each region showing similar intensity (implying similar molecular concentration) and certain kind of textural pattern. Because the photon distribution in a turbid tissue is not usually uniform, the intensity within a region usually changes gradually. This intensity variation can cause errors when attempting to segment images using intensity-based classification methods. Intuitively, if a feature insensitive to the slowly varying intensity can be introduced into the classification, the performance of the image segmentation could be improved. Here,

(a) (b) (c) (d) (e)

Figure 1: Denoising effect comparison among GNF, SRAD, and GNF plus SRAD: (a) original image; (b) filtering result of GNF; (c) filtering result of SRAD; (d) filtering result of GNF plus SRAD; (e) filtering result of anisotropic median-diffusion (MAD) [8].

a texture characterization method based on the Gabor wavelet is utilized to obtain this desirable feature.

A large number of texture classification techniques have been proposed in the past two decades [12]. Gabor wavelet has been a popular method because it can capture the local structure corresponding to spatial frequency, spatial localization, and orientation selectivity. As a result, Gabor wavelet representation of an image should be robust to intensity variations [13, 14]. A Gabor function in the spatial domain is a sinusoidal modulated Gaussian. The real impulse response of Gabor filter is given by

$$h(x,y;\mu,\theta) = \exp\left\{-\frac{1}{2}\left[\frac{x^2}{\sigma_x^2}+\frac{x^2}{\sigma_y^2}\right]\right\}\cdot\cos(2\pi\mu x), \tag{8}$$

where $x = x'\cos\theta + y'\sin\theta$, $y = -x'\sin\theta + y'\cos\theta$, $(x, y)$ represent rotated spatial-domain rectilinear coordinates, $u$ is the frequency of the sinusoidal wave along the direction $\theta$ from the $x$-axis, $\sigma_x$ and $\sigma_y$ define the size of the Gaussian envelope along $x$- and $y$-axes, respectively, which determine the bandwidth of the Gabor filter. The frequency response of the filter is given by

$$H(U,V) = 2\pi\sigma_x\sigma_y\left(\exp\left\{-\frac{1}{2}\left[\frac{(U-u)^2}{\sigma_u^2}+\frac{V^2}{\sigma_v^2}\right]\right\} + \exp\left\{-\frac{1}{2}\left[\frac{(U+u)^2}{\sigma_u^2}+\frac{V^2}{\sigma_v^2}\right]\right\}\right), \tag{9}$$

where $\sigma_u = 1/2\pi\sigma_x$, $\sigma_v = 1/2\pi\sigma_y$. By tuning $u$ and $\theta$, multiple filters that cover the spatial frequency domain can be obtained. In our study, Gabor wavelets with four different scales, $\mu \in \{\pi/4\sqrt{2}, \pi/4, \pi/2\sqrt{2}, \pi/2\}$, and eight orientations, $\theta \in \{0\pi/8, 1\pi/8, \ldots, 7\pi/8\}$, are used. Let $X(x, y)$ be the intensity level of an image. The Gabor wavelet representation is the convolution of $X(x, y)$ with a family of Gabor kernels:

$$G_{\mu,\theta}(x,y) = X(x,y) * h(x,y;\mu,\theta), \tag{10}$$

where $*$ denotes the convolution operator, and $G_{u,\theta}$ is the convolution result corresponding to the Gabor kernel at the scale $\mu$ and the orientation $\theta$. The next step is to compute the textural energy in $G_{u,\theta}$. The textural energy is a measure widely used to characterize the image texture. The energy that corresponds to a square window of the image $G_{u,\theta}$ centered at $x$ and $y$ is defined as

$$E_{\mu,\theta}(x,y) = \frac{1}{M^2}\sum_{(i,j)\in W_{xy}} \left|F(G_{\mu,\theta}(i,j))\right|, \tag{11}$$

where $M^2$ is the total number of pixels in the window, and $F(.)$ is a nonlinear, sigmoid function of the form

$$F(t) = \tanh(\alpha t) = \frac{1-e^{-2\alpha t}}{1+e^{-2\alpha t}}, \tag{12}$$

where $\alpha$ equals 0.25. The texture feature image is finally given by

$$T(x,y) = \frac{1}{32}\sum_{\mu,\theta} E_{\mu,\theta}(x,y). \tag{13}$$

As an example, Figure 2(a) shows a synthetic image with the intensity inhomogeneity. Figure 2(b) gives the texture energy bank ($E_{\mu,\theta}$) illustration. Figure 2(c) shows the texture feature image. From this example, it is seen that the texture feature characterization using Gabor wavelet is insensitive to the intensity inhomogeneity.

## 4. 2DFCM

### 4.1. FCM

Let $X = \{x_1, x_2, \ldots, x_n\}$ be a set of $n$ data points, and let $c$ be the total number of clusters. The objective function of the FCM [2] for partitioning $X$ into $c$ clusters is given by

$$J_{\text{FCM}} = \sum_{j=1}^{c}\sum_{i=1}^{n}\mu_{ij}^{b}||x_i - m_j||^2, \tag{14}$$

where $m_j$, $j = 1, 2, \ldots, c$, represent the cluster prototypes and $\mu_{ij}$ gives the membership of pixel $x_i$ in the $j$th cluster $m_j$. The parameter $b$ is the fuzzy index that satisfies $b \in (1, \infty)$ and controls the degree of "fuzziness" in the resulting classification. The fuzzy partition matrix satisfies

$$U = \left\{\mu_{ij} \in [0,1] \;\middle|\; \sum_{j=1}^{c}\mu_{ij} = 1\ \forall i,\ 0 < \sum_{i=1}^{N}\mu_{ij} < N\ \forall j\right\}. \tag{15}$$

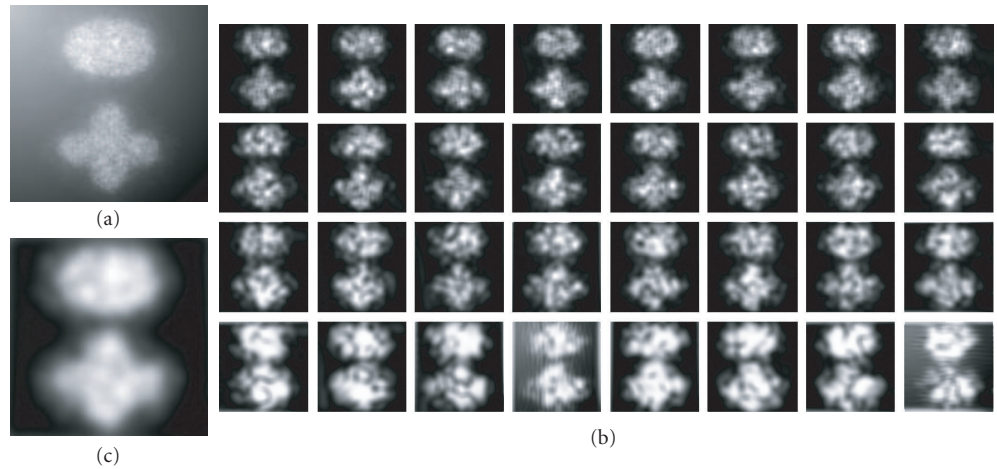

Figure 2: Illustration of the texture feature characterization: (a) original image with the intensity inhomogeneity; (b) texture energy bank illustration; (c) texture feature image.

Under the constraints condition of (15), taking the first derivations of (14) with respect to $\mu_{ij}$ and $m_j$ and setting those equations to zero yield necessary conditions for (14) to be minimized. Performing iteration through these two necessary conditions leads to an iterative scheme for minimizing the objective function. The objective function (14) is minimized when high membership values are assigned to pixels whose intensities are close to the centroid of its particular class, and low membership values are assigned when the pixel data is far from the centroid [2]. After FCM clustering, a segmentation of the image can be obtained by assigning each pixel solely to the class that has the highest membership value for that pixel.

Although the membership allows a pixel to deviate from multiple cluster prototypes, the spatial correlation between adjacent pixels is not considered.

### 4.2. FCM with spatial constraints

A popular method to introduce the local spatial context into the pixel classification is the spatial constraint. The spatial constraint is to let the spatial information influence the classification of the pixel of interest [5, 6]. Let $N_i$ denote the configuration of neighbors that exists in a window around $x_i$. According to the assumption that real-world images usually have strong correlation among neighboring pixels, if the pixel $x_i$ belongs to the cluster with the prototype $m_j$, then pixels in $N_i$ and the center pixel $x_i$ should have similar and high membership values in $m_j$. This original idea of incorporating local spatial constraints in the FCM is formulized as [15]

$$J_{\text{FCM\_S}} = \sum_{j=1}^{c}\sum_{i=1}^{n}\mu_{ij}^{b}||x_i - m_j||^2 + \frac{\alpha}{N_R}\sum_{j=1}^{c}\sum_{i=1}^{n}\mu_{ij}^{b}\left(\sum_{x_r\in N_i}||x_r - m_j||^2\right), \tag{16}$$

where $N_i$ stands for the neighborhood configuration with respect to a center pixel $x_i$, $N_R$ is the cardinality of $N_i$, $\alpha$ controls the effect of the neighboring penalty. The second term on the right side of (16) allows the labeling of a pixel to be influenced by the labels in its immediate eight neighborhoods and aims at keeping continuity in the neighboring window. The problem with (16) is that computing the neighborhood terms will cost much more time than clustering. In order to reduce the complexity of computing the neighborhood terms, the dissimilarity measurements between the whole neighborhood configuration and the prototype $m_j$ can be replaced by a distance from a feature data of $N_i$ to $m_j$. The feature data of the neighborhood configuration can be obtained by several kinds of neighboring window filters, such as the linear filter or the median filter. This approach is expressed in the following objective function [5]:

$$J_{\text{FCM\_S}'} = \sum_{j=1}^{c}\sum_{i=1}^{n}\mu_{ij}^{b}||x_i - m_j||^2 + \alpha\sum_{j=1}^{c}\sum_{i=1}^{n}\mu_{ij}^{b}||x_i^{\wedge} - m_j||^2, \tag{17}$$

where $x_i^{\wedge}$ is a mean or median of neighboring pixels lying within a window around $x_i$. Here, we modify (17) by substituting $x_i^{\wedge}$ with denoising molecular image data $x_i^{*}$. The objective function for the FCM with spatial constraints (called FCM_S later) is given by

$$J_{\text{FCM\_S}} = \sum_{j=1}^{c}\sum_{i=1}^{n}\mu_{ij}^{b}||x_i - m_j||^2 + \alpha\sum_{j=1}^{c}\sum_{i=1}^{n}\mu_{ij}^{b}||x_i^{*} - m_j||^2. \tag{18}$$

### 4.3. 2DFCM

Equation (18) introduces spatial constraints into the clustering procedure. However, the classification result of (18) still solely depends on the intensity distribution of the image, which makes it sensitive to intensity variations within a turbid tissue. With the texture information obtained by the Gabor wavelet bank, the two-dimensional fuzzy C-Means (2DFCM) algorithm is constructed by integrating both the

intensity and the texture information. Suppose that the texture feature image is $T = \{t_1, t_2, \ldots, t_n\}$, the objective function of 2DFCM can be expressed as

$$J_{\text{2DFCM}} = \sum_{j=1}^{c}\sum_{i=1}^{n}\mu_{ij}^{b}||x_i - m_j||^2 + \alpha\sum_{j=1}^{c}\sum_{i=1}^{n}\mu_{ij}^{b}||x_i^* - m_j||^2 + \beta_i\sum_{j=1}^{c}\sum_{i=1}^{n}\mu_{ij}^{b}||t_i - v_j||^2. \tag{19}$$

The influence of the texture characterization imposed on the clustering procedure can be controlled by a constant vector $\beta_i (i = 1, \ldots, n)$; the prototype of texture image data is represented by $v_j (j = 1, \ldots, c)$. The choice of $\beta_i$ is based on the following principle. If $t_i$ is large, implying the texture energy is dominant, and $\beta_i$ should be large; if $t_i$ is small, implying the texture energy is weak, and $\beta_i$ should be also small. The $\beta_i$ is determined by $\beta_i = (Bt_i)/\max(T)$, where $B$ is a constant and its optimized value is determined by "trial-and-error" technique (see Section 5 for details).

The optimization problem under the constraint of $U$ as stated in (15) can be solved using one Lagrange multiplier:

$$F = \sum_{j=1}^{c}\sum_{i=1}^{n}\mu_{ij}^{b}||x_i - m_j||^2 + \alpha\sum_{j=1}^{c}\sum_{i=1}^{n}\mu_{ij}^{b}||x_i^* - m_j||^2 + \beta_i\sum_{j=1}^{c}\sum_{i=1}^{n}\mu_{ij}^{b}||t_i - v_j||^2 + \lambda\left(1 - \sum_{j=1}^{c}\mu_{ij}\right). \tag{20}$$

Taking the derivative of $F$ with respect to $\mu_{ij}$ and setting the result to zero, we can obtain an equation for $\mu_{ij}$ with unknown

$$\mu_{ij} = \left\{\frac{\lambda}{b[(x_i - m_j)^2 + \alpha(x_i^* - m_j)^2 + \beta_i(t_i - v_j)^2]}\right\}^{1/(b-1)}. \tag{21}$$

Utilizing the constraint of $U$ can be solved as

$$\lambda = \left\{\sum_{k=1}^{c}\left\{b\left[(x_i - m_j)^2 + \alpha(x_i^* - m_j)^2 + \beta_i(t_i - v_j)^2\right]\right\}^{1/(b-1)}\right\}^{b-1}. \tag{22}$$

Substituting (22) into (21), a necessary condition for (19) to be at a local minimum will be obtained:

$$\mu_{ij} = \frac{\left[(x_i - m_j)^2 + \alpha(x_i^* - m_j)^2 + \beta_i(t_i - v_j)^2\right]^{-1/(b-1)}}{\sum_{k=1}^{c}\left[(x_i - m_k)^2 + \alpha(x_i^* - m_k)^2 + \beta_i(t_i - v_k)^2\right]^{-1/(b-1)}}. \tag{23}$$

Similarly, zeroing the derivative of $F$ with respect to $m_j$ and $v_j$, we have

$$m_j = \frac{\sum_{i=1}^{n}\mu_{ij}^{b}(x_i + \alpha x_i^*)}{(1+\alpha)\sum_{i=1}^{n}\mu_{ij}^{b}}, \qquad v_j = \frac{\sum_{i=1}^{n}\mu_{ij}^{b}t_i}{\sum_{i=1}^{n}\mu_{ij}^{b}}. \tag{24}$$

### 4.4. Implementation of 2DFCM

For the 2DFCM, the number of prototypes ($c$) and the initial centroids ($\mathbf{M} = \{(m_j, v_j) \mid j = 1, \ldots, c\}$) ought to be known at the beginning of iterative procedures. A maximum likelihood approach by processing and analyzing the two-dimensional (2D) histogram of $X$ and $T$ is used to estimate $c$ and $\mathbf{M}$. The number of prototypes ($c$) and initial prototypes ($\mathbf{M}$ ) is estimated by following steps.

(1) Count the number of peaks in the 2D histogram and record it as $PeakNum^{prev}$.
(2) Filter the histogram using a five-by-five Gaussian filter with zero mean and a standard deviation of 0.6.
(3) Pick peak points in the 2D histogram and record the number of peaks using $PeakNum^{next}$. Then calculate $PeakSub = PeakNum^{next} - PeakNum^{prev}$, and $PeakNum^{prev} = PeakNum^{next}$.
(4) If $PeakSub < 1$, then go to step (5); if $PeakSub \geq 1$, then go to step (2);
(5) The $c$ is estimated as the number of peaks existing in the filtered 2D histogram and the locations of $c$ peaks found are used as the initial centroids $\mathbf{M}$.

The procedure of 2DFCM can be summarized in the following steps.

(1) Filter the image using GNF followed by SRAD to generate the denoising data $X^*$.
(2) Filter the image using Gabor wavelet band and compute the texture feature image $T$.
(3) Formulate the 2D histogram using the denoising data $X^*$ and the texture feature image $T$. Estimate the number of clusters ($c$) and initial prototypes ($\mathbf{M}$).
(4) Repeat the following steps until the centroids variation is less than 0.001.
    (a) Update the membership function matrix using (23).
    (b) Update the centroids using (24).
    (c) Calculate the centroids variation between before updating and after updating.

## 5. EXPERIMENTAL RESULTS AND DISCUSSIONS

We perform experiments on a PC with 2.0 GHz Pentium processor using Visual C++ 6.0. To illustrate the performance of the 2DFCM, we first test it using simulated molecular images from which the ground truth data is available. Simulated molecular images are obtained by using MOSE (Monte Carlo optical simulation environment) [16–18] developed by Bioluminescence Tomography Lab, Department of Radiology and Department of Biomedical Engineering, University of Iowa (http://radiology.uiowa.edu/). MOSE is based on Monte Carlo method to simulate bioluminescent phenomena in the mouse imaging and to predict bioluminescent signals around the mouse.

The optimized $\alpha$ and $B$ in the 2DFCM should be obtained by "trial-and-error" technique. We first choose an appropriate value for $\alpha$ based on the segmentation performance of the FCM with spatial constraints (FCM_S) (the objective

function is formularized as (18). We take a group of values for $\alpha$ ranging from 0.25 to 6 to test the misclassification rate. With the increasing of $\alpha$, the number of misclassified pixels reduces. However, after $\alpha$ exceeds 3, the segmentation performance of the FCM_$S$ has no apparent changes. Therefore, we set $\alpha = 3.5$ in our study, which is a value that can produce steady and good results. Then, we choose an appropriate value for $B$ based on the segmentation performance of the 2DFCM. We also take a group of values for $B$ ranging from 5 to 80 to test the misclassification rate. After $B$ exceeds 36, the segmentation performance of the 2DFCM has no apparent changes. Therefore, we set $B = 36$ in our work, which gives steady and satisfactory results. The computation time of the proposed algorithm on an image of $128 \times 128$ is approximately 12 seconds. About two thirds of total time are consumed in texture characterization based on Gabor wavelet.

The first example is applying algorithms to a synthetic cellular image and comparing the 2DFCM with other three algorithms, including the FCM on the original image, the FCM with spatial constraints, and the FCM on the texture feature image. The model to generate synthetic molecular images is illustrated in Figure 3(a). The simulated molecular image ($128 \times 128$) corresponding to Figure 3(a) is shown in Figure 3(b). Then Figure 3(b) is corrupted by the intensity inhomogeneity (as shown in Figure 3(c)) to generate the final synthetic image (as shown in Figure 3(d)). Figure 3(e) shows the image filtered by the GNF plus SRAD. Figure 3(f) shows the texture feature image obtained by the Gabor wavelet bank. Figures 3(g)–3(j) give the segmentation results of the FCM on the original image (Figure 3(d)), the FCM with spatial constraints, the FCM on the texture feature image (Figure 3(f)), and the 2DFCM, respectively. We quantify the algorithm performance in terms of three parameters defined as follows:

$$\begin{aligned} \mathrm{SA} &= \frac{N_{\mathrm{CORRECT}}}{N_{\mathrm{TOTAL}}}, \\ \mathrm{US} &= \frac{N_{fp}}{N_n}, \\ \mathrm{OS} &= \frac{N_{fn}}{N_p}. \end{aligned} \tag{25}$$

SA represents the total segmentation accuracy; US is the under segmentation rate; OS denotes the over segmentation rate. $N_{CORRECT}$ is the number of correctly classified pixels; $N_{TOTAL}$ is the total number of pixels; $N_{fp}$ is the number of pixels that do not belong to the class and are segmented into this class; $N_{fn}$ is the number of pixels that belong to the class and are not segmented into the class; $N_p$ is the number of all pixels that belong to the class; $N_n$ is the number of all pixels that do not belong to the class. There are totally four algorithms that are compared in our experiments. Table 1 gives the SA, US, and OS comparisons among the four algorithms, correspondingly.

To further test the segmentation performance of the proposed method, a group of synthetic images under different imaging conditions are utilized. Nine synthetic images are shown in Figure 4. These images are organized into the form with different photons density along the vertical direction and different types of intensity inhomogeneity along the horizontal direction. Table 2 summarizes the segmentation accuracy of the FCM on the original image, the FCM with

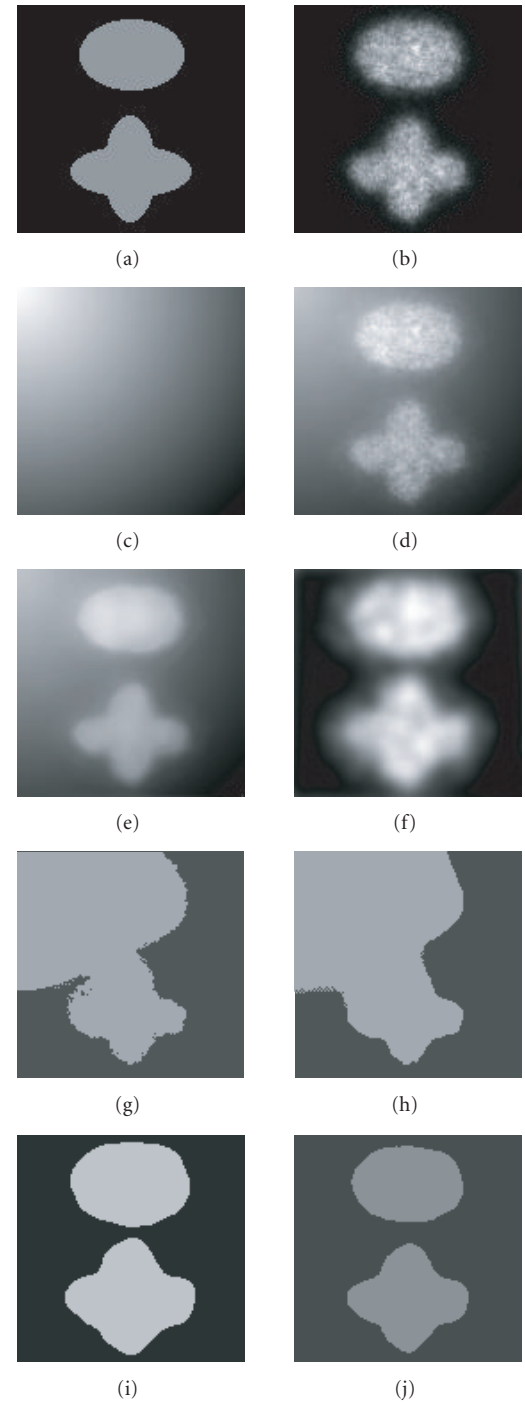


Figure 3: Segmentation results on the first synthetic image: (a) the ground truth image; (b) the synthetic image generated by MOSE; (c) the intensity inhomogeneity model; (d) the synthetic image corrupted by the intensity inhomogenetiy; (e) the denoising result with the GNF plus SRAD; (f) the texture feature image; (g) the FCM result on (d); (h) the FCM_$S$ result on (d); (i) the FCM result on texture feature image; (j) the 2DFCM result.

Table 1: SA, US, and OS of the three-conventional FCM and 2DFCM on Figure 3.

| Parameter | The FCM on original image | The FCM with spatial constraints | The FCM on texture image | The 2DFCM |
|---|---|---|---|---|
| SA | 0.72 | 0.71 | 0.91 | 0.97 |
| US | 1.12 | 1.16 | 0.35 | 0.13 |
| OS | 0.01 | 0.01 | 0 | 0 |

SA: segmentation accuracy.
US: undersegmentation rate.
OS: oversegmentation rate.

Table 2: SA of the three-conventional FCM and 2DFCM on images with different imaging conditions.

| Parameter | The FCM on original image | The FCM with spatial constraints | The FCM on texture image | The 2DFCM |
|---|---|---|---|---|
| SA | $0.87 \pm 0.15$ | $0.86 \pm 0.14$ | $0.93 \pm 0.03$ | $0.96 \pm 0.03$ |

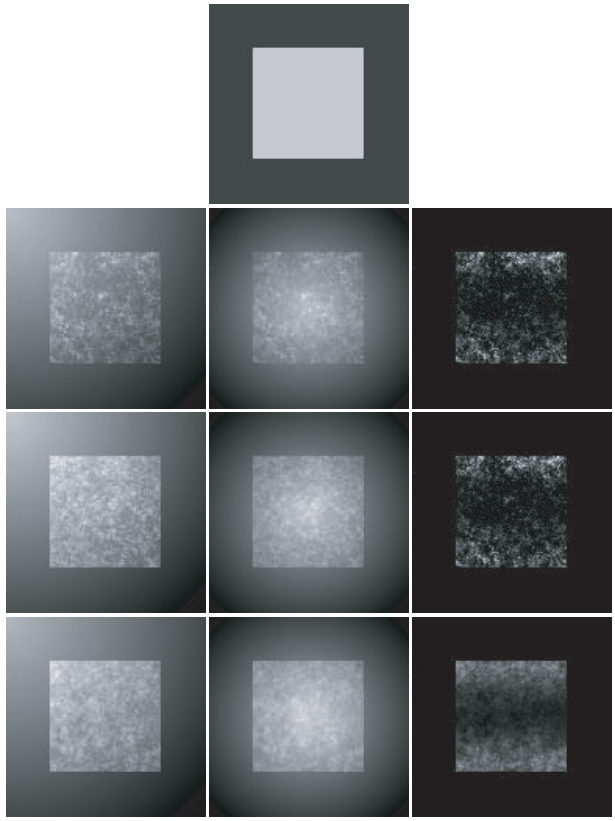

Figure 4: Synthetic images under different imaging conditions. First row: the ground truth image. From the second row to bottom: synthetic images with different photons density along the vertical direction and different types of intensity inhomogeneity along the horizontal direction.

spatial constraints, the FCM on the texture feature image, and the 2DFCM, respectively.

The second example is applying the algorithms to a real-molecular image ($256 \times 256$) (as shown in Figure 5(a)). Figures 5(b) and 5(c) show the denoising result of the GNF plus SRAD, and the texture feature image obtained by the Gabor wavelet bank, respectively. Figures 5(d)–5(g) illustrate the segmentation results of the FCM on the original image, the FCM with spatial constraints, the FCM on the texture feature image, and the 2DFCM, respectively. In order to illustrate the segmentation results clearly, the contours of the interest of region in the classification image are extracted and superimposed on the original image. Figures 5(h)–5(k) give the contour comparisons. It can be seen from Figure 5(a) that the middle of the tissue appears homogeneously bright. However, the molecular concentration decreases in the boundary area, which leads to the intensity variation near the boundary. The conventional FCM on the original image and the FCM with spatial constraints produce undersegmentation results and the FCM on the texture feature image shows oversegmentation.

From the experimental results, we can see that the denoising effects of the GNF plus SRAD are satisfactory. The Gabor wavelet bank can represent the texture information in the molecular image without being disturbed by the intensity variation. The FCM produces the worst result due to the fact that no spatial constraints are used in it. The FCM with spatial constraints produces more smoothed segmentation results than the FCM. However the intensity inhomogeneity makes the segmentation result degenerate. Since the 2DFCM utilizes both the intensity and texture information simultaneously, it produces more satisfactory results than other methods.

## 6. CONCLUSIONS

In this paper, we have developed a novel algorithm based on the fuzzy clustering for the molecular image segmentation. Considering that there are two disadvantages for the conventional FCM in the image segmentation, its successful employment in the molecular image segmentation requires overcoming nonrobust factors by introducing spatial constraints and the texture feature of images into the clustering. To alleviate noises in molecular images, a denoising method combining GNF plus SRAD is proposed. We use the denoising data obtained by GNF plus SRAD to compose spatial constraints for the new 2DFCM. By utilizing the Gabor wavelet representation and the texture energy characterization, the texture feature that is insensitive to intensity variations is introduced into the 2DFCM. Quantitative evaluation demonstrates the superiority of the 2DFCM over the conventional FCM in the molecular image segmentation.

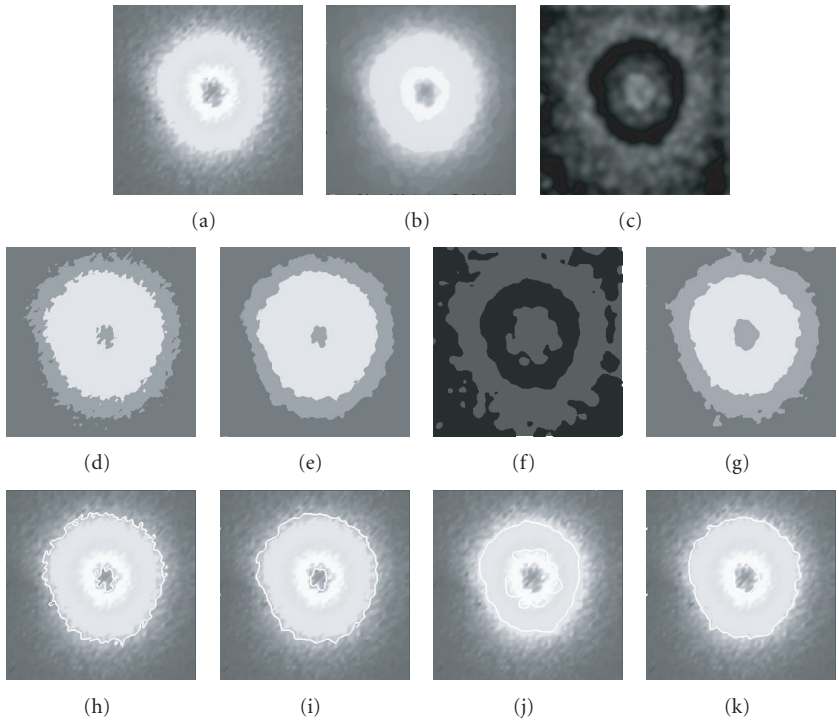


Figure 5: Segmentation results on a real molecular image: (a) the original image; (b) the denoising result with the GNF plus SRAD; (c) the texture feature image; (d) the FCM result on (a); (e) the FCM_*S* result on (a); (f) the FCM result on the texture feature image; (g) the 2DFCM results; (h)–(k) the contours obtained from (d) to (g) superimposed on the original image, respectively.

## ACKNOWLEDGMENTS

This work was supported by the National Basic Research Program of China (no. 2006CB705700), Natural Science Foundation of China (no. 30570488), and Shanghai Science and Technology Plan (no. 054119612).

## REFERENCES

[1] A. Hengerer, A. Wunder, D. J. Wagenaar, A. H. Vija, M. Shah, and J. Grimm, "From genomics to clinical molecular imaging," *Proceedings of the IEEE*, vol. 93, no. 4, pp. 819–828, 2005.

[2] J C. Bezdek, "A convergence theorem for the fuzzy ISODATA clustering algorithm," *IEEE Transactions on Pattern Analysis and Machine Intelligence*, vol. 2, no. 1, pp. 1–8, 1980.

[3] M. N. Ahmed, S. M. Yamany, N. Mohamed, A. A. Farag, and T. Moriarty, "A modified fuzzy c-means algorithm for bias field estimation and segmentation of MRI data," *IEEE Transactions on Medical Imaging*, vol. 21, no. 3, pp. 193–199, 2002.

[4] D. L. Pham and J. L. Prince, "Adaptive fuzzy segmentation of magnetic resonance images," *IEEE Transactions on Medical Imaging*, vol. 18, no. 9, pp. 737–752, 1999.

[5] S. Chen and D. Zhang, "Robust image segmentation using FCM with spatial constraints based on new kernel-induced distance measure," *IEEE Transactions on Systems, Man, and Cybernetics*, vol. 34, no. 4, pp. 1907–1916, 2004.

[6] Y. A. Tolias and S. M. Panas, "Image segmentation by a fuzzy clustering algorithm using adaptive spatially constrained membership functions," *IEEE Transactions on Systems, Man, and Cybernetics*, vol. 28, no. 3, pp. 359–369, 1998.

[7] A. W. C. Liew, H. Yan, and N.-F. Law, "Image segmentation based on adaptive cluster prototype estimation," *IEEE Transactions on Fuzzy Systems*, vol. 13, no. 4, pp. 444–453, 2005.

[8] J. Ling and A. C. Bovik, "Smoothing low-SNR molecular images via anisotropic median-diffusion," *IEEE Transactions on Medical Imaging*, vol. 21, no. 4, pp. 377–384, 2002.

[9] F. Russo, "A method for estimation and filtering of Gaussian noise in images," *IEEE Transactions on Instrumentation and Measurement*, vol. 52, no. 4, pp. 1148–1154, 2003.

[10] Y. Yu and S. T. Acton, "Speckle reducing anisotropic diffusion," *IEEE Transactions on Image Processing*, vol. 11, no. 11, pp. 1260–1270, 2002.

[11] P. Perona and J. Malik, "Scale-space and edge detection using anisotropic diffusion," *IEEE Transactions on Pattern Analysis and Machine Intelligence*, vol. 12, no. 7, pp. 629–639, 1990.

[12] T. Randen and J. H. Husy, "Filtering for texture classification: a comparative study," *IEEE Transactions on Pattern Analysis and Machine Intelligence*, vol. 21, no. 4, pp. 291–310, 1999.

[13] B. Schiele and J. L. Crowley, "Recognition without correspondence using multidimensional receptive field histograms," *International Journal of Computer Vision*, vol. 36, no. 1, pp. 31–50, 2000.

[14] C. Liu and H. Wechsler, "Gabor feature based classification using the enhanced Fisher linear discriminant model for face recognition," *IEEE Transactions on Image Processing*, vol. 11, no. 4, pp. 467–476, 2002.

[15] M. N. Ahmed, S. M. Yamany, N. Mohamed, A. A. Farag, and T. Moriarty, "A modified fuzzy c-means algorithm for bias field estimation and segmentation of MRI data," *IEEE Transactions on Medical Imaging*, vol. 21, no. 3, pp. 193–199, 2002.

[16] H. Li, J. Tian, F. Zhu, et al., "A mouse optical simulation environment (MOSE) to investigate bioluminescent phenomena in the living mouse with the Monte Carlo method," *Academic Radiology*, vol. 11, no. 9, pp. 1029–1038, 2004.

[17] H. Li, J. Tian, J. Luo, G. Wang, and W. Cong, "Interactive graphic editing tools in bioluminescent imaging simulation," in *Photonic Therapeutics and Diagnostics*, vol. 5686 of *Proceedings of SPIE*, pp. 407–414, San Jose, Calif, USA, January 2005.

[18] Y. J. Lv, J. Tian, H. Li, W. Cong, and G. Wang, "Adaptive finite element methods for diffusive photon propagation in bioluminescent imaging," in *Proceedings of the 4th Annual Meeting of Molecular Imaging*, p. 369, Cologne, Germany, September 2005.

Hindawi Publishing Corporation
International Journal of Biomedical Imaging
Volume 2007, Article ID 48989, 6 pages
doi:10.1155/2007/48989

*Research Article*

# A Monte-Carlo-Based Network Method for Source Positioning in Bioluminescence Tomography

**Zhun Xu, Xiaolei Song, Xiaomeng Zhang, and Jing Bai**

*Department of Biomedical Engineering, School of Medicine, Tsinghua University, Beijing 100084, China*

Received 19 January 2007; Revised 22 May 2007; Accepted 4 July 2007

Recommended by Jie Tian

We present an approach based on the improved Levenberg Marquardt (LM) algorithm of backpropagation (BP) neural network to estimate the light source position in bioluminescent imaging. For solving the forward problem, the table-based random sampling algorithm (TBRS), a fast Monte Carlo simulation method we developed before, is employed here. Result shows that BP is an effective method to position the light source.



## 1. INTRODUCTION

Recently developed bioluminescence tomography (BLT), with its noninvasive nature, has become a hotspot in invivo optical imaging which can reveal the molecular and cellular activity through determining the distribution of bioluminescent sources [1, 2]. Therefore, it can be applied to the study of much physiological and pathological processes through small animal imaging, such as monitoring tumor growing and drug delivery, evaluating new therapies, and examining protein and gene functions.

There are two basic points in the reconstruction of BLT, one is the accurate modeling and solving of photon propagation through biologic tissues, and the other is the proper inversion strategy. Most existing reconstruction methods in BLT were based on diffusion approximation of radiative transfer equation. And the diffusion approximation, considered as a linear problem, can be solved by using classical inversion methods such as some regularization skills [2, 3], Newton and modified Newton method [3–5], and other strategies like adaptive finite element [5]. However, using diffusion equation to describe the photon transportation has its limitations in some special cases and solving it accurately is also very difficult [6]. Monte Carlo (MC) approach is always employed to simulate the photon propagation for its accuracy and flexibility [7]. But the time-consuming nature made it seldom used in reconstruction field.

Based on traditional MC method, a table-based random sampling (TBRS) method [8] was developed by Xiaomeng Zhang in our lab, which could remarkably accelerate the computation while keeping the accuracy of MC. In this paper with the TBRS algorithm, the method that simulates the photon transportation, an improved LM algorithm of BP neural network, is used to calculate the position of bioluminescent source approximately, since BP neural network is effective in finding the nonlinearity between the inputs and the outputs, and LM algorithm will speed up the process of training.

## 2. METHODOLOGY

### 2.1. Scheme of the TBRS algorithm

The TBRS algorithm is based on a table to find a process in obtaining the positions and directions of scattering photons [8]. This table records a photon's successive $N$ steps of transportation by including the position and direction of the photon during each scattering. For any consecutive $n$ ($n \ll N$) steps in the $N$ steps of photon movement, the TBRS algorithm suggests a possible state of continuous $n$-step transportation. Thus, TBRS simulation can be started based on the table we have built. With the help of the table, we can randomly take out the continuous $n$ steps from the table and obtain the change of position and direction from one position to the other one within these $n$ steps. Then, it is added to the position and direction of the photon in site 1, the initial position of the photon, through the mapping principal illustrated in Figure 1(a) . Hence, the new position and direction of the photon in site 2 can be obtained.

With the method as mentioned above, the $n$ steps of a photon's transportation are simplified to one step in the

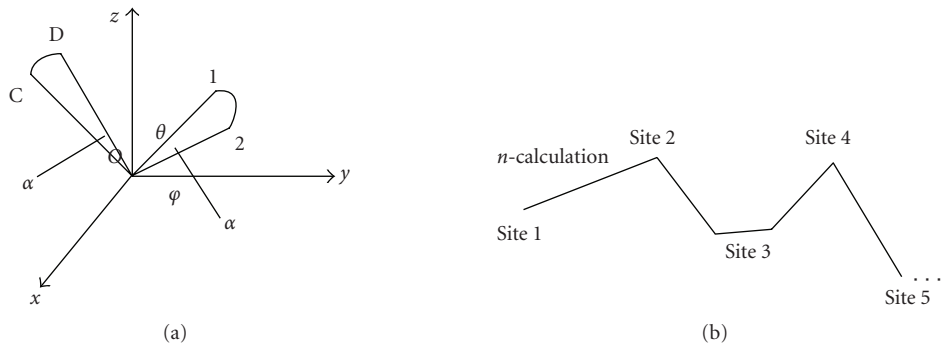


Figure 1: The mapping principle of TBRS is shown in (a). The process of obtaining new sites through $n$-calculation is described in (b).

simulation. Such approach can be performed again and again to obtain site 3, site 4, and so forth. (refer to Figure 1(b)). Once the photon reaches the inside or outside boundary of the media, it may either be reflected or transmitted, which is determined by Snell's law.

The comparison between TBRS algorithm and conventional Monte Carlo algorithm shows that, with the exact same conditions (size, geometric parameters, and optical parameters of simulation media, computer configuration), the computing time of TBRS is about 40% of conventional Monte Carlo method [8].

### 2.2. The application of backpropagation neural network to the reconstruction

To estimate the bioluminescent source position, we propose an approach based on artificial neural network. It is one of the most active methods in the realm of intelligence control, especially in finding the nonlinearity between the inputs and the outputs even in the absence of enough information about the relationship between them [9].

The first step of the method is to generate proper number of training data, in which the source position is randomly selected and varies in each simulation. TBRS method is employed here to simulate the measurements as it has the accuracy similar to that of Monte Carlo while more timesaving than it. The results obtained from the TBRS are used as the actual measurement data to train the network in the process of reconstruction.

Here we use a single hidden layer of back propagation neural network method where the input layer comprises the actual measurement data, and the output layer is the position of the source, which is in the term of 3 coordinate values.

We consider the training error to be the sum over output units of the squared difference between the desired output $t_k$ and the actual output $z_k$. So, we can define a criterion function as

$$J(w) = \frac{1}{2}\sum_{k=1}^{3}(t_k - z_k)^2, \tag{1}$$

where $(t_1, t_2, t_3)$ is the actual coordinate of the source position, the desired output in the process of training, while $(z_1, z_2, z_3)$ is the network's output, which can be adjusted each time until $J(\omega)$ approaches the given limit.

Once $J(\omega)$ drops to a value lower than the error limit through the adjustment of $\omega$, the training ceases and the network is determined. When the actual measurement data is inserted to the input layer, the source position can be obtained.

### 2.3. Improved Levenberg Marquardt algorithm of back propagation neural network

In order to speed up the learning process and reduce the training time, we should improve the traditional BP algorithm. Here, we use Levenberg Marquardt (LM) algorithm, a fast optimization algorithm that combines gradient descent method with Gauss-Newton method. It has not only the character of local convergence in Gauss-Newton method, but also the character of global convergence in gradient descent method [10]. As a result, it can be used to solve our reconstruction problem as an improvement of BP method.

Let $x^{(k)}$ be the weight vector of the kth iteration. The new vector $x^{(k+1)}$ can be written as

$$x^{(k+1)} = x^{(k)} + \Delta x. \tag{2}$$

According to Newton method, we get

$$\Delta x = -\left[\nabla^2 E(x)\right]^{-1}\nabla E(x), \tag{3}$$

where $\nabla^2 E(x)$ is called the Hessian matrix of the error criterion function $E(x)$ and, $\nabla E(x)$ is called the gradient of $E(x)$.

The error criterion function is $E(x) = (1/2)\sum_{i=1}^{N} e_i^2(x)$, where $e_i(x)$ is the error between the ith output and the $i$th target value

$$\begin{aligned} \nabla E(x) &= J^T(x)e(x), \\ \nabla^2 E(x) &= J^T(x)e(x) + J(x), \end{aligned} \tag{4}$$

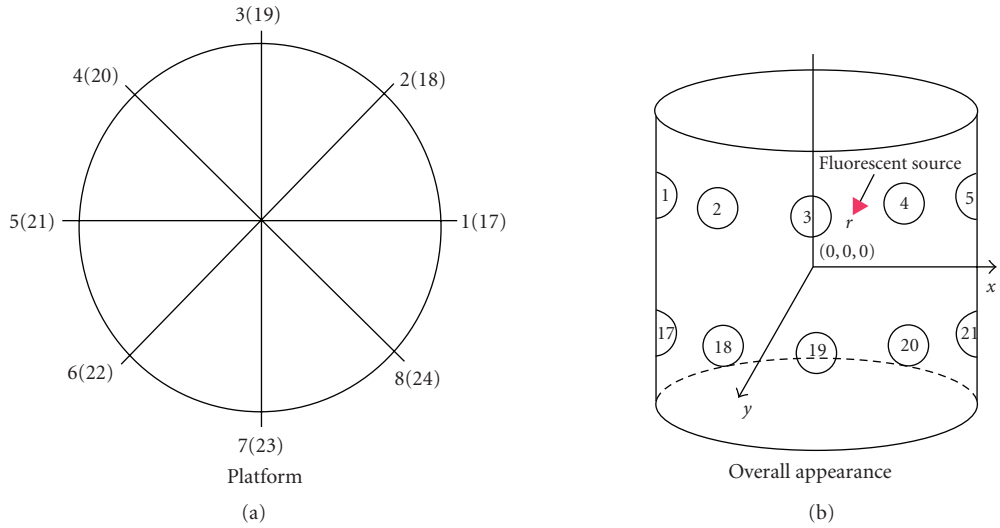


FIGURE 2: Cylinder phantom: platform and overall appearance.

where $J(x)$ is called Jacobian matrix, as

$$J(x) = \begin{vmatrix} \frac{\partial e_1(x)}{\partial x_1} & \frac{\partial e_1(x)}{\partial x_2} & \cdots & \frac{\partial e_1(x)}{\partial x_n} \\ \frac{\partial e_2(x)}{\partial x_1} & \frac{\partial e_2(x)}{\partial x_2} & \cdots & \frac{\partial e_2(x)}{\partial x_n} \\ & \cdots & & \\ & \cdots & & \\ \frac{\partial e_N(x)}{\partial x_1} & \frac{\partial e_N(x)}{\partial x_2} & \cdots & \frac{\partial e_N(x)}{\partial x_n} \end{vmatrix}. \quad (5)$$

For the Gauss-Newton method, we get

$$\Delta x = -\left[J^T(x)J(x)\right]^{-1}J(x)e(x) \quad (6)$$

while LM is an improved Gauss-Newton method, the formation of which is

$$\Delta x = -\left[J^T(x)J(x) + \mu I\right]^{-1}J(x)e(x), \quad (7)$$

where $\mu$ is the learning factor and $I$ is the unit matrix. The basic steps of this method are as follows.

(i) Set the initial $x^{(k)} = x_0$, and take a large setting value of $\mu$.

(2) Calculate error criterion function $E(x^{(k)})$.

(3) If the function $E$ is less than target or the number of training epochs reaches the fixed number, stop the training, else go on.

(4) Update $x^{(k)}$ to $x^{(k+1)}$ according to Equations (2) and (7).

(5) If $|E(x^{(k+1)})| \leq |E(x^{(k)})|$, then make $\mu^{(k+1)} = \alpha\mu^{(k)}$, where $0 < \alpha < 1$ else make $\mu^{(k+1)} = \beta\mu^{(k)}$ where $\beta > 1$. Go back to ②.

## 3. SIMULATION

Simulations were conducted in a homogeneous media as shown in Figure 2, in which the platform is shown on the left-hand side, and on the right-hand side is its overall appearance.

The cylinder, which the center is set at coordinate (0, 0, 0), has a height of 30 mm and 12 mm as the base radius. Each detector has a radius of 1 mm and the centers of the detectors are on the $z$-plane of $z = 6$, and $z = -6$, respectively. The detectors in the two layers are numbered anticlockwisely (1–8, 17–24). Inside the cylinder, there is an absorptive sphere that has different absorption coefficient from the reference medium. To simplify the problem, the fluorescent source is assumed as a point source.

### 3.1. Simulation in 2D

In the first part of our simulation, we consider the estimation of source on the $z$-plane ($z = 6$) and use the eight detectors in this plane to reconstruct the source position. We generate 10 groups of source positions randomly on the $z$-plane of $z = 6$. For every source position, we get other 3 positions of its symmetrical position of $x$-axis, $y$-axis, and the center of the circle. For example, we randomly generate one coordination of (a, b, 6) and also get (a, -b, 6), (-a, b, 6), and (-a, -b, 6). Totally we get 40 data, each of which will be used later as the output of neural network during the process of training. Each time we use one of these 40 data to generate the information of eight detectors' (1–8) photon numbers through TBRS. Each of the 40 data we get by means of TBRS is used as the input of neural network that corresponds to the output. We generate other 30 coordinates on the same plane, as well as the information got by means of TBRS, as the testing samples. The 30 source positions for the test are selected every 36° on the circle of radius = 3, 6, and 9. When training is completed, we can use the testing samples to check out whether the network built by training works well in estimating the source position.

When testing the new data, we define the term of "correct testing samples within the range of maximal allowable error." When the distance between point coordinate calculated through the trained network and the actual one is smaller than 2.4 mm, we say the testing sample is correct. We also

Table 1: Estimation of source position on the $z$-plane of $z = 6$.

| Photon numbers | Number of training samples | Number of testing samples | Number of correct testing samples (maximal allowable error = 10%) | Maximal distance (mm) |
|---|---|---|---|---|
| 10 000 000 | 40 | 30 | 30 | 2.18 |

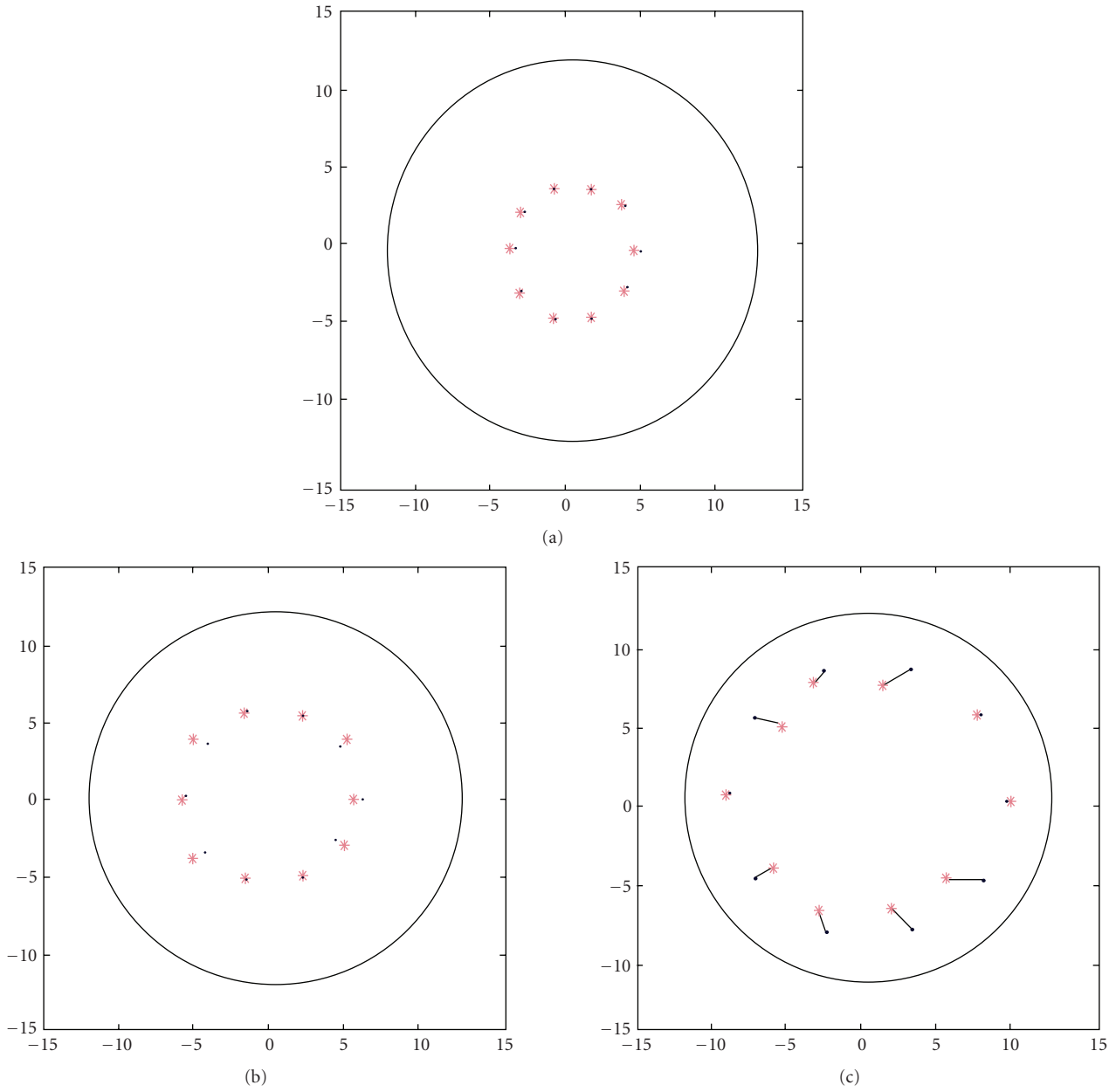


Figure 3: The comparison results between the estimated points and the actual ones.

define the maximal allowable error as the ratio of the distance mentioned above to the diameter of the cylinder, 24 mm. Therefore, when the distance mentioned above is 2.4 mm, the maximal allowable error is 10%. Table 1 shows the result of improved LM algorithm of BP neural network simulation within the range of 10% allowable error. Figure 3 shows the distribution of the 30 samples.

### 3.2. Simulation in 3D

In the second part of our simulation, the coordinate $(x, y, z)$ of source position is set randomly in a particular range. And we use all 16 detectors' photon numbers, since only 8 of them in $z = 6$ or $z = -6$ may not determine the unique source position in 3D. In order to get higher accuracy of source

Table 2: Estimation of source position in the particular region.

| | Source point region (cm) | Number of training samples | Number of testing samples | Number of correct testing samples (maximal allowable error = 10%) | Maximal distance (mm) |
|---|---|---|---|---|---|
| Simulation1 in 3D | $-5 < x < 5, -5 < y < 5, -5 < z < 5$ randomly selected | 20 | 40 | 31 | 7.7 |
| Simulation2 in 3D | $0 < x < 10, -5 < y < 5, -5 < z < 5$ randomly selected | 20 | 40 | 35 | 5.9 |

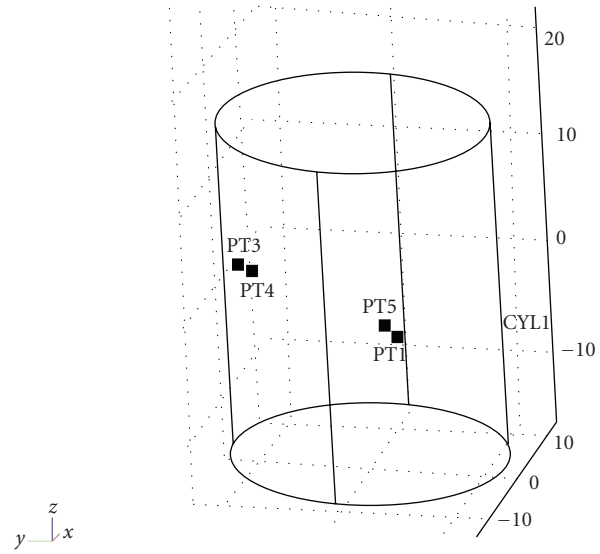


Figure 4: Two estimations of source position in the second simulation we select.

position in the finite times of training, we should only select part of the cylinder instead of the whole region. When testing the new data that is also selected randomly in the same region as the training one, the maximal allowable error is defined the same as the first part of simulation. The result is shown in Table 2. We just select two results of estimation of source position to express our expected estimation more clearly (see Figure 4). It has proved to be a good result since it is hard to discriminate between the actual source position and the estimated one in 3-dimension.

## 4. DISCUSSION

The results have shown that backpropagation neural network can be implemented to position the source, though only in a particular region of the whole cylinder. The estimated source position can mostly be located in an acceptable range of error.

The first part of our reconstruction shows an especially good result due to our tactical selection of training samples. Not only does the result prove that backpropagation neural network can be implemented in the estimation of source position in 2-dimension, but it also presents a reliable selection of training samples, that is, to train one point as well as its other three symmetric points in the 2-dimension plane.

The result of our second part of simulation also shows a high accuracy of estimation, represented by its approximately 80% accuracy of the testing sample. The difference between the two correct rates of testing sample shows us that the nearer the region is to the detectors, the higher accuracy we get when testing, since the source point in Simulation 2 is closer to the detectors than it is in Simulation 1. From the result, we could see that it is possible that such region is apparently closer to some of the detectors that may make it easier for the neural network to learn in the process of training.

Actually, the shapes of training and testing region in the three simulations above are not as important as the dimension of it. In the second part of our simulation, we choose a cube region for training and testing just for the purpose that we can generate random numbers in our programing code more conveniently. We can also choose other shapes such as the cylinder, the sphere, and so forth. The dimension of the region is more pivotal, for a broad range of region would increase the difficulty in training. The $10 \times 10 \times 10$ dimension in our simulation goes through many attempts in trying to make a balance between the low-convergence speed of training and the high accuracy of testing. On the other hand, we choose the whole circle plane as the region for training in our first part of simulation since it is much easier for network to learn in a lower dimension.

From the testing results, we can see that a high rate of accuracy was obtained after only forty training samples in the first part and twenty ones in the second part of our simulations. This demonstrates that the implementation of LM algorithm in BP neural network could make the convergence speed of training faster and the result of test more accurate. This method can be extended to solve the problem in which the source's shape is more complex and indefinite.

## ACKNOWLEDGMENTS

This work is partially supported by the National Nature Science Foundation of China, the Tsinghua-Yue-Yuen Medical Science Foundation, the National Basic Research Program of China, and the Special Research Fund for the Doctoral Program of Higher Education of China.

## REFERENCES


[1] G. Wang, W. Cong, Y. Li, et al., "Recent development in bioluminescence tomography," in *Proceedings of the 3rd IEEE International Symposium on Biomedical Imaging: From Nano to Macro, (ISBI '06)*, pp. 678–681, Arlington, Va, USA, 2006.

[2] G. Wang, W. Cong, D. Kumar, et al., "In vivo mouse studies with bioluminescence tomography," *Optics Express*, vol. 14, no. 17, pp. 7801–7809, 2006.

[3] W. Cong, G. Wang, D. Kumar, et al., "Practical reconstruction method for bioluminescence tomography," *Optics Express*, vol. 13, no. 18, pp. 6756–6771, 2005.

[4] X. Gu, Q. Zhang, L. Larcom, and H. Jiang, "Three-dimensional bioluminescence tomography with model-based reconstruction," *Optics Express*, vol. 12, no. 17, pp. 3996–4000, 2004.

[5] Y. Lv, J. Tian, W. Cong, et al., "A multilevel adaptive finite element algorithm for bioluminescence tomography," *Optics Express*, vol. 14, no. 18, pp. 8211–8223, 2006.

[6] I. V. Yaroslavsky, H. J. Schwarzmaier, A. N. Yaroslavsky, and V. V. Yuchin, "Radiative transfer equation and its diffusion approximation in the frequency domain technique: a comparison," in *Photon Transport in Highly Scattering Tissue*, vol. 2326 of *Proceedings of SPIE*, pp. 465–474, Lille, France, September 1995.

[7] H. Li, J. Tian, F. Zhu, et al., "A mouse optical simulation environment (MOSE) to investigate bioluminescent phenomena in the living mouse with the Monte Carlo method," *Academic Radiology*, vol. 11, no. 9, pp. 1029–1038, 2004.

[8] X. Zhang and J. Bai, "A table-based random sampling simulation for bioluminescence tomography," *International Journal of Biomedical Imaging*, vol. 2006, Article ID 83820, 8 pages, 2006.

[9] T. O. Duda and P. E. Hart, "Multilayer neural networks," in *Pattern Classification*, chapter 6, p. 287, Wiley-Interscience, New York, NY, USA, 2nd edition, 2000.

[10] L.-Q. Li, S.-L. Wang, and B.-T. Zhao, "Improved Levenberg-Marquardt algorithm for BP neural network and its application in predicting the particle impact damping," *Journal of University of Shanghai for Science and Technology*, vol. 28, no. 4, pp. 331–333, 2006.

Hindawi Publishing Corporation
International Journal of Biomedical Imaging
Volume 2007, Article ID 84724, 9 pages
doi:10.1155/2007/84724

*Research Article*

# A Penalized Linear and Nonlinear Combined Conjugate Gradient Method for the Reconstruction of Fluorescence Molecular Tomography

**Shang Shang, Jing Bai, Xiaolei Song, Hongkai Wang, and Jaclyn Lau**

*Medical Engineering and Health Technology Research Group, Department of Biomedical Engineering, Tsinghua University, Beijing 100084, China*

Received 22 January 2007; Accepted 28 June 2007

Recommended by Jie Tian

Conjugate gradient method is verified to be efficient for nonlinear optimization problems of large-dimension data. In this paper, a penalized linear and nonlinear combined conjugate gradient method for the reconstruction of fluorescence molecular tomography (FMT) is presented. The algorithm combines the linear conjugate gradient method and the nonlinear conjugate gradient method together based on a restart strategy, in order to take advantage of the two kinds of conjugate gradient methods and compensate for the disadvantages. A quadratic penalty method is adopted to gain a nonnegative constraint and reduce the illposedness of the problem. Simulation studies show that the presented algorithm is accurate, stable, and fast. It has a better performance than the conventional conjugate gradient-based reconstruction algorithms. It offers an effective approach to reconstruct fluorochrome information for FMT.



## 1. INTRODUCTION

Light with wavelength in the near-infrared range can propagate a few centimeters through the tissue because of low tissue absorption in the spectral of "near-infrared window." This finding has encouraged the development of fluorescence techniques to visualize specific biochemical events inside living subjects [1, 2]. In recent years, a great development has happened to the fluorescence molecular tomography (FMT), a technique that resolves molecular signatures in deep tissue using fluorescent probes or markers [1, 3–6]. Tissue is illuminated by a series of excitation light in FMT; multiple measurements for the fluorescent emission light are collected from the tissue surface to resolve and quantify fluorochromes deep inside the tissue. With great potential, FMT has become a promising imaging modality for in vivo small animal imaging [1, 2].

Several reconstruction approaches for FMT have been proposed. Most of them are based on the diffusion model [6–10]. The model can be solved by methods such as finite difference method [8], finite element method [6], adaptive finite element method [11], and statistical method [12]. A weighting matrix can be obtained from the forward model, which describes the influence of each volume element on the detector readings. Generally, the inverse reconstruction problem of FMT is to find the fluorescent source distribution in the target tissue based on the precalculated weighting matrix and the measured data. Since the data measured from the tissue surface is far less than the number of unknown points inside the tissue, the reconstruction problem is illposed, and the solution is sensitive to noise as well as measurement error. Several algorithms have been reported, such as the modified Newton method-based optimization scheme [13] and the Born-type approximation techniques [14]. The conjugate gradient (CG) methods, which need less storage and computation, are favorable for the problems with large-dimension data. They have been reported to be adopted successfully in the reconstruction algorithms for imaging modalities such as the positron emission tomography (PET) [15–17] and diffusion optical tomography (DOT) [18]. Normally, two different kinds of CG with different properties are being used under different conditions. They are the linear CG method (L-CG) and the nonlinear CG method (N-CG) [19]. There is a remarkable point that L-CG and N-CG have reciprocal properties. Combining them together may generate an improved algorithm, which has the advantages of both of them.

In this paper, a penalized linear and nonlinear combined conjugate gradient method (PLN-CG) for the reconstruction of FMT is presented. The L-CG method and the N-CG method are employed separately at different period based on a restart strategy, in order to exert their advantages while compensating for their disadvantages. Besides, a quadratic penalty method is adopted to give the result a nonnegative constraint, as well as reduce the uncertainty and illposedness of the problem. Simulation studies show that the PLN-CG algorithm can give a more accurate and more stable result for the reconstruction in FMT with less computation. Detailed description of the PLN-CG algorithm can be found in Section 3. Section 2 gives a general review of the forward and inverse problems in FMT, including the conventional CG-based reconstruction method. Simulation experiments are presented in Section 4 to demonstrate the validity and efficiency of the proposed algorithm. Section 5 summarizes the main results and gives a general discussion.

## 2. THEORY AND BACKGROUND

### 2.1. Forward model in FMT

When an external excitation light source works at continuous wave mode (CW mode), the following diffusion equation can be employed to model the propagation of the excitation light and the fluorescent emission light [6–10]:

$$\begin{aligned}\nabla\cdot\left[D_x(\mathbf{r})\nabla\Phi_x(\mathbf{r})\right]-\left[\mu_{ax}(\mathbf{r})+\mu_{af}(\mathbf{r})\right]\Phi_x(\mathbf{r})&=-\Theta_s\delta\left(\mathbf{r}-\mathbf{r}_{sk}\right),\\ \nabla\cdot\left[D_m(\mathbf{r})\nabla\Phi_m(\mathbf{r})\right]-\mu_{am}(\mathbf{r})\Phi_m(\mathbf{r})&=-\Phi_x(\mathbf{r})\eta\mu_{af}(\mathbf{r}),\end{aligned}\tag{1}$$

where $\mathbf{r}$ is the position vector belonging to the image region $\Omega$. $\Phi_{x,m}(\mathbf{r})$ represents the photon density at $\mathbf{r}$ for the excitation light (subscript $x$) or the fluorescent emission light (subscript $m$). $D_{x,m}(\mathbf{r})$ is defined as the diffusion coefficient

$$D_{x,m}(\mathbf{r})=\left(3\left(\mu_{ax,m}(\mathbf{r})+(1-g)\mu_{sx,m}(\mathbf{r})\right)\right)^{-1},\tag{2}$$

where $\mu_{ax,m}(\mathbf{r})$ and $\mu_{sx,m}(\mathbf{r})$ are the absorption and scattering coefficients, respectively. $g$ is the anisotropy parameter. The absorption of the excitation light due to fluorophores is described as $\mu_{af}(\mathbf{r})$ and the fluorescent yield $\eta\mu_{af}(\mathbf{r})$ is required for fluorescence parameter.

### 2.2. The inverse reconstruction problem in FMT

In this work, the finite element method is used to solve the forward model. Detailed description of the finite element method for the FMT forward problem can be found in [6, 11]. Based on the finite element solution of the forward problem, (1) is transformed into a linear matrix equation as follows:

$$\mathbf{W}\mathbf{x}=\mathbf{I},\tag{3}$$

where $\mathbf{x}$, an $N\times 1$ vector, denotes the real fluorescent source distribution to be reconstructed. $\mathbf{I}$, a $M\times 1$ vector, is the emission data computed from the measurement at the surface of the tissue. And $\mathbf{W}$, a $M\times N$ matrix, is the weighting matrix generated from the forward model. Generally, the inverse problem for FMT is to find the fluorescent source distribution $\mathbf{x}$ in the target tissue from the measured data $\mathbf{I}$ and the precalculated matrix $\mathbf{W}$. As mentioned before, the problem in (3) is quite illposed and undetermined.

### 2.3. The L-CG and N-CG method

The implementation of CG in image reconstruction field is generally in two ways. CG is one of the most useful methods for solving large linear systems of equations with symmetric and positive definite parameters, as it is called L-CG [19]. L-CG can be employed in FMT reconstruction by transforming equation (1) into a standard linear system. Since all parameters of each step in L-CG can be obtained from the value of the last step by iterative functions, the computation and storage of the algorithm are reduced. Besides, with pertinence, L-CG converges fast and has a good orientating ability. However, it is brittle and sensitive to noise. The requirement of the standard form of the problem in L-CG limits the implementation of the regularization and penalty methods, which are quite important for the illposed problem in FMT reconstruction. Thus, the CG method for nonlinear optimization problems, namely N-CG, which is more flexible to work along with the regularization and penalty methods and has a better capability to work under noise, is used widely for image reconstruction [15, 17]. According to the least-squares (LS) rule, problem (3) can be changed into a nonlinear optimization problem as follows:

$$\min\phi(\mathbf{x})=\frac{1}{2}\|\mathbf{I}-\mathbf{W}\mathbf{x}\|^2+\eta(\mathbf{x}),\tag{4}$$

where $\eta(\mathbf{x})$ is the regularization or penalty term chosen on various purposes. Then the N-CG method can be adopted to find the optimal solution of (4). However, defects exist in N-CG. This method is more computationally expensive than L-CG, resulting in more time consuming for each iteration. Besides, it converges slowly [20]. Nevertheless, it is noticed that the properties of N-CG and L-CG are reciprocal. Thus, combining N-CG and L-CG together may generate an improved algorithm, which can get a higher speed and accuracy from L-CG as well as a good antinoise capability and the flexibility from N-CG. Therefore, an improved CG-based algorithm for FMT reconstruction, penalized linear and nonlinear combined conjugate gradient method (PLN-CG), was developed according to this consideration. The main scheme of the algorithm is presented in the following section.

## 3. A PENALIZED LINEAR AND NONLINEAR COMBINED CG METHOD

### 3.1. Searching the rough region using L-CG

The searching process for the optimal solution $\mathbf{x}^*$ in PLN-CG begins with an initial guess $\mathbf{x}_0$, and takes a steepest descent first step. The sketch of the scheme is shown in Figure 1.

At first, the search is general and the effect of noise is low, so L-CG is employed to find the rough region of the

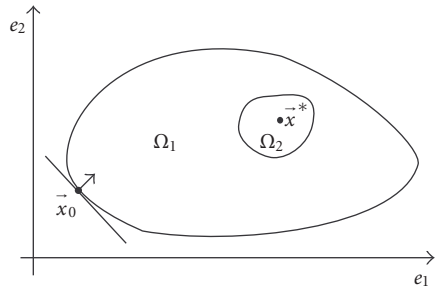


Figure 1: The sketch of the combined L-CG and N-CG schemes.

optimal solution $\mathbf{x}^*$, that is, $\Omega_2$. Because L-CG has a better orientating ability, and needs less computation, it can find $\Omega_2$ faster and more accurately, while it does not have to expose its fragility under noise.

Transformation has to be made to (3) to make it a standard linear system with symmetric positive definite coefficient matrix. The optimal solution of the LS problem described in (4) satisfies the normal equation as follows:

$$\mathbf{W}^T\mathbf{W}x = \mathbf{W}^T\mathbf{I}, \tag{5}$$

where $\mathbf{W}^T$ is the transpose of $\mathbf{W}$. Thus

$$\mathbf{W}^*\mathbf{x} = \mathbf{I}^*, \tag{6}$$

where $\mathbf{W}^* = \mathbf{W}^T\mathbf{W}$, is an $N \times N$ symmetric matrix. The reconstruction problem has become a standard linear one, as is required by L-CG.

Starting from an initial guess $\mathbf{x}_0$, the solution can be updated iteratively by

$$\mathbf{x}_{k+1} = \mathbf{x}_k + \alpha_k\mathbf{p}_k, \tag{7}$$

where $\alpha_k$ is the step size

$$\alpha_k = \frac{\mathbf{r}_k^T\mathbf{r}_k}{\mathbf{p}_k^T\mathbf{W}^*\mathbf{p}_k}, \tag{8}$$

and $\mathbf{r}_k$ is the gradient of each step. It is defined in L-CG as the residue of the linear system, which is obtained iteratively by

$$\mathbf{r}_{k+1} = \mathbf{r}_k + \alpha_k\mathbf{W}^*\mathbf{p}_k, \tag{9}$$

where $\mathbf{p}_k$ is the searching direction and

$$\begin{aligned} \mathbf{p}_{k+1} &= -\mathbf{r}_{k+1} + \beta_{k+1}\mathbf{p}_k, \\ \beta_{k+1} &= \frac{\mathbf{r}_{k+1}^T\mathbf{r}_{k+1}}{\mathbf{r}_k^T\mathbf{r}_k}. \end{aligned} \tag{10}$$

The L-CG searching iteration process will cease when $\mathbf{x}_k$ enters the region $\Omega_2$. The definition of the region $\Omega_2$ is determined by a restarting parameter, which is described in the following section.

### 3.2. The restart strategy

The restart strategy is a modification that is often used in nonlinear conjugate gradient procedures [19, 21]. The general scheme is to restart the iteration and take a steepest descent step according to some predetermined conditions. Restarting serves to periodically refresh the algorithm, erase old information that may not be beneficial or even harmful, and renew the initial guess $\mathbf{x}_0$ at every restarting time for the new iteration process.

We adopt a restart strategy in the PLN-CG scheme described as follows:

$$\left|\mathbf{r}_k\right| = \left|\mathbf{r}_{k-1} + \alpha_{k-1}\mathbf{W}^*\mathbf{p}_{k-1}\right| \le \delta, \tag{11}$$

where $\mathbf{r}_k$ represents the gradient of $\phi(\mathbf{x}_k)$. When $|\mathbf{r}_k|$ satisfies (11), it means that the $\mathbf{x}_k$ obtained at current iteration has entered the small region $\Omega_2$ around $\mathbf{x}^*$. Then, a steepest descent step is taken, using the gradient direction at current point as the searching direction. At the same time, a new iteration process with the N-CG method begins, using $\mathbf{x}_k$ as the initial guess $\mathbf{x}_0$. The experiential typical value for $\delta$ is between $10^{-3}$ and $10^{-5}$. Normally, we choose $10^{-4}$ for practical use.

### 3.3. Use of the N-CG method

After entering $\Omega_2$, the searching result is getting quite closer to the optimal solution, so the effect of noise has to be taken into consideration. Besides, the uncertainty of the searching has increased. Thus, the method has been shifted to N-CG, which can work better with noisy data. Besides, N-CG can introduce the penalty or regularization method to gain a constraint as well as to reduce the illposedness.

Now, problem (3) is transformed into a nonlinear optimization problem:

$$\min \phi(x) = \frac{1}{2}\|\mathbf{I} - \mathbf{W}\mathbf{x}\|^2 + \eta(\mathbf{x}), \tag{12}$$

where $\eta(\mathbf{x})$ is a penalty term which will be discussed in Section 3.4.

The N-CG method differs from L-CG mainly in two ways. Firstly, rather than using a standard iterative function to find the step length $\alpha_k$, a line search method is used to identify an approximate minimum of the nonlinear function $\phi(\mathbf{x})$ along the searching direction $\mathbf{p}_k$ [15, 17, 19]. Secondly, the gradient of $\phi(\mathbf{x})$ in L-CG is simply the residue of the linear system that can be obtained iteratively. While for N-CG, it must be replaced by the gradient of the nonlinear objective $\phi(\mathbf{x})$, that is, $\nabla\phi(\mathbf{x})$.

Thus, using the $\mathbf{x}_k$ obtained from L-CG as the initial guess $\mathbf{x}_0$ for N-CG, the solution is updated iteratively:

$$\mathbf{x}_{k+1} = \mathbf{x}_k + \alpha_k\mathbf{p}_k, \tag{13}$$

where $\alpha_k$ is the step size that is computed by a line search method,

$$\min f(\mathbf{x}_k + \alpha\mathbf{p}_k) \quad \text{s.t. } \alpha \ge 0, \tag{14}$$

where $\mathbf{p}_k$ is the searching direction and

$$\begin{aligned} \mathbf{p}_{k+1} &= -\mathbf{r}_{k+1} + \beta_{k+1}\mathbf{p}_k, \\ \beta_{k+1} &= \frac{\mathbf{r}_{k+1}^T(\mathbf{r}_{k+1} - \mathbf{r}_k)}{\mathbf{r}_k^T\mathbf{r}_k}, \end{aligned} \tag{15}$$

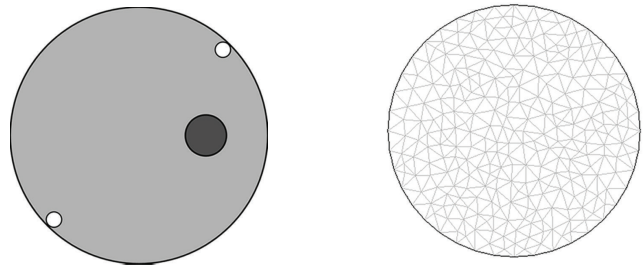

(a) (b)

Figure 2: (a) Configuration of the simulation experiment using two excitation sources. The object is homogeneous, with a fluorophore (designated with •) imbedded in it. Two excitation sources (designated with ∘) are placed around the inner surface of the object. (b) Mesh in the forward FEM model.

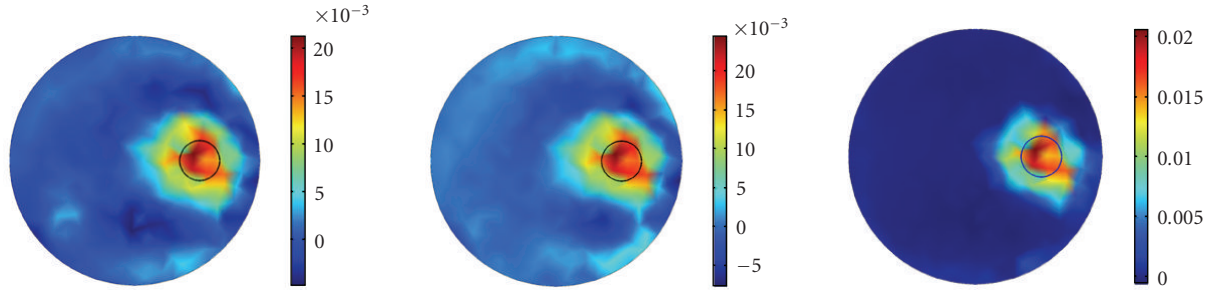


(a) N-CG (b) L-CG (c) PLN-CG

Figure 3: Images reconstructed with different methods. (a) N-CG, (b) L-CG, (c) PLN-CG. All results were obtained with a hundred iterations, $\gamma$ was chosen to be 50. A zero vector was used as the initial guess. The small circle in each figure shows the real distribution of the fluorophore.

where $\mathbf{r}_k$ is the gradient of the objective function $\phi(\mathbf{x})$ at current point, that is,

$$\mathbf{r}_k = \nabla\phi(\mathbf{x}_k). \tag{16}$$

### 3.4. The nonnegative penalty

It is known that a major problem of the conventional gradient-based methods is that they are mainly designed for unconstrained problems, but the fluorescent source distribution in the biological tissue has to be constrained to a nonnegative region [16, 22]. Here, a quadratic penalty method [15, 19] is adopted to give the problem a nonnegative constraint.

Consider the penalty function described below

$$\eta = \gamma \sum_i x_i^2 u(-x_i), \tag{17}$$

where $x_i$ is the $i$th element of $\mathbf{x}$, $u(x)$ is the unit step function. During the searching procedure, when the searched result $\mathbf{x}$ at current iteration has negative values, the penalty term will be increased. In this way, it will penalize $\mathbf{x}$ and force it to go back. $\gamma$ is a penalty weighting parameter, which will gradually become zero as the iteration number increases. Thus, the solution of the new unconstrained problem in (12) with the penalty term (17) will approach the solution of the original problem in (3). The value of $\gamma$ will be discussed experimentally in Section 4.1.3.

Set an initial value $\mathbf{x}_0$, and the restarting parameter $\delta$.
(1) Find $\mathbf{x}_k$ using L-CG method,
the gradient $\mathbf{r}_k = \mathbf{A}x_k - \mathbf{b}$, as in (9).
(2) If $\mathbf{r}_k \le \delta$, go to (3). Else, repeat (1).
(3) Restart, set $\mathbf{x}_0 = \mathbf{x}_k$, $\beta = 0$.
(4) Find the optimal solution $\mathbf{x}^*$ with N-CG method, use $\phi(\mathbf{x})$ with penalty function $\eta(\mathbf{x})$ as the objective function.

Algorithm 1: The PLN-CG scheme for FMT reconstruction.

Thus, a penalized linear and nonlinear combined conjugate gradient method is generated according to the scheme described above. The main flow of Algorithm 1 is listed below.

## 4. SIMULATIONS AND RESULTS

### 4.1. Simulations with two sources

In this experiment, a numerical model was set up to test the validity of the PLN-CG algorithm. A circular object was simulated with an outer diameter of 25 mm, which had a fluorophore with a diameter of 4 mm embedded in it. We supposed the optical property to be homogeneous, with $\mu_a = 0.005\ \text{mm}^{-1}$ and $\mu_s = 1\ \text{mm}^{-1}$. In order to show the ef-

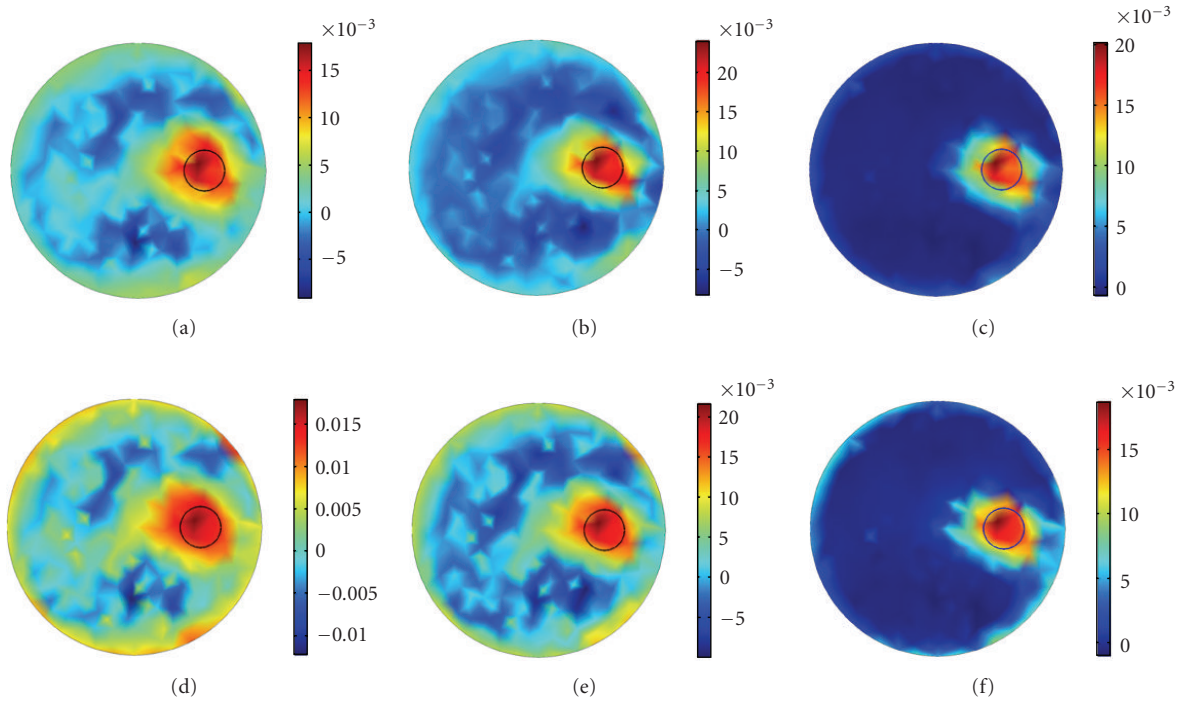


FIGURE 4: Images reconstructed with different initial guesses, using N-CG (Column 1), L-CG (Column 2), and PLN-CG (Column 3). Initial guess for (a)–(c) was an all-0.005 vector, and for (d)–(f) was an all-0.01 vector. Results were all obtained with one hundred iterations. $\gamma$ was 50 for the PLN-CG approach. The small circle in each figure shows the real distribution of the fluorophore.

ficiency of PLN-CG better, only two excitation sources were used this time. They were placed around the inner surface of the circular object (as shown in Figure 2(a)), and were turned on in turn. For each source, 32 detector readings were available through the detector fibers, which were distributed uniformly on the surface of the circular object.

The forward data were simulated by finite element method [6, 10], using a FEM light transport model in CW mode [7]. The object was divided into 518 small triangular elements and the mesh is shown in Figure 2(b). The FEM forward engine was based on COMSOL Multiphysics (Section 3.2). The reconstruction algorithm was programed in MATLAB 6.5. A computer with CPU AMD Athlon×23600+ and 512M DDRII memory was used.

Images reconstructed by N-CG, L-CG, and PLN-CG are shown in Figures 3(a), 3(b), and 3(c). All images were obtained with one hundred iterations, as the objective function would descend very slowly thereafter. The nonnegative penalty parameter $\gamma$ used for PLN-CG was 50. A zero vector was used as the initial guess for each algorithm.

It can be seen that images reconstructed by N-CG and L-CG are noisy. Negative values exist, which affect the accuracy of the results. While for PLN-CG, the values are all nonnegative, and the image is cleaner and more accurate. The computing time was about 5.02 seconds for N-CG, 0.22 second for L-CG, and 1.45 seconds for PLN-CG. It indicates that L-CG is much faster than N-CG. So helping N-CG with L-CG has tremendously reduced the computing time, as in the PLN-CG method.

#### 4.1.1. *Reconstruction using different initial guesses*

Being sensitive to the initial guess is a big disadvantage for most of the iterative approach based algorithms. It is regarded as a standard to test the stability of the algorithm.

Figure 4 shows the results reconstructed with different initial values, using N-CG (Column 1), L-CG (Column 2), and PLN-CG (Column 3), respectively. Since most elements of the original solution are zero and the quantity of the fluorochrome intensity in FMT is relatively small, a zero vector is closer to the solution of the problem and is a better choice to be the initial value (Figure 3). When the initial value is increased to 0.005 and 0.01, the reconstructed images of N-CG (Figures 4(a) and 4(d)) and L-CG (Figures 4(b) and 4(e)) become perturbed, with artifacts distributed in the background. Whereas the PLN-CG (Figures 4(c) and 4(f)) is still giving a clear result, with only a slight blur on the edge.

#### 4.1.2. *Reconstruction using noisy data*

To test the stability of the algorithm, white Gaussian noise was added to the detector readings. Figure 5 shows the images reconstructed by N-CG (Column 1), L-CG (Column 2), and PLN-CG (Column 3). The L-CG method reveals its fragility under noise. The image is perturbed when the noise level is 5% (Figure 5(e)). When the noise level is 10%, the image is totally blurred, as is shown in Figure 5(h). The N-CG method has a better performance compared with L-CG (Figures 5(i) and 5(g)). However, many artifacts exist in the images and affect the quantification of the fluorophore.

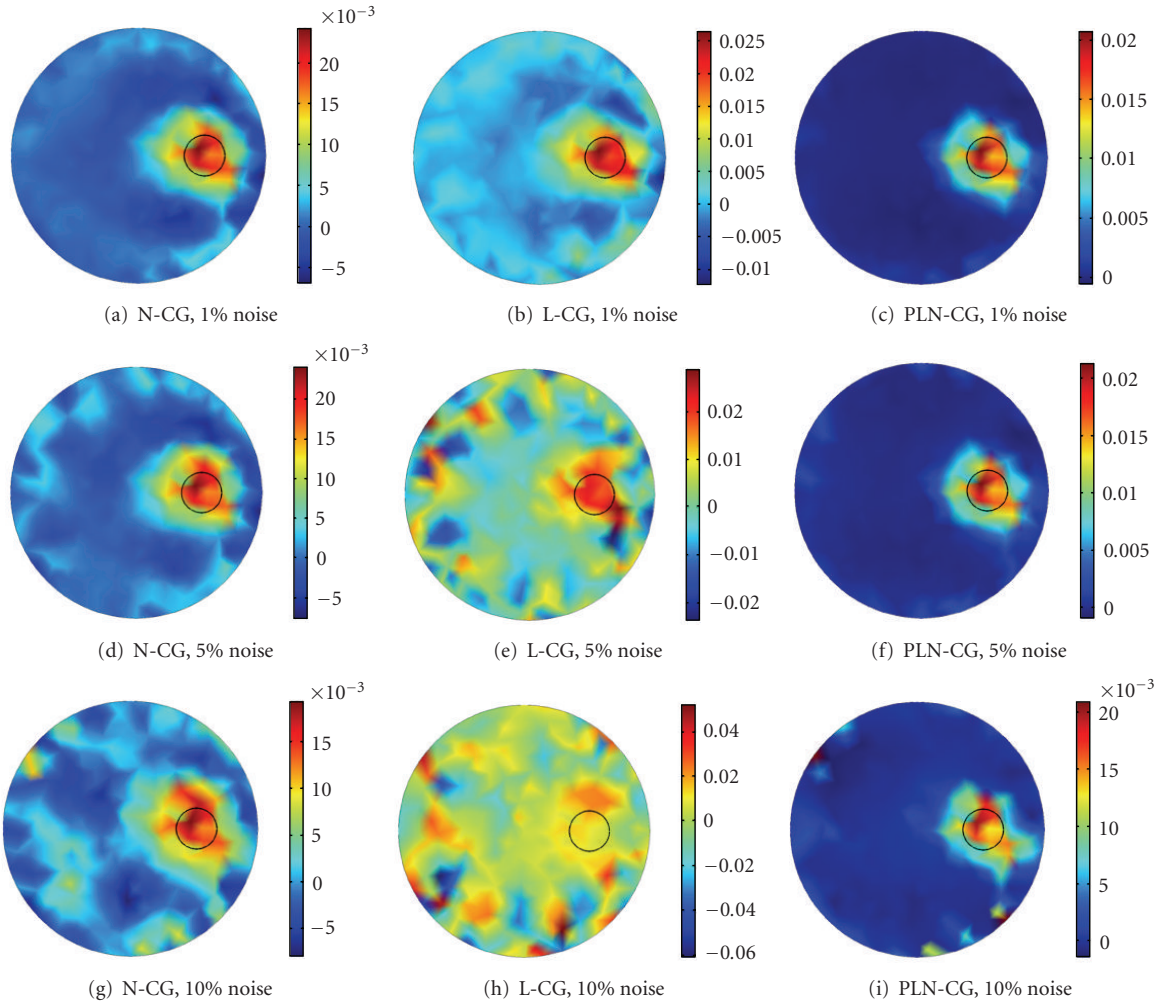


(a) N-CG, 1% noise (b) L-CG, 1% noise (c) PLN-CG, 1% noise

(d) N-CG, 5% noise (e) L-CG, 5% noise (f) PLN-CG, 5% noise

(g) N-CG, 10% noise (h) L-CG, 10% noise (i) PLN-CG, 10% noise

FIGURE 5: Images reconstructed with noisy data, using N-CG (Column 1), L-CG (Column 2), and PLN-CG (Column 3). Noise level for (a)-(c) was 1%, for (d)–(f) was 5%, and for (g)–(i) was 10%. Results reconstructed with N-CG and L-CG were obtained with one hundred and fifty iterations. For PLN-CG, when $\gamma$ was 50, the iteration number was one hundred. The small circle in each figure shows the real distribution of the fluorophore.

Whereas, images reconstructed with PLN-CG approach are clear when the noise levels are 1% (Figure 5(c)) and 5% (Figure 5(f)). When the noise level is 10%, the fluorescent source distribution is still relatively clear, with a little artifacts appearing on the edge.

#### 4.1.3. *The value of the penalty parameter $\gamma$*

When using the PLN-CG method, $\gamma$ is the weighting parameter that controls the effect of the penalty term. Figure 6 shows the images reconstructed with different $\gamma$.

It can be seen that when $\gamma$ is $10^{-3}$, the effect of the penalty term is not enough. Negative values exist and the background is not clean. Increasing $\gamma$ to 1 does produce better results (Figure 6(b)), and a further increase to $10^3$ enhances the improvement (Figure 6(c)). When $\gamma$ increases to $10^5$, the quality of the image begins to get worse (Figure 6(d)). The results show that the penalty term can work well for a large variation of $\gamma$. A typical value for $\gamma$ is 10 to$10^3$. Besides, $\gamma$ should be increased when the total iteration number increases.

In addition, rather than keeping $\gamma$ fixed, one can use different $\gamma$ according to the experiential equation [18]

$$\gamma = an^2, \tag{18}$$

where $n$ is the iteration number. $a$ is a fixed weighting parameter, which can be set to a value between $10^{-3}$ and 1. Figure 6(f) shows the images reconstructed according to (18). The iteration number was one hundred and $a$ was chosen to be 0.005.

### 4.2. *Simulations with more sources*

Simulation studies above were based on two excitation sources, in order to demonstrate the qualities of the PLN-CG approach better. When the number of sources is increased, a larger dataset can be obtained. It will improve the information content of the measurements and reduce

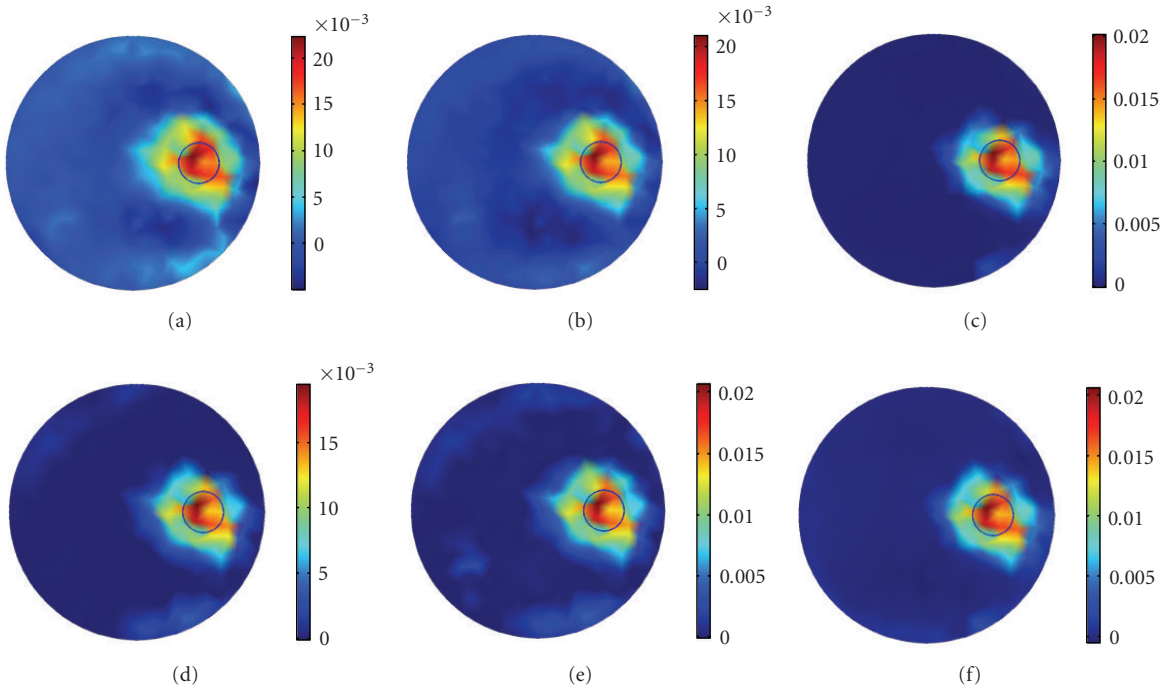


Figure 6: Reconstructed images using different $\gamma$: (a) $\gamma = 1e-3$; (b) $\gamma = 1$; (c) $\gamma = 1e3$; (d) $\gamma = 1e5$; (e) $\gamma = 1e7$; (f) $\gamma = 0.005n^2$, where $n$ is the iteration number. A zero vector was used as the initial guess for each reconstruction process, and all results were obtained with a hundred iterations. The small circle in each figure shows the real distribution of the fluorophore.

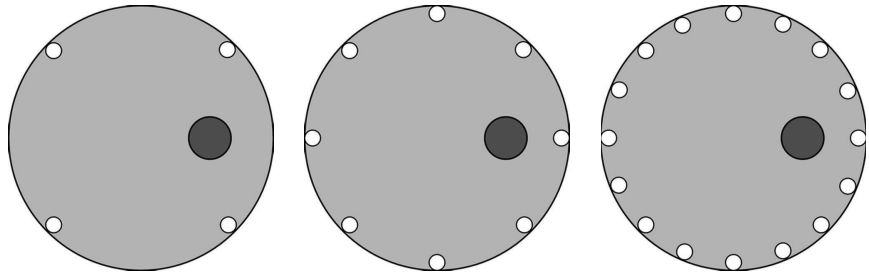


Figure 7: Configuration of the simulation experiments using more excitation sources. (a) 4 sources. (b) 8 sources. (c) 16 sources. The excitation sources are distributed uniformly around the inner surface of the object (designated with ∘). For each experiment, the object is homogeneous, with a fluorophore (designated with •) embedded in it.

the illposedness of the inverse problem [5]. Thus, in practice, FMT equipments normally use more excitation sources [3, 4]. Here, simulation experiments were designed using 4 sources (Figure 7(a)), 8 sources (Figure 7(b)), and 16 sources (Figure 7(c)), respectively.

In each experiment, sources were turned on in turn and 32 detector readings were available for each source. Results with clean data were obtained with a hundred iterations for about 2.99 seconds in the 4 sources case (Figure 8(a)). While the computing time was about 4.9220 seconds and 9.1560 seconds for 150 iterations in the 8 sources case (Figure 8(b)) and 16 sources case (Figure 8(c)), as they have a larger dataset. $\gamma$ was simply set to 50 for all cases because the difference among the iteration numbers was small. It is shown that as the source number increases, the qualities of the reconstructed images are in progress. The reconstructed fluorochrome region marked with the small black circle is more even and closer to the original value.

After the experiments using clean data described above, white Gaussian noise with a constant variance was added to the detector readings. The noise level was 10%. It is shown that the reconstructed results become clearer and better when the sources number increases from 2 (Figure 5(i)) to 4 (Figure 8(d)) and 8 (Figure 8(e)). However, when using 16 sources (Figure 8(f)), the image is not improved compared with the 8 sources case, or even worse, which defies the common sense. The reason may be that, when using clean and accurate data for the reconstruction, more datasets mean more information, whereas for the cases using noisy data, too many data may interfere with each other and counteract

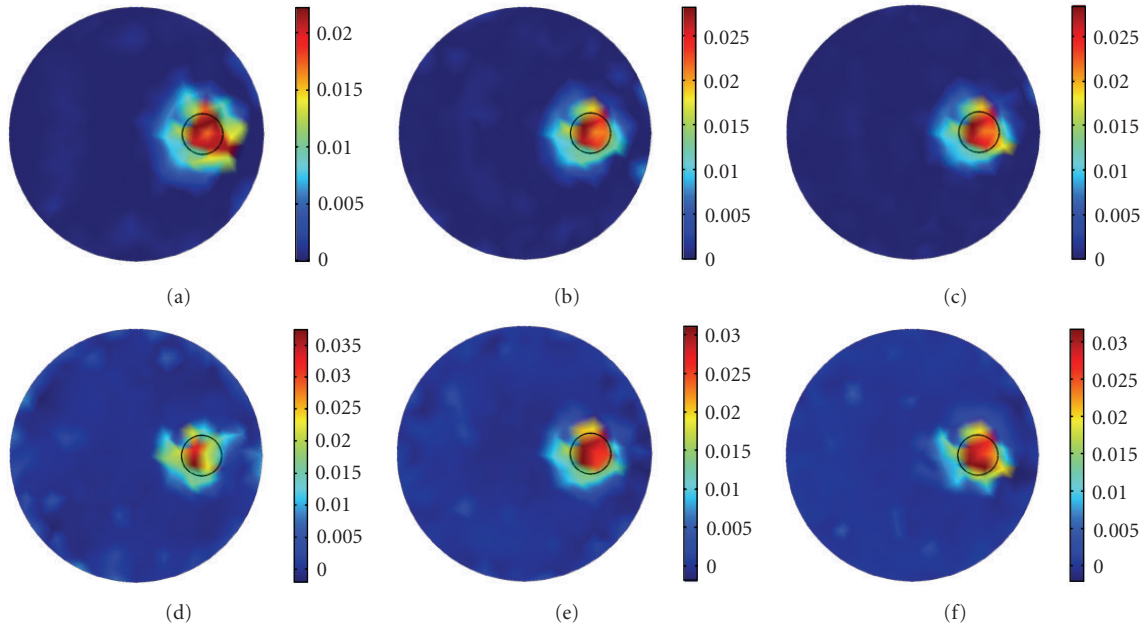


FIGURE 8: Images reconstructed in the experiments which have more excitation sources. (a) 4 sources, clean data; (b) 8 sources, clean data; (c) 16 sources, clean data; (d) 4 sources, 10% noise; (e) 8 sources, 10% noise; (f) 16 sources, 10% noise. The small circle in each figure shows the real distribution of the fluorophore.

the effect. Nevertheless, the results of this experiment further demonstrate the capability of the PLN-CG method to work under noise.

## 5. DISCUSSION AND CONCLUSION

The goal of this work was to establish a fast and accurate algorithm for FMT reconstruction, which is illposed. In order to achieve this goal, a penalized linear and nonlinear combined conjugate gradient algorithm was developed. Simulation studies have indicated that this PLN-CG method can exhibit very favorable performance and produce relatively stable behavior. Further studies show that, when using sixteen sources, the reconstruction algorithm can work under 15% noise, which is sufficient for practical use. The better performance is partly achieved by the combination of L-CG and N-CG. L-CG makes the algorithm faster and more accurate. While at the same time, N-CG gives the whole algorithm a better capacity to deal with noise. It introduces the penalty method to get a nonnegative constraint and reduce the uncertainty of the problem. The restart strategy also improves the efficiency of the algorithm by refreshing the algorithm periodically.

Further improvement can be made for the PLN-CG algorithm in future. Some kind of regularization techniques can be employed to regularize the results and smoothen the images [6]. The prior knowledge about the intensity of the fluorochrome can be used to utilize a general threshold of the reconstructed fluorescent source density to decrease the permissible region [11]. In addition, doing more restarting procedures appropriately may also upgrade the reconstruction images. Currently, we are involved in the practical use of the PLN-CG reconstruction algorithm for the ongoing FMT experiment in our laboratory.

## ACKNOWLEDGMENTS

This work is partially supported by the National Nature Science Foundation of China, the Tsinghua-Yue-Yuen Medical Science Foundation, the National Basic Research Program of China, and the Special Research Fund for the Doctoral Program of Higher Education of China.

## REFERENCES

[1] V. Ntziachristos, C. Bremer, and R. Weissleder, "Fluorescence imaging with near-infrared light: new technological advances that enable in vivo molecular imaging," *European Radiology*, vol. 13, no. 1, pp. 195–208, 2003.

[2] V. Ntziachristos, J. Ripoll, L. V. Wang, and R. Weissleder, "Looking and listening to light: the evolution of whole-body photonic imaging," *Nature Biotechnology*, vol. 23, no. 3, pp. 313–320, 2005.

[3] V. Ntziachristos and R. Weissleder, "Charge-coupled-device based scanner for tomography of fluorescent near-infrared probes in turbid media," *Medical Physics*, vol. 29, no. 5, pp. 803–809, 2002.

[4] V. Ntziachristos, C.-H. Tung, C. Bremer, and R. Weissleder, "Fluorescence molecular tomography resolves protease activity in vivo," *Nature Medicine*, vol. 8, no. 7, pp. 757–760, 2002.

[5] E. E. Graves, J. Ripoll, R. Weissleder, and V. Ntziachristos, "A submillimeter resolution fluorescence molecular imaging system for small animal imaging," *Medical Physics*, vol. 30, no. 5, pp. 901–911, 2003.

[6] A. X. Cong and G. Wang, "A finite-element-based reconstruc-

tion method for 3D fluorescence tomography," *Optics Express*, vol. 13, no. 24, pp. 9847–9857, 2005.

[7] S. R. Arridge, M. Schweiger, M. Hiraoka, and D. T. Delpy, "A finite element approach for modeling photon transport in tissue," *Medical Physics*, vol. 20, no. 2, pp. 299–309, 1993.

[8] D. Y. Paithankar, A. U. Chen, B. W. Pogue, M. S. Patterson, and E. M. Sevick-Muraca, "Imaging of fluorescent yield and lifetime from multiply scattered light reemitted from random media," *Applied Optics*, vol. 36, no. 10, pp. 2260–2272, 1997.

[9] X. Song, J. Yi, and J. Bai, "A parallel reconstruction scheme in fluorescence tomography based on contrast of independent inversed absorption properties," *International Journal of Biomedical Imaging*, vol. 2006, Article ID 70839, 7 pages, 2006.

[10] X. Song, X. Xiong, and Z. Zhang, "A fast pre-iteration reconstruction method for 3D fluorescence tomography based on finite element analysis," in *The 5th Annual Meeting of the Society for Molecular Imaging*, The Big Island of Hawaii, Hawaii, USA, August-September 2006.

[11] A. Joshi, W. Bangerth, K. Hwang, J. C. Rasmussen, and E. M. Sevick-Muraca, "Fully adaptive FEM based fluorescence optical tomography from time-dependent measurements with area illumination and detection," *Medical Physics*, vol. 33, no. 5, pp. 1299–1310, 2006.

[12] A. B. Milstein, S. Oh, K. J. Webb, et al., "Fluorescence optical diffusion tomography," *Applied Optics*, vol. 42, no. 16, pp. 3081–3094, 2003.

[13] W. Cong, D. Kumar, Y. Liu, A. Cong, and G. Wang, "A practical method to determine the light source distribution in bioluminescent imaging," in *Developments in X-Ray Tomography IV*, vol. 5535 of *Proceedings of SPIE*, pp. 679–686, Denver, Colo, USA, October 2004.

[14] V. Ntziachristos and R. Weissleder, "Experimental three-dimensional fluorescence reconstruction of diffuse media by use of a normalized born approximation," *Optics Letters*, vol. 26, no. 12, pp. 893–895, 2001.

[15] E. U. Mumcuoglu, R. Leahy, S. R. Cherry, and Z. Zhou, "Fast gradient-based methods for Bayesian reconstruction of transmission and emission PET images," *IEEE Transactions on Medical Imaging*, vol. 13, no. 4, pp. 687–701, 1994.

[16] E. U. Mumcuoglu and R. Leahy, "A gradient projection conjugate gradient algorithm for Bayesian PET reconstruction," in *IEEE Nuclear Science Symposium and Medical Imaging Conference*, vol. 3, pp. 1212–1216, Norfolk, Va, USA, October-November 1994.

[17] J. A. Fessler and S. D. Booth, "Conjugate-gradient preconditioning methods for shift-variant PET image reconstruction," *IEEE Transactions on Image Processing*, vol. 8, no. 5, pp. 688–699, 1999.

[18] A. H. Hielscher, A. D. Klose, and K. M. Hanson, "Gradient-based iterative image reconstruction scheme for time-resolved optical tomography," *IEEE Transactions on Medical Imaging*, vol. 18, no. 3, pp. 262–271, 1999.

[19] J. Nocedal and S. J. Wright, *Numerical Optimization*, Springer, New York, NY, USA, 2000.

[20] A. J. Davies, D. B. Christianson, L. C. W. Dixon, R. Roy, and P. van der Zee, "Reverse differentiation and the inverse diffusion problem," *Advances in Engineering Software*, vol. 28, no. 4, pp. 217–221, 1997.

[21] M. J. D. Powell, "Restart procedures for the conjugate gradient method," *Mathematical Programming*, vol. 12, no. 1, pp. 241–254, 1977.

[22] M. Hanke, J. G. Nagy, and C. Vogel, "Quasi-Newton approach to nonnegative image restorations," *Linear Algebra and Its Applications*, vol. 316, no. 1–3, pp. 223–236, 2000.

Hindawi Publishing Corporation
International Journal of Biomedical Imaging
Volume 2007, Article ID 63234, 4 pages
doi:10.1155/2007/63234

*Research Article*

# Kidney Modelling for FDG Excretion with PET

**Huiting Qiao,[1] Jing Bai,[1] Yingmao Chen,[2] and Jiahe Tian[2]**

[1] *Department of Biomedical Engineering, Tsinghua University, Beijing 100084, China*
[2] *Department of Nuclear Medicine, General Hospital of PLA, Beijing 100853, China*

Received 18 January 2007; Accepted 31 May 2007

Recommended by Jie Tian

The purpose of this study was to detect the physiological process of FDG's filtration from blood to urine and to establish a mathematical model to describe the process. Dynamic positron emission tomography scan for FDG was performed on seven normal volunteers. The filtration process in kidney can be seen in the sequential images of each study. Variational distribution of FDG in kidney can be detected in dynamic data. According to the structure and function, kidney is divided into parenchyma and pelvis. A unidirectional three-compartment model is proposed to describe the renal function in FDG excretion. The time-activity curves that were picked up from the parenchyma, pelvis, and abdominal aorta were used to estimate the parameter of the model. The output of the model has fitted well with the original curve from dynamic data.



## 1. INTRODUCTION

The development of positron emission tomography (PET) has made it possible to detect the physiological process in a human body. [18F]fluoro-2-deoxy-D-glucose(FDG) is the analog of glucose, which is widely used in clinical PET experiment [1]. In order to understand the metabolism of glucose and to detect diseases better, mathematical models of FDG have been established for brain, heart, liver, and some other organs [2–5]. Although kidney is the most important organ in the metabolism system of a human, and large quantity of FDG in the body is accumulated in the urine through the kidney [6], yet little work has been done for kidney modelling with FDG PET. There are two major reasons why only a few mathematical models are established for kidney. The first reason is because of the complicated structure and function of the kidney [7], and the second reason is due to the high excretion of FDG through the kidney [6, 8]. FDG, unlike glucose, cannot be reabsorbed in the proximal tubules of the kidney, and so FDG will be accumulated in the urine.

To describe the filtration process of FDG from blood to urine, seven normal volunteers took part in the dynamic FDG-PET experiment. The imaging data has been used for kinetic analysis and parameter estimation.

Compared to the high concentration of FDG in kidney collection system, the small quantity of metabolized FDG in kidney can be neglected. The dynamic imaging shows the filtration of FDG and the process of urinary excretion. Though three-compartment four-rate model is widely used to describe the metabolism of some of the human organs, it is not suitable for describing kidney. A unidirectional compartment model is proposed to show the transport process of FDG from blood to urine. Due to the kidney which contains great quantity of blood vessel and collection system of urine, the effect fractions from the blood and the urine to parenchyma will be all considered in the model.

Bouchet et al. [7] had proposed the model which divides the kidney into five parts in order to compute the absorbed fractions of radiopharmaceuticals. In our study of dynamic PET imaging, the inhomogeneity of kidney can also be seen. Here, the kidney is separated into two parts: parenchyma and pelvis. Time-activity curves are picked up from each part and are used to estimate the parameters. Though there are great differences between each set of parameters, the output of the model is basically in accord with the original curve.

## 2. MATERIALS AND METHOD

### 2.1. Subjects

Seven normal volunteers participated in the study. The age of volunteers is between 34 to 60 years (mean ± SD, 47 ± 11 years), the height is from 165 to 185 cm (172 ± 7 cm), and the weight is from 53 to 94 kg (76 ± 12 kg). None of them has had a prior history of any major metabolic illnesses or renal diseases. Dynamic FDG-PET scans were performed on each

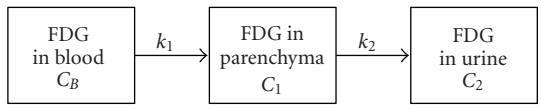


Figure 1: Model of kidney for FDG excretion.

volunteer. They were asked to fast for at least four hours and to empty the bladder before the scanning. During the experiment, they were asked to lie down still and to keep quiet. Each volunteer was informed fully about the purposes and procedures of the study and was asked to give a written consent.

### 2.2. PET scanning protocol

All the experiments were done with an ECAT EXACT HR$^+$ PET (CTI/Siemens, Inc., TN, USA). The scanner provides 63 continuous transaxial slices with a 15.5 cm field of view. The spatial resolution is 4.2 mm full width at half maximum in the centre field of view. The experiments were performed in a single bed position covering the kidneys. The tracer dose of FDG, 4-5 mCi, was injected intravenously into the human body, and PET scan began immediately after the injection. In the sampling protocol, the dynamic imaging sequences consisted of six 10-seconds frames; eight 20-seconds frames; six 30-seconds frames; five 60-seconds frames; four 300-seconds frames; and three 600-seconds frames, which is in total of 32 frames for a total scan time of 61 minutes and 40 seconds.

### 2.3. Organ time-activity measurement

Kidney and abdominal aorta can be detected from the dynamic PET image. During study, the time-activity curve was picked up from the drawn region of interest (ROI) in each frame. The radioactivity was calculated by averaging the whole voxel's values within the ROI. Kidney is different from other organs, because it is heterogeneous for the complex physiological function. Kidney is divided into two parts: renal parenchyma and pelvis. In this study, the ROIs of parenchyma and pelvis were drawn for each plan from the 3D image data in separate frames which have a best view of certain parts of the kidney. The ROI of parenchyma is drawn in the frame for about 2 minutes after the scan, and the ROI of pelvis is drawn in the frame for about 5 minutes. The blood time-activity curve (BTAC) was derived from the ROI in abdominal aorta [9], which is drawn in the frame for 1 minute.

### 2.4. Model analysis

A three-compartment model (Figure 1) with four parameters is proposed to simply describe the excretion of FDG. In this simple model, blood, renal parenchyma, and urine compartments are assumed to be uniformly distributed with FDG, respectively. The urine compartment includes urine in the pelvis and urine in the bladder. For the high excretion of FDG, the metabolism of FDG in kidney is unobvious and is neglected in the model. $k_1$ and $k_2$ are the rate constants of FDG between each compartment,

$$\frac{dC_1}{dt} = k_1 C_B - k_2 C_1, \tag{1}$$

$$C_1(t) = k_1 \cdot e^{-k_2 t} \otimes C_B(t), \tag{2}$$

$$C_T(t) = k_1 e^{-k_2 t} \otimes C_B(t) + f_1 C_B(t) + f_2 C_{\text{pelvis}}, \tag{3}$$

where $C_B$ is the concentration of FDG in blood, $C_1$ is the concentration of FDG in parenchyma, $C_2$ is the concentration of FDG in urine, $C_{\text{pelvis}}$ is the concentration of FDG in pelvis, and $C_T$ is the concentration of FDG detected from PET. Equation (1) shows the kinetic description of the compartment model, (2) is derived from (1), and (3) shows that the activity in kidney detected by PET is not only decided by $C_1$, but also affected by $C_B$ and $C_{\text{pelvis}}$. Kidney is an organ which is rich in blood. So, the parameter $f_1$ is used to describe the effect fraction from the blood to parenchyma. Parenchyma and pelvis are so close to each other inside the kidney that their effect on each other cannot be neglected. Thus, parameter $f_2$ is introduced to calibrate the effect of the urine from the pelvis.

## 3. RESULT

### 3.1. FDG imaging

In these seven subjects, the kidneys are clearly visualized with very high target-to-background ratio (Figure 2). Shreve et al. [10] had used carbon-11-acetate as the tracer to detect kidney. In their studies, no urinary tracer activity has appeared in the intrarenal collecting system. Unlike carbon-11-acetate and glucose, FDG is a kind of tracer which cannot be reabsorbed when the initial urine passes through the renal tubule. Thus, FDG can be detected in renal pelvis in some frames. The concentration distribution variation can be seen in kidney in different frames. Figures 3(a) and 3(b) are the same coronal sections of a dynamic PET study in one frame (in 1 minute after injection), but the two images are in different brightness (window center) and contrast (window wide). The part of the kidney in which activity is highly accumulated can be found by adjusting brightness and contrast (Figure 3(a)). Figure 2(b) gives the outline of the whole organ in hot color scheme, and two images, Figures 3(a) and 3(b) were fused. It can be seen from the fused image (Figure 3(c)) that in early time after the injection, the FDG is mostly accumulated in the edge of the kidney, where the renal cortex and some of renal medulla are located. Figure 3(d) is another fused image in frame for over 5 minutes after injection. It can be seen that the high activity concentration appears in the renal depression, where the position of renal pelvis is.

### 3.2. Kinetic parameter

Seven dynamic data sets from the seven subjects were used for parameter estimation. The BTAC which has been picked up from aorta and the tissue time-activity curve (TTAC) of pelvis is the input of the model, while the detected TTAC

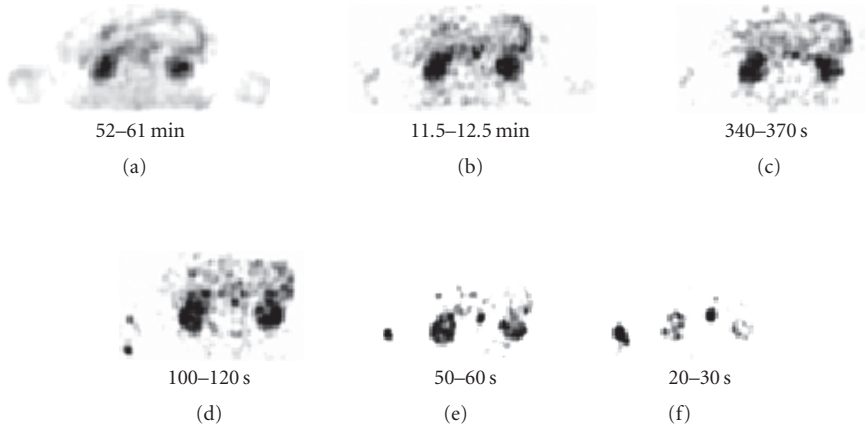


Figure 2: Some of the sequential transaxial images of one study.

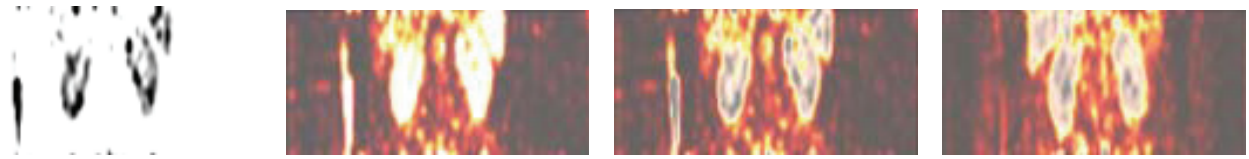


Figure 3: Images of kidney: (a)-(b) is one coronal section at 40–50 seconds, (c) is the fused image of (a) and (b), and (d) is another fused coronal section at 310–340 seconds.

Table 1: Parameters of the kidney model.

| | $k_1$ (min$^{-1}$) | $k_2$ (min$^{-1}$) | $f_1$ | $f_2$ |
|---|---|---|---|---|
| Subject1 | 3.4659 | 2.8042 | 0.15964 | 0.07574 |
| Subject2 | 1.8423 | 2.3827 | 0.03293 | 0.10977 |
| Subject3 | 1.3318 | 1.9806 | 0.19699 | 0.04073 |
| Subject4 | 0.7703 | 0.8280 | 0.17543 | 0.03623 |
| Subject5 | 1.5503 | 1.1120 | 0.10181 | 0.00000 |
| Subject6 | 0.8981 | 0.9486 | 0.07342 | 0.04563 |
| Subject7 | 1.2170 | 1.0007 | 0.03525 | 0.03525 |
| Average | 1.5822 | 1.5795 | 0.1269 | 0.0491 |
| SD | 0.9074 | 0.7981 | 0.0593 | 0.0347 |

of the parenchyma is the output of the model. Weighted least squares principle [11] was used to fit the simple kidney model. The weight is the inverses of the measurement error. Parameters for the model are listed in Table 1.

The average and standard deviations (SD) for $k_1$, $k_2$, $f_1$, and $f_2$ are also shown in Table 1. The average rate constant $k_1$ is 1.5822 min$^{-1}$, and $k_2$ is 1.5795 min$^{-1}$. The effect fraction $f_1$ is 0.1269, and $f_2$ is 0.0491. The parameters of each subject are compared with each other. Results show significant differences in the parameters for the subjects. Characters such as age, height, or weight of the individual subjects may be one of the reasons for the differences in the parameters. The confirmations of ROI for each study also lead to the huge differences especially for $f_2$, which describes the effect from urine

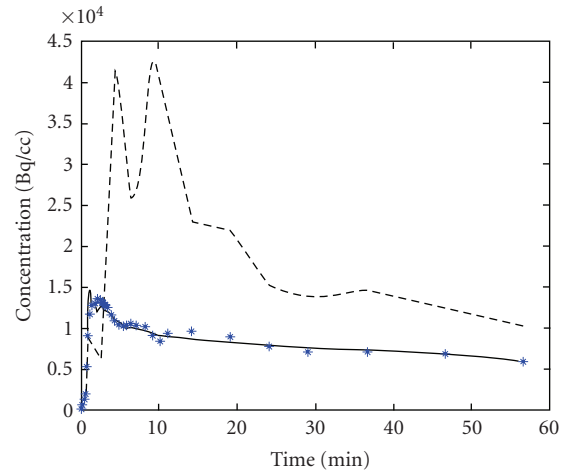


Figure 4: Time-activity curve. The normal line represents the time-activity curve of renal parenchyma, the dashed line is the time-activity curve of renal pelvis, and the asterisks show the point we fitted.

of pelvis to renal parenchyma. The further the ROI of the parenchyma is from the pelvis, the smaller $f_2$ will be. Figure 4 shows the time-activity curve of one of the experiments. The asterisk points are the result from compartment model and estimated parameters.

## 4. DISCUSSION

The research of metabolism with FDG PET has been done for many years, but only a little work is focused on kidney. In some study, the function of kidney is just described by a constant rate from plasma to urine [5]. For some tracer, kidney can also be described by the classical three-compartment model [12]. The kidney model for FDG is different, because F-18 FDG is excreted greatly into the tubular lumen and accumulated in the renal collecting system [8], no reabsorption appears. So we use only one-direction compartment model to describe kidney. Seven sets of dynamic clinical data were being used to estimate the parameters. Results have shown great differences in each subject. However, the output of the model fits well with the original curve from clinical data.

In order to make the model simple and workable, some assumptions were made in this study: the blood time-activity curve which was picked up from the aorta is used as plasma time-activity curve in parameter estimation; no urine is accumulated in the parenchyma, and the effect from the pelvis is assumed to be consistent.

The high excretion of FDG has made it difficult to analyze the glucose metabolism of kidney and also to detect renal diseases. However, the high excretion of FDG can still provide other important physiological information. In the dynamic data, Parenchyma and pelvis can be distinguished, and the time-activity curves are shown in Figure 4. The peaks of the two curves which show the highest concentration appear at different time points. The peak of the pelvis appears a little later than that of parenchyma. The result is in accord with the renal physiology. Two peaks are shown in the time-activity curve for pelvis. This can be explained by the physiology of pelvis. Pelvis is the tissue which accumulates urine temporarily. The urine is then transported to bladder. The time-activity curve of the pelvis shows the process of urinary transport to bladder. The process cannot just be described by a rate constant. Hence, this model is just a preliminary study of kidney, further investigation will be done.

## ACKNOWLEDGMENTS

This work is partially supported by the National Nature Science Foundation of China, the Tsinghua-Yue-Yuen Medical Science Foundation, the National Basic Research Program of China, and the Special Research Fund for the Doctoral Program of Higher Education of China. The authors would like to thank Professor Dagan Feng, Professor Eberl Stefan, and Dr. Lingfeng Wen for their valuable comments at School of Information Technologies, the University of Sydney.

## REFERENCES

[1] B. M. Gallagher, A. Ansari, H. Atkins, et al., "Radiopharmaceuticals XXVII. 18F-labeled 2-deoxy-2-fluoro-d-glucose as a radiopharmaceutical for measuring regional myocardial glucose metabolism in vivo: tissue distribution and imaging studies in animals," *Journal of Nuclear Medicine*, vol. 18, no. 10, pp. 990–996, 1977.

[2] S. C. Huang, M. E. Phelps, E. J. Hoffman, K. Sideris, C. J. Selin, and D. E. Kuhl, "Noninvasive determination of local cerebral metabolic rate of glucose in man," *The American Journal of Physiology*, vol. 238, no. 1, pp. E69–E82, 1980.

[3] T. Torizuka, K. R. Zasadny, B. Recker, and R. L. Wahl, "Untreated primary lung and breast cancers: correlation between F-18 FDG kinetic rate constants and findings of in vitro studies," *Radiology*, vol. 207, no. 3, pp. 767–774, 1998.

[4] T. Torizuka, S. Nobezawa, S. Momiki, et al., "Short dynamic FDG-PET imaging protocol for patients with lung cancer," *European Journal of Nuclear Medicine*, vol. 27, no. 10, pp. 1538–1542, 2000.

[5] M. T. Hays and G. M. Segall, "A mathematical model for the distribution of fluorodeoxyglucose in humans," *Journal of Nuclear Medicine*, vol. 40, no. 8, pp. 1358–1366, 1999.

[6] J. K. Moran, H. B. Lee, and M. D. Blaufox, "Optimization of urinary FDG excretion during PET imaging," *Journal of Nuclear Medicine*, vol. 40, no. 8, pp. 1352–1357, 1999.

[7] L. G. Bouchet, W. E. Bolch, H. P. Blanco, et al., "MIRD Pamphlet No. 19: absorbed fractions and radionuclide S values for six age-dependent multiregion models of the kidney," *Journal of Nuclear Medicine*, vol. 44, no. 7, pp. 1113–1147, 2003.

[8] Z. Szabo, J. Xia, W. B. Mathews, and P. R. Brown, "Future direction of renal positron emission tomography," *Seminars in Nuclear Medicine*, vol. 36, no. 1, pp. 36–50, 2006.

[9] G. Germano, B. C. Chen, S.-C. Huang, S. S. Gambhir, E. J. Hoffman, and M. E. Phelps, "Use of the abdominal aorta for arterial input function determination in hepatic and renal PET studies," *Journal of Nuclear Medicine*, vol. 33, no. 4, pp. 613–620, 1992.

[10] P. Shreve, P.-C. Chiao, H. D. Humes, M. Schwaiger, and M. D. Gross, "Carbon-11-acetate PET imaging in renal disease," *Journal of Nuclear Medicine*, vol. 36, no. 9, pp. 1595–1601, 1995.

[11] A. Bertoldo, P. Vicini, G. Sambuceti, A. A. Lammertsma, O. Parodi, and C. Cobelli, "Evaluation of compartmental and spectral analysis models of [$^{18}$F]FDG kinetics for heart and brain studies with PET," *IEEE Transactions on Biomedical Engineering*, vol. 45, no. 12, pp. 1429–1448, 1998.

[12] J. S. Fowler, J. Logan, G.-J. Wang, et al., "PET imaging of monoamine oxidase B in peripheral organs in humans," *Journal of Nuclear Medicine*, vol. 43, no. 10, pp. 1331–1338, 2002.

Hindawi Publishing Corporation
International Journal of Biomedical Imaging
Volume 2007, Article ID 86741, 4 pages
doi:10.1155/2007/86741

*Research Article*

# Experimental Study on Bioluminescence Tomography with Multimodality Fusion

**Yujie Lv,[1] Jie Tian,[1,2] Wenxiang Cong,[3] and Ge Wang[3]**

[1] *Medical Image Processing Group, Institute of Automation, Chinese Academy of Sciences, P.O. Box 2728, Beijing 100080, China*
[2] *Life Science Center, Xidian University, Xian 710071, Shaanxi, China*
[3] *Division of Biomedical Imaging, VT-WFU School of Biomedical Engineering and Sciences, Virginia Polytechnic Institute and State University, Blacksburg, VA 24061, USA*

Received 12 March 2007; Accepted 1 August 2007

Recommended by Ming Jiang

To verify the influence of a priori information on the nonuniqueness problem of bioluminescence tomography (BLT), the multimodality imaging fusion based BLT experiment is performed by multiview noncontact detection mode, which incorporates the anatomical information obtained by the microCT scanner and the background optical properties based on diffuse reflectance measurements. In the reconstruction procedure, the utilization of adaptive finite element methods (FEMs) and a priori permissible source region refines the reconstructed results and improves numerical robustness and efficiency. The comparison between the absence and employment of a priori information shows that multimodality imaging fusion is essential to quantitative BLT reconstruction.



Bioluminescence tomography (BLT) has an increasingly significant effect on revealing the molecular and cellular information in vivo [1]. When the bioluminescence imaging experiment is performed, luciferase can be introduced into various types of cells, organisms, and genes in a living mouse. Then, luciferin is combined with luciferase in the presence of oxygen and ATP to generate bioluminescent signals of about 600 nm in wavelength. The mechanism of BLT is to identify bioluminescent source from the light flux detected on the surface of small animal. However, three-dimensional bioluminescent source reconstruction is an inverse source problem in theory, which has been less researched and is different from the inverse scattering imaging, such as diffusion optical tomography (DOT). Then, in the highly heterogeneous biological tissues, the scattering and absorption of the photons emitted by bioluminescent source further increase the difficulty of source localization. In addition, although the absence of external illumination sources acquires high-sensitive signal and yields high-contrast image in bioluminescence imaging, it complicates the tomographic problem. Therefore, the unique and quantitative reconstruction of bioluminescent source is a topic of further investigation [2].

Based on diffusion approximation theory, the uniqueness theorem indicates that it is necessary to utilize a priori information to solve the nonunique problem of BLT [3]. In view of the spectral characteristics of the underlying bioluminescent source, hyper- and multispectral BLT methods are proposed [4–7]. Taking into account the surface light power distribution and the heterogeneous structure of the phantom, a priori permissible source region based BLT reconstruction method is developed on the fixed discretized mesh [8]. Then, the multilevel adaptive finite element based tomographic algorithm is also developed, which further reduces the ill-posedness of BLT and improves the reconstruction quality [9]. In this research, a BLT experiment is performed, which incorporates the anatomical and background optical information. Using our proposed tomographic algorithm [9], the reconstructed results show that multimodality imaging fusion is indispensable to quantitative BLT reconstruction.

Figure 1(a) shows the BLT prototype for bioluminescence imaging. The main component of the equipment is a cooled CCD camera (Princeton Instruments, USA), which collects optical signals emitted from bioluminescent source in the phantom. The combination of the vertically rotated stage under computer control and the camera realizes the multiview noncontact detection. When the phantom is placed on the stage, we may manually adjust the distance

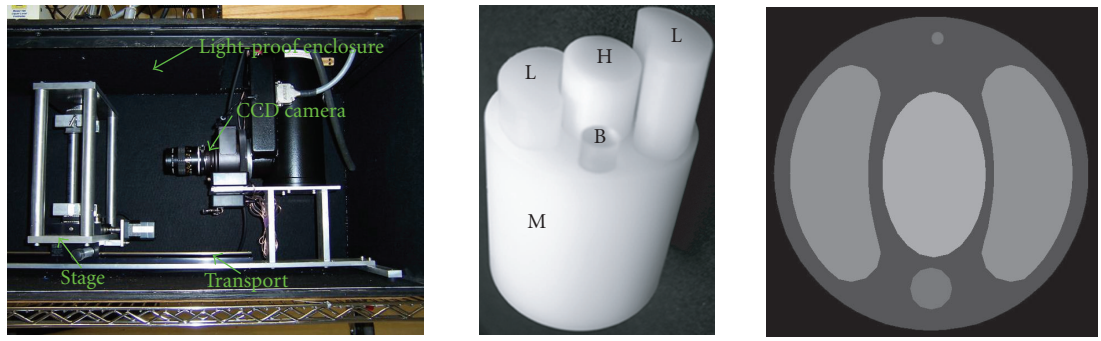


(a) (b) (c)

Figure 1: BLT system and physical phantom. (a) Multiview noncontact BLT prototype; (b) the physical heterogeneous phantom consisting of bone (B), heart (H), lungs (L), and muscle (M); and (c) a slice scanned by microCT scanner.

between the lens and the phantom surface through the controlled transport for the best signal acquisition. In addition, the utilization of light-tight enclosure guarantees that the bioluminescence imaging is performed in a totally dark environment.

When bioluminescent photons propagate in biological tissue, the radiative transfer equation (RTE) may precisely describe photon transportation. Diffusion equation as an approximation has been extensively applied in terms of high scattering characteristic of tissues [8]. In addition, Robin boundary condition is used to deal with the refractive indices mismatch between the small animal and the external medium [8]. In the framework of adaptive finite element analysis, a linear relationship between the measurable boundary flux $\Phi_k^m$ and the unknown source density $S_k^p$ can be established on the $k$th discretized level in terms of a priori permissible source region [9]:

$$A_k S_k^p = \Phi_k^m. \tag{1}$$

Then, we define the following $k$th level minimization problem to reconstruct source distribution based on Tikhonov regularization methods:

$$\min_{S_{\inf}^k \le S_k^p \le S_{\sup}^k} \Theta_k(S_k^p) = \{||A_k S_k^p - \Phi_k^m||_\Lambda + \lambda_k \eta_k(S_k^p)\}, \tag{2}$$

where $S_{\inf}^k$ and $S_{\sup}^k$ are the $k$th level lower and upper bounds of source density; $\Lambda$ is the weight matrix, $\|V\|_\Lambda = V^T \Lambda V$; $\lambda_k$ the regularization parameter; and $\eta_k(\cdot)$ the penalty function. Through selecting the effective optimization method, we can obtain the preferable BLT reconstruction.

In this bioluminescence imaging experiment, a heterogeneous physical phantom of 30 mm height and 15 mm radius is designed and fabricated. The phantom, shown in Figure 1(b), is made up of four different materials, that is, high-density polyethylene (8624K16), nylon 6/6 (8538K23), delrin (8579K21), and polypropylene (8658K11) to represent muscle, lungs, heart, and bone, respectively. Two luminescent sources of about 1.9 mm height and 0.56 mm diameter are embedded in the left-lung region of the phantom with the centers at (−9.0, 1.5, 0.0) and (−9.0, −1.5, 0.0). Their source densities are 155.53 nW/mm$^3$ and 178.49 nW/mm$^3$, respectively. The slice of the phantom representing anatomical information is obtained by microCT scanner for generating the volumetric finite element mesh, as shown in Figure 1(c). In addition, the optical properties of four materials as a priori information need to be acquired. To each material, a cylindrical phantom with 10 mm radius and 20 mm height was made. The side surface of the phantom was blackened. After the stable light was obtained by an integrating sphere, it was guided for illumination through the optic fiber. The optic fiber was inserted into a small hole of 10 mm depth at the center of the phantom bottom surface. The CCD camera was used to detect the output photon density on the other bottom surface of the phantom. After the data acquisition, an optical tomography procedure was used to decide the optical parameters of each material. Specifically, the specimen was considered as a semi-infinite homogeneous medium, and diffusion theory was applied with the extrapolated boundary condition. The photon density on the bottom surface was predicted by an analytic formula; and then, the absorption and reduced scattering coefficients were calculated by a nonlinear least-square fitting, as shown in Table 1. The detailed information can be found in [8]. In the noncontact detection mode, multiview detection is essential to reduce the influence of the curved surface of the phantom on the measured value. In this experiment, four views are acquired, which are separated by 90 degrees along radial directions. Its schematic diagram is displayed in Figure 2. Measured data on the CCD camera is transformed from the recorded pixel gray levels by $\phi = \text{pix} \times 0.377\ \text{pW/mm}^2$ [8], where $\phi$ is the photon density and pix denotes the pixel value.

Table 1: Optical properties of the physical heterogeneous phantom.

| Material | Muscle | Lung | Heart | Bone |
|---|---|---|---|---|
| $\mu_a$[mm$^{-1}$] | 0.007 | 0.023 | 0.011 | 0.001 |
| $\mu_s'$[mm$^{-1}$] | 1.031 | 2.000 | 1.096 | 0.060 |

When the BLT reconstruction is performed, the physical phantom is an anatomical and optical homogeneous object if two types of a priori information are not considered.

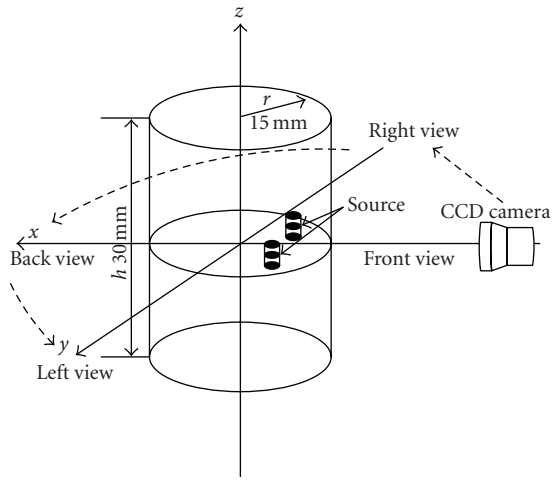


Figure 2: Schematic diagram of the multipleview bioluminescence imaging experiment.

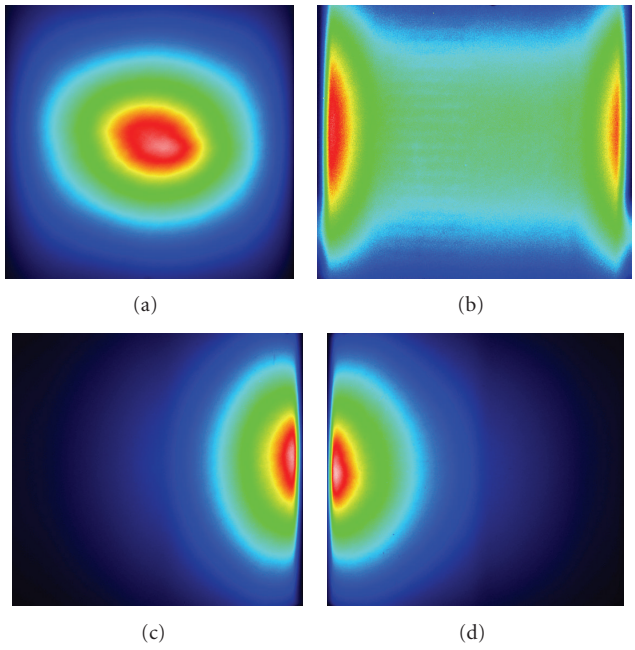


Figure 3: The detected photon energy distribution on the phantom surface by CCD camera.

Area-weighted method is employed to approximate the homogeneous optical property. Through the difference of detected surface light power distribution in four views, as demonstrated in Figure 3 [8], we may infer the permissible source region as $P_s = \{(x, y, z) \mid x < 0, -1.5 < z < 1.5, (x, y, z) \in \text{the phantom}\}$, as shown in Figure 4(a). During the reconstruction procedure, a modified Newton method with active-set strategy is employed for the minimization problem $\Theta_k(S_k^p)$ at each level. Using a posteriori error estimation techniques, the elements with higher errors and reconstructed values in the forbidden and permissible source regions, respectively, are selected for adaptive mesh refinement after the reconstruction is accomplished on

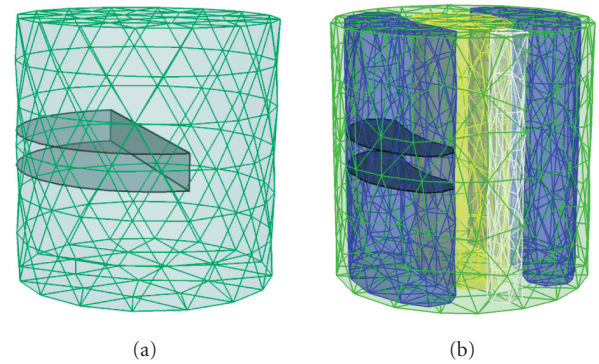


Figure 4: The initial homogeneous (a) and heterogeneous (b) finite element meshes used in the BLT reconstruction. The black areas represent a priori permissible source regions.

Table 2: Quantitative comparison between the reconstructed and actual sources with and without a priori anatomical and optical information. Density errors are calculated by $|S_{\text{recons}} - S_{\text{real}}|/S_{\text{real}}$.

| No. | Recons. pos. (mm) | Recons. dens. (nW/mm$^3$) | Pos./dens. errors |
|---|---|---|---|
| 1 | (−6.39,0.39,1.31) | 168.80 | N.A. |
| 2 | (−5.83,2.85,−0.09) | 143.69 | 3.45/7.61 |
| | (−6.05,-1.31,0.10) | 177.26 | 2.96/0.69 |
| 3 | (−9.40,1.31,−0.26) | 167.49 | 0.51/7.69 |
| | (−8.11,−1.76,0.24) | 175.74 | 0.96/1.54 |

the coarse mesh. *Red-green* refinement strategy reasonably implements the local mesh refinement. Note that BLT with a coarsely discretized mesh means less unknown variables, higher computational efficiency, and better numerical stability than that with a finely discretized counterpart. Hence, the optimization of the objective function $\Theta_k(S_k^p)$ is indispensable on the coarse mesh. The detailed explanation and discussion can be found elsewhere [9]. After four mesh refinements, Figure 5(a) shows the final reconstructed results. Due to the absence of anatomical and optical information, the BLT reconstruction cannot distinguish two light sources, and the reconstructed position is also far from the actual one despite that the roughly inferred permissible source region is utilized. When the anatomical information is considered, the selection of permissible source region may be restricted in the left lung, as illustrated in Figure 4(b). Two light sources can be distinguished from the reconstructed results, as shown in Figure 5(b). Although there are small relative errors in source density between the reconstructed and actual sources, the preferable source localization cannot be obtained. Finally, Figure 5(c) displays the reconstructed results in terms of the utilization of anatomical and optical information. The position and density of light sources are better reconstructed. The quantitative comparison above is summarized in Table 2, which further demonstrates the importance of anatomical and optical information for BLT reconstruction.

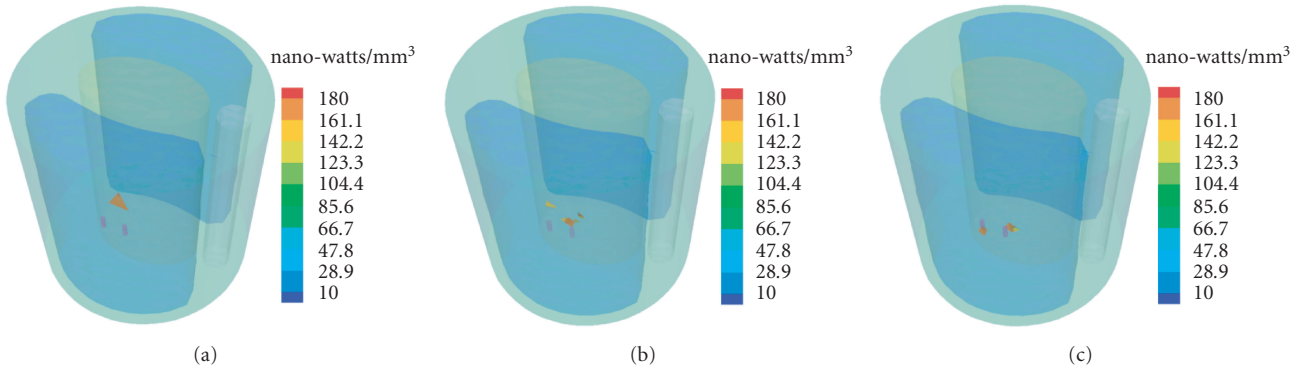


Figure 5: Comparison between the actual and reconstructed sources. (a) The BLT reconstruction without anatomical and optical information; (b) the counterpart only with anatomical information; and (c) that with anatomical and optical information.

In this research, to our knowledge, we have first presented that multimodality imaging fusion is essential for quantitative BLT reconstruction through the experimental comparison based on the multilevel adaptive finite element algorithm. Despite that there is a linear relationship between the boundary measured data and the unknown source variables, inherent characteristics make BLT reconstruction more ill-posed compared with fluorescence imaging. The more a priori knowledge we have, the better the light source is reconstructed [3]. The utilization of anatomical and optical information not only approaches the basal optical transportation model better, but also helps to infer the permissible source region. When the small animal-based BLT equipment and algorithm researches are ongoing for the practical application to biology, this research provides the basically experimental verification for BLT reconstruction.

## ACKNOWLEDGMENTS

This work is supported by NIH/NIBIB, Grant EB001685, NBRPC (2006CB705700), NSFDYS (60225008), and NSFC (30370418, 30500131, and 60532050), China.

## REFERENCES

[1] T. F. Massoud and S. S. Gambhir, "Molecular imaging in living subjects: seeing fundamental biological processes in a new light," *Genes and Development*, vol. 17, no. 5, pp. 545–580, 2003.

[2] V. Ntziachristos, J. Ripoll, L. V. Wang, and R. Weissleder, "Looking and listening to light: the evolution of whole-body photonic imaging," *Nature Biotechnology*, vol. 23, no. 3, pp. 313–320, 2005.

[3] G. Wang, Y. Li, and M. Jiang, "Uniqueness theorems in bioluminescence tomography," *Medical Physics*, vol. 31, no. 8, pp. 2289–2299, 2004.

[4] A. J. Chaudhari, F. Darvas, J. R. Bading, et al., "Hyperspectral and multispectral bioluminescence optical tomography for small animal imaging," *Physics in Medicine and Biology*, vol. 50, no. 23, pp. 5421–5441, 2005.

[5] G. Alexandrakis, F. R. Rannou, and A. F. Chatziioannou, "Tomographic bioluminescence imaging by use of a combined optical-PET (OPET) system: a computer simulation feasibility study," *Physics in Medicine and Biology*, vol. 50, no. 17, pp. 4225–4241, 2005.

[6] A. X. Cong and G. Wang, "Multispectral bioluminescence tomography: methodology and simulation," *International Journal of Biomedical Imaging*, vol. 2006, Article ID 57614, 7 pages, 2006.

[7] H. Dehghani, S. C. Davis, S. Jiang, B. W. Pogue, K. D. Paulsen, and M. S. Patterson, "Spectrally resolved bioluminescence optical tomography," *Optics Letters*, vol. 31, no. 3, pp. 365–367, 2006.

[8] W. Cong, G. Wang, D. Kumar, et al., "Practical reconstruction method for bioluminescence tomography," *Optics Express*, vol. 13, no. 18, pp. 6756–6771, 2005.

[9] Y. Lv, J. Tian, W. Cong, et al., "A multilevel adaptive finite element algorithm for bioluminescence tomography," *Optics Express*, vol. 14, no. 18, pp. 8211–8223, 2006.

Hindawi Publishing Corporation
International Journal of Biomedical Imaging
Volume 2007, Article ID 28387, 9 pages
doi:10.1155/2007/28387

*Research Article*

# A Near-Infrared Optical Tomography System Based on Photomultiplier Tube

**Huacheng Feng, Jing Bai, Xiaolei Song, Gang Hu, and Junjie Yao**

*Department of Biomedical Engineering, Tsinghua University, Beijing 100084, China*

Received 5 January 2007; Revised 7 May 2007; Accepted 7 June 2007

Recommended by Jie Tian

Diffuse optical tomography (DOT) is a rapidly growing discipline in recent years. It plays an important role in many fields, such as detecting breast cancer and monitoring the cerebra oxygenation. In this paper, a relatively simple, inexpensive, and conveniently used DOT system is presented in detail, in which only one photomultiplier tube is employed as the detector and an optical multiplexer is used to alter the detector channels. The 32-channel imager is consisted of 16-launch fibers and 16-detector fibers bundles, which works in the near-infrared (NIR) spectral range under continuous-wave (CW) model. The entire imaging system can work highly automatically and harmoniously. Experiments based on the proposed imaging system were performed, and the desired results can be obtained. The experimental results suggested that the proposed imaging instrumentation is effective.



## 1. INTRODUCTION

Optical imaging is a traditional imaging technique for medical purpose [1]. However, diffuse optical tomography (DOT) is a relatively new discipline and drew increasing interest in recent years [2, 3]. If the target-specific fluorescent contrast agent is employed in DOT, it can probe molecular event in vivo [4–6], which is very useful to detect disease in its early stage, comprehensively understand disease mechanism, and develop new drugs. DOT has many advantages over the conventional imaging techniques. For example, it is not harmful to tissue due to its noninvasive and nonionizing characteristics. Thus it can be repeatedly even continuously used on patients at the bedside. In addition, DOT instrumentation is relatively inexpensive and can be made portable. DOT technique has shown its powerful potential in clinical applications. Currently, its two main applications are monitoring cerebral blood volume and oxygenation and screening breast cancer [7–12].

For neonates, the deficiencies of cerebral blood flow or oxygen may lead to severe irreversible damages to the brain development. The premature babies are more subject to have the risk of cerebral hemorrhage [10]. However, the existing conventional medical imaging modalities are not capable of monitoring the cerebral blood volume and oxygenation continuously without invasion and damage.

Besides, currently the most commonly used conventional means to detect breast tumor is X-ray. It is not suitable to be used on patients continuously or even frequently due to its radiative nature. In addition, when the tumor can be "seen" by the X-ray instrumentation, it is generally too late to be treated.

The optical tomography is a very powerful complementary tool to the existing conventional imaging techniques in the above mentioned fields [13].

Many investigators have contributed considerably to DOT technique, and many excellent DOT systems for medical purpose have been developed [1, 14, 15].

In this paper, we present a DOT imaging system that is based on photomultiplier tube (PMT). In the entire imaging system, only one PMT was employed as the detector and an optical multiplexer was used to alter the detector channels, so that the entire imaging system is relatively compact. Compared to the charge-coupled-device- (CCD-) based imaging system, it is relatively simple and considerably inexpensive. Besides, the proposed imaging instrumentation was designed as a highly automatically system, of which all the components can work harmoniously. In the following discussions, the system principle, including hardware setup and control and data acquisition software, is depicted in detail. Some experiments based on the proposed imaging system were

performed to test it. The experimental results demonstrate that the proposed imaging instrumentation is effective.

## 2. THEORETICAL BACKGROUND

The DOT imaging systems can be broadly divided into three categories [2]: continue-wave (CW) system, time-domain (TD) instrumentation, and frequency-domain (FD) modality. Each category has its advantages and disadvantages. In this paper, a CW system is represented in detail, in which the source light is sinusoidally modulated at the frequency of 5 kHz to facilitate the signal processing, such as elimination of noise.

As photons propagate in tissue, they experience scattering as well as absorption. In the near-infrared (NIR) spectral range, scattering is the dominant interaction. The transport process of photons in tissue can be well described by the radiation transport equation (RTE). Under certain assumptions, the RTE can be approximated by the diffusion equation (DE), a partial differential equation [3, 13, 16], which is more commonly used to model light transport in tissue. The diffusion equation in time-domain and frequency-domain has been derived in detail in earlier literature [13]. In the CW case, the DE can be written as

$$-\nabla\left(D(\mathbf{r})\nabla\Phi(\mathbf{r})\right)+\mu_a(\mathbf{r})\Phi(\mathbf{r})=q(\mathbf{r}), \tag{1}$$

where $\mathbf{r}$ is the location in tissue domain $\Omega$, $\Phi(\mathbf{r})$ is the photon density distribution, $\mu_a(\mathbf{r})$ is the absorption coefficient distribution, $q(\mathbf{r})$ is the source term, $D$ is the diffusion coefficient given by $D = 1/[3(\mu_a+\mu_s')]$, where $\mu_s' = (1-g)\mu_s$ is the reduced scattering coefficient, $\mu_s$ is the scattering coefficient, and $g$ is the anisotropic factor. The spatially dependent diffusion coefficient $D(\mathbf{r})$ and absorption coefficient $\mu_a(\mathbf{r})$ are the two main optical properties that reflect the function of the diseased and healthy tissues, and generally are the objectives to be reconstructed in DOT.

If the source $q(\mathbf{r})$ is a collimated incident beam, it can be treated as a "point source" under the surface $\partial\Omega$ at a depth of one mean free length [17]. In this situation, $q(\mathbf{r}) = q_0\delta(\mathbf{r}-\mathbf{r}_s)$, where $\mathbf{r}_s$ is the location of the equivalent point source and $q_0$ is the strength of the source term.

The Robin boundary condition in the steady-state case is usually employed [18]. So the measured quantity on the boundary is expressed as

$$\Gamma(\xi) = -D(\xi)\frac{\partial\Phi(\xi)}{\partial\mathbf{n}}, \tag{2}$$

where $\mathbf{n}$ is the outward normal at the site $\xi$ on the boundary $\partial\Omega$, and $\Gamma(\xi)$ is the measurement photon flux. In the CW case, along with the boundary condition (2), (1) is the most commonly used forward model for DOT and it is also employed in this paper in succeeding discussions.

In CW case, the absorption and diffusion coefficients cannot be recovered simultaneously [19, 20]. When scattering is the dominant interaction, it is absorption coefficient rather than scattering coefficient that often derives the important physiological information [1]. So the spatially dependent absorption coefficient distribution is the main optical property of tissue to be recovered.

The light in the NIR region of 650 nm–900 nm is most commonly used in practical applications [21]. In this spectral range, the principal absorbers, water, lipids, and hemoglobin have their lowest absorption coefficients, and then the penetration depth of the light in tissue is highest [7].

## 3. MATERIALS AND METHODS

### 3.1. System hardware setup

The proposed imaging instrumentation is primarily consisted of optical components, electrical components, control and data acquisition routines, and image reconstruction program. In this section, we present the scheme of the imaging system and its hardware setup.

The scheme of the DOT system can be illuminated in Figure 1.

The signal generator circuit (1) (homemade) generates a sinusoidal signal at the frequency of 5 kHz, which is used to modulate the intensity of the source light. The laser source (2) (VA671-200, Viasho, China) produces the source light at wavelength of 671 nm with maximum power of 200 mW. The output power of the source light can be adjusted to the desired level by adjusting the current of the laser generator. The purpose to modulate the source light is to facilitate the elimination of noise in succeeding signal processing. The sinusoidally intensity-modulated source light is also named as "AC light" (similarly, the constant intensity light is named as "DC light"), which is guided into a 1×16 fiber switch (3) (SUN-FSW 1 × 16 MM, SUN, China) through a source fiber. The AC light is then switched into one of the 16 launch fibers sequentially. The launch fibers are held in the imaging tube (4) (homemade), and launch the source light onto the tissue surface at different site sequentially. The imaging tube is illustrated in detail in Figure 2.

As illustrated in Figure 2, the imaging tube has five rings of bores. On each ring there are 32 bores, of which 16 bores are used to hold the launch fibers and the other 16 bores are for detector fibers bundles. They are separated uniformly. When the launch fibers and the detector fibers bundles are held on the same ring, they are generally used to image in two dimensions (2D). When held in different rings, they are used to image in three dimensions (3D).

The photons that are launched into the tissue undergo scattering and absorption. Some will "quench" when they are absorbed by tissue. The others will "escape" out of the tissue surface after they experience multiplying scattering.

The light that transilluminates from tissue is collected by the 16 detector fibers bundles, and then is guided into the optical multiplexer (5), which switches the 16 detector fibers bundles sequentially to the output fibers bundle. The optical multiplexer is homemade, and its principle is similar to the fiber switch (3). The 16 detector fibers bundles have large inner diameter of 1 mm, so that they can collect photons efficiently. However, they are not suitable to be coupled into the fiber switch, because for fiber switch the inner diameter of the coupled fiber is generally required at the $\mu$m level, such as 62.5 $\mu$m, a very widely used standard of fiber diameter. That is the reason why we used an optical multiplexer rather than

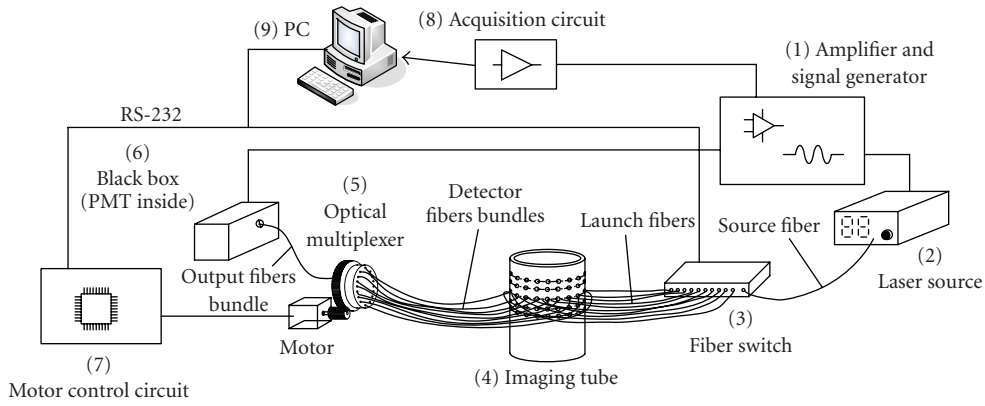


Figure 1: System scheme.

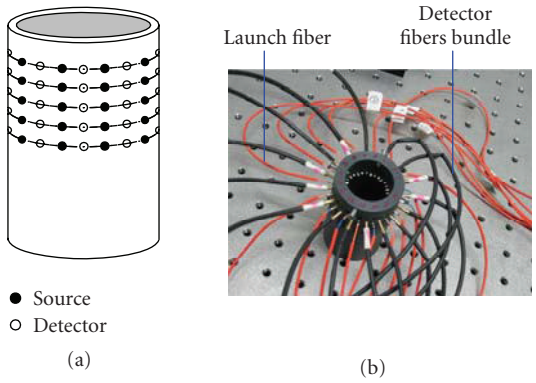


Figure 2: Imaging tube.

a fiber switch to alter the detector channels. The principle of the optical multiplexer is illustrated in Figure 3.

As illustrated in Figure 3, the optical multiplexer has mainly three parts: the motor (ii), the rotation part (iii), and the fixing part (iv). The rotation part and the fixing part are on-axis and coupled through an axletree. The fixing part has 32 bores and in which 16 bores are used to hold the detector fibers bundles (v). The rotation part has one bore that is used to hold the output fibers bundle (i). Driven by the motor, the rotation part can revolve around its axis while the fixing part is fixedly mounted on the platform. When the rotation part rotates to different location, the output fibers bundle will aim at different detector fibers bundles, and then the collected photons can be switched from one of the detector fibers bundles to the output fibers bundle. The inner diameter of the detector fibers bundles is 1 mm and that of the output fibers bundle is 2 mm. So the energy of the light can be guided efficiently into the black box (6) (homemade), as illustrated in Figure 1. Inside the black box there is a photomultiplier tube (PMT: R928, Hamamatsu, Japan), which translates the light to electrical signal. After being amplified and preprocessed, the electrical signal is then sampled into a personal computer (9) by the data acquisition circuit (8) (NI5112, Ni America, Tex, USA) as the raw data to be used to reconstruct the image.

The photos of the practical imaging system are shown in Figure 4.

### 3.2. *Instrumentation control and data acquisition software*

The primary duties of the instrumentation control and data acquisition software are to sample the raw data, postprocess the data, and control the hardware (fiber switch and the motor of the optical multiplexer). All these functions are integrated together for highly automatical purpose.

The control software is developed by C++ computer language and runs under Windows XP. The process of control and data acquisition can be described as follows: the personal computer delivers a command to the fiber switch by RS-232 serial interface to alter its channels (namely source channels) sequentially, and then the source light is switched into different launch fiber to illuminate different site on the tissue surface. Once the source channel is changed, the computer then delivers a commands to the motor control circuit (7) (as illustrated in Figure 1) to drive the motor, and then drive the rotation part of the optical multiplexer revolved to alter the detector channels. Thus the 16 detector fibers bundles are switched sequentially into the output fibers bundle, and then the light is guided into the black box to illuminate the PMT. The signal translated by PMT is a modulated signal, which is contaminated by the noise, such as the environmental light and the dark current of the PMT. We have two methods to improve the signal quality. One method is that the lock-in amplifier is employed, in which the sinusoidal signal produced by the signal generator is employed as the reference signal, and the amplified signal derived from the PMT as the input signal. Another method is that the digital filter is employed in the signal postprocessing routine in the computer. When the digital filter is used, as the signal is modulated at the frequency of 5 kHz, we employ one digital band-pass filter with the central frequency of 5 kHz to eliminate the noise. Through the digital filter, a relatively "pure" sinusoidal signal

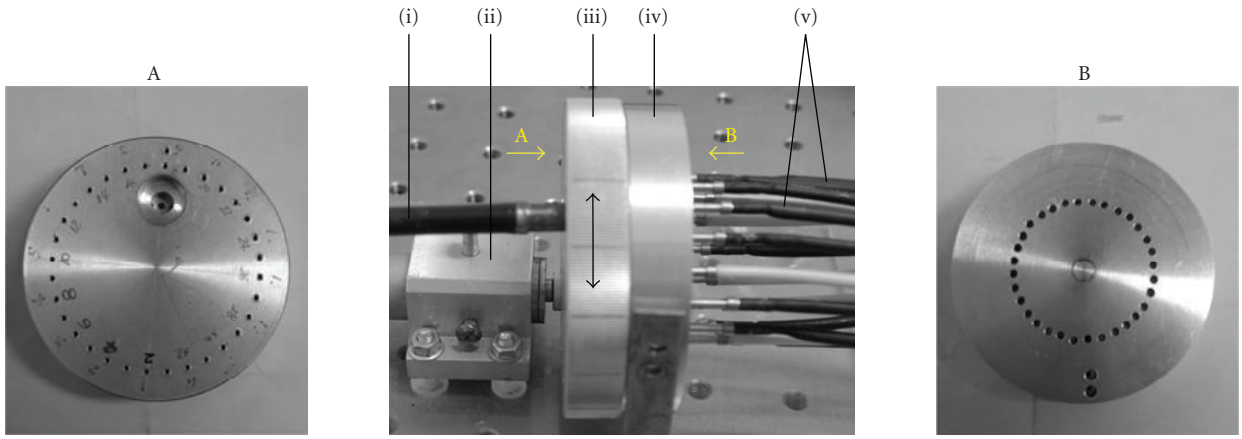


(a) Rotation part (iii) (b) Optical multiplixer (c) Fixing part (iv)

Figure 3: Optical multiplexer. For details, see the text.

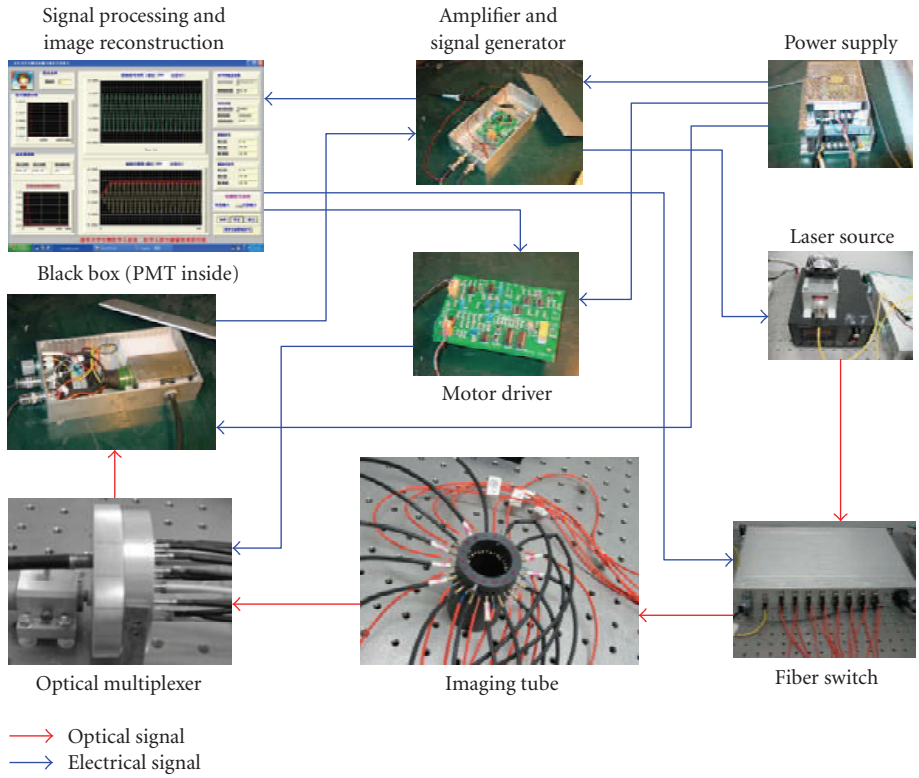


Figure 4: The practical imaging system.

can be obtained, and by Hilbert transform, the amplitude, that is, the envelope of the modulated signal, can be extracted (the result of the Hilbert transform of the sinusoidal signal is shown in Figure 6(a)). The arithmetical average of the amplitude is evalued as the raw data to reconstruct the image. Repeat above processes until all source channels and all detector channels have a turn. All the processes are implemented harmoniously and automatically through the instrumentation control and data acquisition software.

The flow chart of above processes and the corresponding signal format of each stage can be illustrated in Figure 5.

The graphic user interface (GUI) of the data acquisition and signal processing software is shown in Figure 6. The data acquisition, signal spectrum analysis, and signal processing windows are shown in Figure 6(a), in which the parameters of the digital band-pass filter, such as the cut-off frequency and the order of the filter can be set manually according to the result of the signal spectrum analysis.

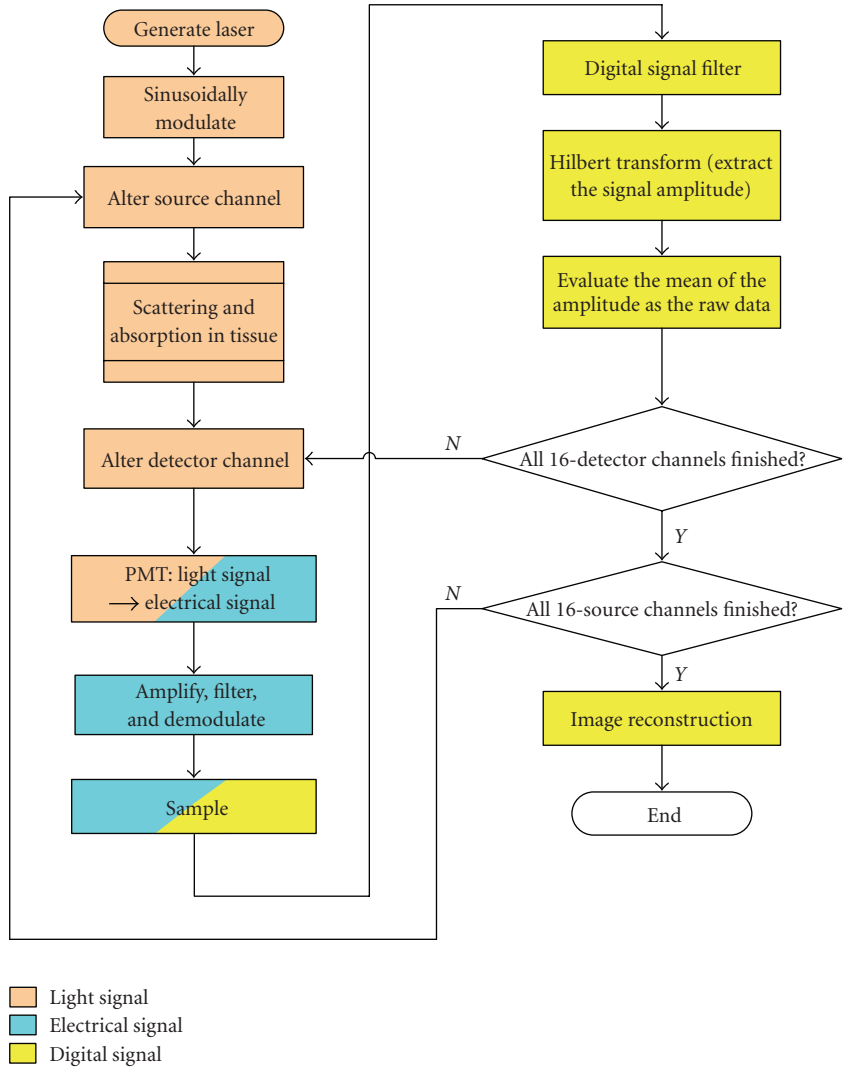


Figure 5: Flow chart of data acquisition and control processes.

The source-detector pair value display panel is shown in Figure 6(b), in which the 16 sources and 16 detectors constitute 256 source-detector pairs and they are divided into four pages. The active channel displays the value of current source-detector pair.

### 3.3. *Image reconstruction algorithm*

In this work, a gradient-based optimization inversion method is used for the absorption coefficient inversion with finite element method solving the forward model [17, 22]. Considering an experimental setting that includes $S$ point excitation light sources located at $\xi_j \in \partial\Omega$ $(j = 1, \ldots, S)$, and $M_j$ measurement positions $\varsigma_{j,i} \in \partial\Omega$ $(i = 1, \ldots, M_j)$ for each source $j$, the following objective function can be defined:

$$E = \frac{1}{2} \sum_{j=1}^{S} \sum_{i=1}^{M_j} \left( (\Gamma_{j,i})_{\text{mea}} - (\Gamma_{j,i})_c \right)^2, \tag{3}$$

where $\Gamma_{j,i}$ represents the photon intensity measured at position $\varsigma_{j,i}$ with the incident excitation source located at $\xi_j$. The subscript $c$ denotes the values calculated by the forward simulation and mea represents the experimental values.

In practice, the attenuations of launch fibers are inconsistent. So do that of the detector fibers bundles. It means that calibration should be performed to eliminate the effect of the inconsistent attenuations of fibers or fibers bundles. In order to avoid the calibration procedure, in this paper, two sets of data are sampled for relative image reconstruction. One is acquired before the absorber is embedded inside the intralipid. The corresponding measurement is $(\Gamma_{j,i})_{\text{bef}}$. The other is acquired after the absorber is immersed into the intralipid and the corresponding measurement is $(\Gamma_{j,i})_{\text{aft}}$. The measurements $(\Gamma_{j,i})_{\text{mea}}$ in (3) and following equations are given by the formula $(\Gamma_{j,i})_{\text{mea}} = (\Gamma_{j,i})_{\text{aft}}/(\Gamma_{j,i})_{\text{bef}}$, which are relative quantities. So the calculated values $(\Gamma_{j,i})_c$ are also relative quantities.

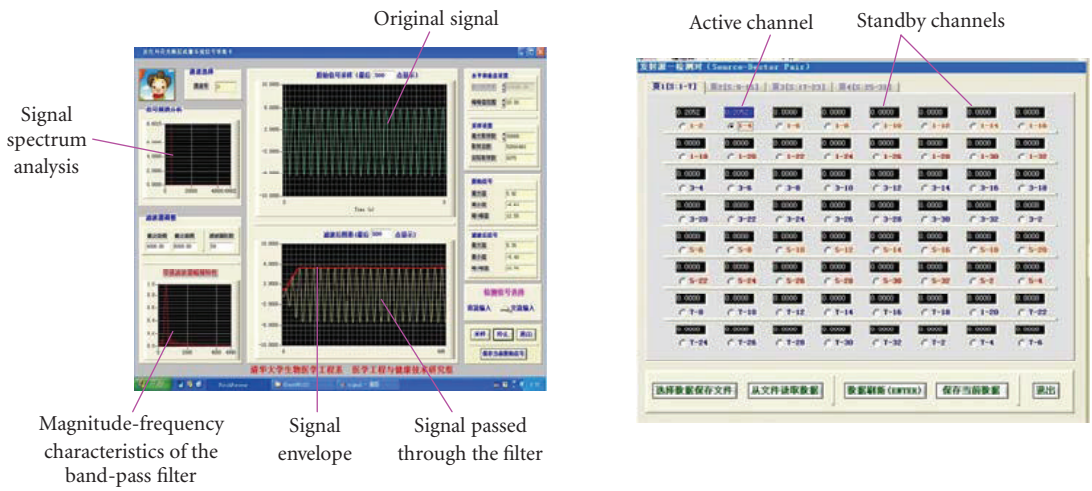


Figure 6: Data acquisition and signal processing GUI.

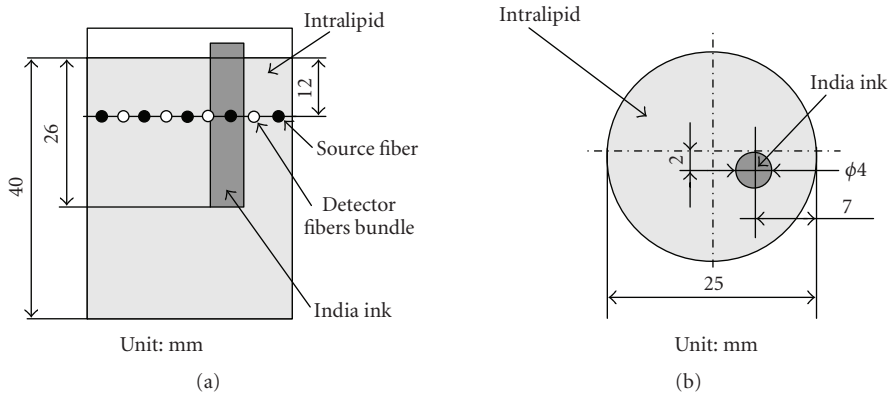


Figure 7: An experimental model.

In our work, conjugate gradient (CG) method is used to minimize the objective function. First, the gradient of the objective function needs to be calculated as follow:

$$\nabla E = \sum_{j=1}^{S} \sum_{i=1}^{M_j} \left( (\Gamma_{j,i})_{\text{mea}} - (\Gamma_{j,i})_c \right) \cdot \left( - \frac{\partial (\Gamma_{j,i})_c}{\partial \mu_a} \right). \quad (4)$$

Therefore, the gradient vector $\vec{z}$ can be presented as

$$\vec{z} = \nabla E = -\mathbf{J}^T \mathbf{b}, \quad (5)$$

where $\mathbf{J}$ is an $M_{\text{TOT}} \times N_{\text{TOT}}$ Jacobian matrix, $M_{\text{TOT}} = \sum_{j=1}^{S} M_j$ is the total measurement number at the boundary, and $N_{\text{TOT}}$ is the number of the coefficients to be reconstructed. Here $\mathbf{b}$ is the residual error between the boundary measurements and computation values. Then $\mathbf{J}$ can be calculated by an adjoint source scheme based on the establishment of PMDF (photon measurement density function, as defined in [23]).

With the gradient calculated, the next step is to conduct one-dimension search in order to find the best step length on this gradient direction. Then, we refresh the absorption coefficient and recalculate the gradient to form iteration computing until the error reaches the supposed value.

## 4. RESULTS AND DISCUSSION

To test the proposed imaging system, some experiments were performed, of which one model is illustrated in Figure 7.

In the experiment, a glass cup was filled with 1% intralipid, a tissue-like medium. The cup was mounted in the imaging tube. The intralipid is a homogeneous medium, namely, its anisotropic factor $g = 0$. A glass tube of India ink was employed as the heterogeneous object, that is, the simulated absorber. The launch fibers and the detector fibers bundles were held in the imaging tube on the same ring, and they were separated uniformly. Two sets of data were acquired for relative image reconstruction. They were sampled, respectively, before and after the India ink was embedded inside the intralipid. Their geometries and positions are illustrated in Figure 7.

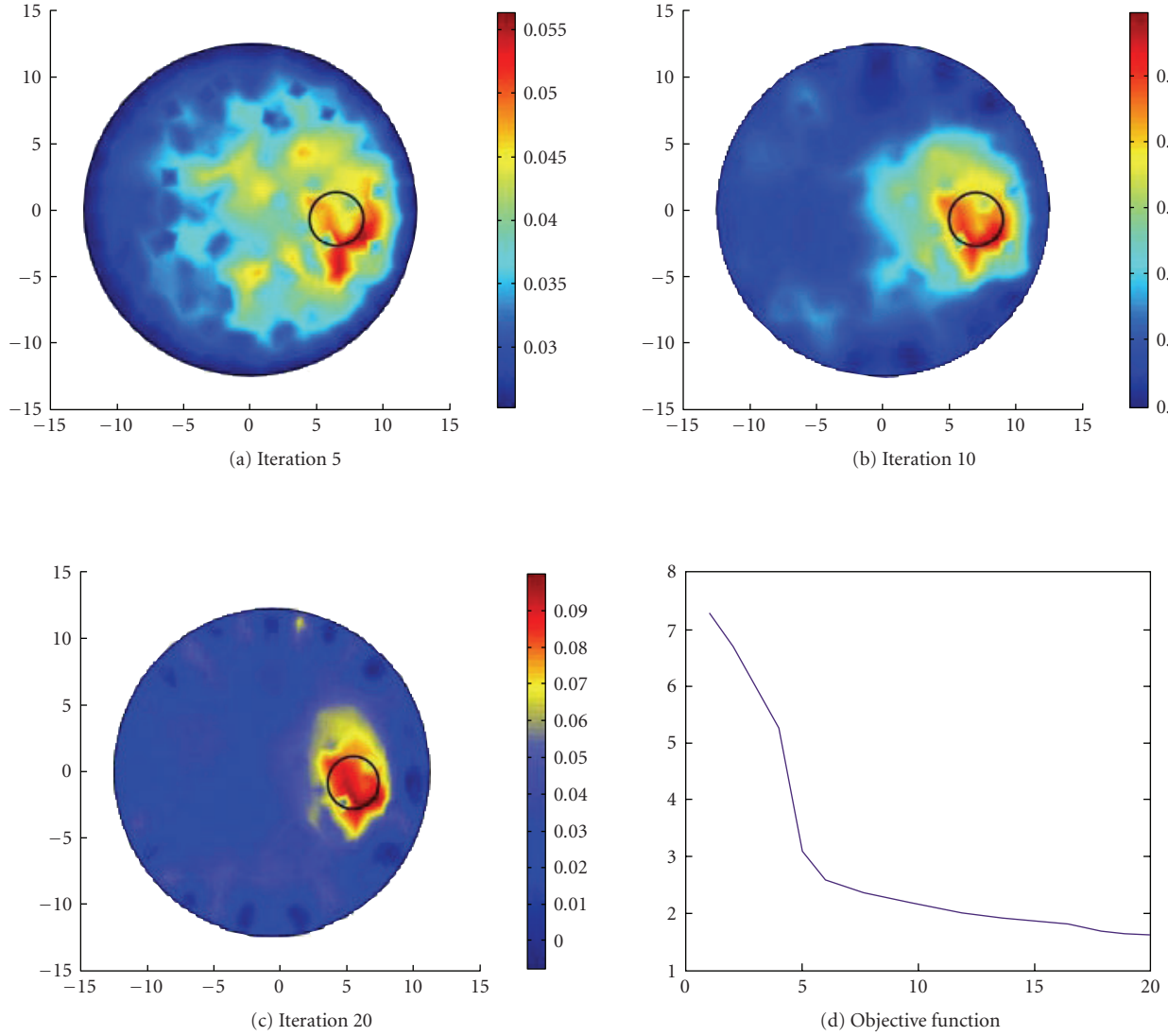


Figure 8: Reconstruction results.

The reconstruction results are illustrated in Figure 8. In Figure 8(a) to Figure 8(c), the circle inside the domain $\Omega$ stands for the true size and position of the absorber. We can see, as the iterations increase, the reconstructed result converges gradually to its true solution. The curve of the objective function (3) is shown in Figure 8(d). The other models used to test the imaging system can also derive the desired results. These experimental results suggest that the proposed imaging system is effective.

To solve the DOT is a typical inverse problem. Inverse problem is intrinsically ill-posed, which means that the solution to the problem may not exist (existence) or is not unique (uniqueness), or does not depend continuously on the data (stability) [24, 25]. For a practical physics problem, the existence and uniqueness of the solution can be satisfied naturally or be enforced by mathematical measures. So the stability is the most important profile. If a problem lacks the property of stability, a little of fluctuation of the measured data may lead to the solution deviated significantly from its true solution. To reduce the ill-posedness, regularizations strategies, such as Tikhonov regularization and Landweber iteration, are often employed [24]. However it is essentially expected that the noise polluted the measured data is as small as possible, while it is unavoidable. So in the next generation of the imaging instrumentation, some measures would be taken to eliminate to a great extent the effect of noise. For example, cooling system is employed on the PMT to reduce the dark current.

To understand the model of the noise is very useful to eliminate its influence by using appropriate algorithm. In the imaging instrumentation there are mainly three kinds of noise: thermal noise, shot noise, and relative intensity noise [26]. Usually the shot noise is the principal noise in the imaging system, which mainly rises from the dark current of the photodetector. The shot noise statistics has its origin in Poisson statistics [27]. When the current is significantly large, it is

governed by the Gaussian distribution. In this case, the statistical method, such as Bayesian framework, is suitable for the inverse problem [28, 29].

In addition, solving DOT is also a highly underdetermined problem, since the number of the measured data is much less than that of the pixels to be reconstructed. In above experiment, the forward problem was solved by the finite element method (FEM) software and the tissue domain $\Omega$ was divided into 1644 elements. However, there are only 16 sources and 16 detectors, namely, 256 known data are available. The number of the known data is much less than that of the elements. It means that the problem is considerably underdetermined. The underdetermining nature is one of the main factors that influences the quality of the reconstructed image, especially the spatial resolution. As noted in the literature [30]: A lack of information cannot be remedied by any mathematical trickery! The most important way to improve the quality of the image is to obtain prior information as more as possible, for example, acquire more data, or take advantage of the anatomical imaging or the physiology information in the reconstruction process.

## ACKNOWLEDGMENTS

This research was partially supported by the National Basic Research Program of China (2006CB705700), the National Natural Science Foundation of China (30670577, 60571013, 60331010), and the Tsinghua-Yue-Yuen Medical Science Foundation.

## REFERENCES

[1] F. E. W. Schmidt, M. E. Fry, E. M. C. Hillman, J. C. Hebden, and D. T. Delpy, "A 32-channel time-resolved instrument for medical optical tomography," *Review of Scientific Instruments*, vol. 71, no. 1, pp. 256–265, 2000.

[2] J. C. Hebden, S. R. Arridge, and D. T. Delpy, "Optical imaging in medicine: I. Experimental techniques," *Physics in Medicine and Biology*, vol. 42, no. 5, pp. 825–840, 1997.

[3] A. P. Gibson, J. C. Hebden, and S. R. Arridge, "Recent advances in diffuse optical imaging," *Physics in Medicine and Biology*, vol. 50, no. 4, pp. R1–R43, 2005.

[4] W. Du, Y. Wang, Q. Luo, and B.-F. Liu, "Optical molecular imaging for systems biology: from molecule to organism," *Analytical and Bioanalytical Chemistry*, vol. 386, no. 3, pp. 444–457, 2006.

[5] S. Kumar and R. Richards-Kortum, "Optical molecular imaging agents for cancer diagnostics and therapeutics," *Nanomedicine*, vol. 1, no. 1, pp. 23–30, 2006.

[6] W. M. Leevy, S. T. Gammon, H. Jiang, et al., "Optical imaging of bacterial infection in living mice using a fluorescent near-infrared molecular probe," *Journal of the American Chemical Society*, vol. 128, no. 51, pp. 16476–16477, 2006.

[7] D. A. Boas, D. H. Brooks, E. L. Miller, et al., "Imaging the body with diffuse optical tomography," *IEEE Signal Processing Magazine*, vol. 18, no. 6, pp. 57–75, 2001.

[8] D. A. Benaron, S. R. Hintz, A. Villringer, et al., "Noninvasive functional imaging of human brain using light," *Journal of Cerebral Blood Flow and Metabolism*, vol. 20, no. 3, pp. 469–477, 2000.

[9] M. A. Franceschini, V. Toronov, M. E. Filiaci, E. Gratton, and S. Fantini, "On-line optical imaging of the human brain with 160-ms temporal resolution," *Optics Express*, vol. 6, no. 3, pp. 49–57, 2000.

[10] J. C. Hebden, A. Gibson, R. M. Yusof, et al., "Three-dimensional optical tomography of the premature infant brain," *Physics in Medicine and Biology*, vol. 47, no. 23, pp. 4155–4166, 2002.

[11] B. W. Pogue, S. P. Poplack, T. O. McBride, et al., "Quantitative hemoglobin tomography with diffuse near-infrared spectroscopy: pilot results in the breast," *Radiology*, vol. 218, no. 1, pp. 261–266, 2001.

[12] V. Ntziachristos and B. Chance, "Probing physiology and molecular function using optical imaging: applications to breast cancer," *Breast Cancer Research*, vol. 3, no. 1, pp. 41–46, 2001.

[13] S. R. Arridge, "Optical tomography in medical imaging," *Inverse Problems*, vol. 15, no. 2, pp. R41–R49, 1999.

[14] G. Gulsen, B. Xiong, O. Birgul, and O. Nalcioglu, "Design and implementation of a multifrequency near-infrared diffuse optical tomography system," *Journal of Biomedical Optics*, vol. 11, no. 1, Article ID 014020, 10 pages, 2006.

[15] N. G. Chen, M. Huang, H. Xia, D. Piao, E. Cronin, and Q. Zhu, "Portable near-infrared diffusive light imager for breast cancer detection," *Journal of Biomedical Optics*, vol. 9, no. 3, pp. 504–510, 2004.

[16] R. Khalaf, P. van der Zee, L. Dixon, and A. Davies, "Image reconstruction for optical tomography using photon density waves," in *Photon Propagation in Tissues IV*, vol. 3566 of *Proceedings of SPIE*, pp. 211–221, Stockholm, Sweden, September 1999.

[17] S. R. Arridge and M. Schweiger, "A gradient-based optimisation scheme for optical tomography," *Optics Express*, vol. 2, no. 6, pp. 213–226, 1998.

[18] S. R. Arridge, "Photon measurement density functions—part I : analytical forms," *Applied Optics*, vol. 34, no. 31, pp. 7395–7409, 1995.

[19] S. J. Matcher, "Nonuniqueness in optical tomography: relevance of the P1 approximation," *Optics Letters*, vol. 24, no. 23, pp. 1729–1731, 1999.

[20] S. R. Arridge and W. R. B. Lionheart, "Nonuniqueness in diffusion-based optical tomography," *Optics Letters*, vol. 23, no. 11, pp. 882–884, 1998.

[21] R. Weissleder, "A clearer vision for in vivo imaging," *Nature Biotechnology*, vol. 19, no. 4, pp. 316–317, 2001.

[22] J. Zhou, J. Bai, and P. He, "Spatial location weighted optimization scheme for DC optical tomography," *Optics Express*, vol. 11, no. 2, pp. 141–150, 2003.

[23] S. R. Arridge and M. Schweiger, "Photon measurement density functions—part II: finite element method calculations," *Applied Optics*, vol. 34, no. 34, pp. 8026–8037, 1995.

[24] A. Kirsch, *An Introduction to the Mathematical Theory of Inverse Problems*, Springer, New York, NY, USA, 1996.

[25] W. E. Heinz, H. Martin, and N. Andreas, *Regularization of Inverse Problems*, Kluwer Academic Publishers, Dordrecht, The Netherlands, 2000.

[26] T. Tu, Y. Chen, J. Zhang, X. Intes, and B. Chance, "Analysis on performance and optimization of frequency-domain near-infrared instruments," *Journal of Biomedical Optics*, vol. 7, no. 4, pp. 643–649, 2002.

[27] R. H. Kingston, *Detection of Optical and Infrared Radiation*, Springer, New York, NY, USA, 1978.

[28] J. C. Ye, K. J. Webb, C. A. Bouman, and R. P. Millane, "Optical diffusion tomography by iterative-coordinate-descent optimization in a Bayesian framework," *Journal of the Optical Society of America A*, vol. 16, no. 10, pp. 2400–2412, 1999.

[29] J. C. Ye, C. A. Bouman, K. J. Webb, and R. P. Millane, "Nonlinear multigrid algorithms for Bayesian optical diffusion tomography," *IEEE Transactions on Image Processing*, vol. 10, no. 6, pp. 909–922, 2001.

[30] C. Lanczos, *Linear Differential Operators*, Van Nostrand, New York, NY, USA, 1961.

Hindawi Publishing Corporation
International Journal of Biomedical Imaging
Volume 2007, Article ID 79710, 9 pages
doi:10.1155/2007/79710

*Research Article*

# Development of a Confocal Optical System Design for Molecular Imaging Applications of Biochip

**Guoliang Huang,[1,2] Shukuan Xu,[1,2] Jiang Zhu,[1,2] Cheng Deng,[1,2] Zhonghua Dong,[1,2] Yang Yang,[1,2] Xiaoyong Yang,[2] Xianhua Wang,[2] and Guofan Jin[3]**

[1] *Medical Systems Biology Research Center, School of Medicine, Tsinghua University, Beijing 100084, China*
[2] *National Engineering Research Center for Beijing Biochip Technology, Beijing 102206, China*
[3] *Department of Precision Instruments and Mechanology, School of Mechanical Engineering, Tsinghua University, Beijing 100084, China*

Received 19 April 2007; Revised 23 June 2007; Accepted 15 July 2007

Recommended by Jie Tian

A novel confocal optical system design and a dual laser confocal scanner have been developed to meet the requirements of highly sensitive detection of biomolecules on microarray chips, which is characterized by a long working distance ($w_d > 3.0$ mm), high numerical aperture (NA = 0.72), and only 3 materials and 7 lenses used. This confocal optical system has a high scanning resolution, an excellent contrast and signal-to-noise ratio, and an efficiency of collected fluorescence of more than 2-fold better than that of other commercial confocal biochip scanners. The scanner is as equally good for the molecular imaging detection of enclosed biochips as for the detection of biological samples on a slide surface covered with a cover-slip glass. Some applications of gene and protein imagings using the dual laser confocal scanner are described.



## 1. INTRODUCTION

Systems biology is a discipline that examines the organizational relationships between biological structures in an organism, and thus it covers a very broad scope of biology from the macroscopic to the microscopic biology of organisms, ranging from mankind and other animals, plants, and microorganisms to their organs, tissues, cells, and subcellular organelles and structures through to molecular structures and the interactions between different molecular structures and systems. This broad scope of systems biology demands many different types of instruments for different aspects of imaging and signal detection. Instruments and devices such as cameras and X-ray imaging systems are used for whole organism imaging in man and larger animals [1, 2], IVIS imaging system has been developed for small animal imaging in vivo [3], ultrasonic devices are applied for the organ and tissue imaging [4], the ultraview living cell imager has been developed for cells and subcellular imaging [5], and various types of biochip have been designed for the analysis of the tissue, cells, and molecular structures [6]. Except for ultrasonic devices, all of the above detection-analysis systems require excellent optical design for the best performance of their particular objectives. One important type of optical system useful for the analysis of subcellular and molecular structures is the confocal chip scanner with a low background noise.

Advanced biochip analysis platforms [7, 8] analyze the content of a particular microarray slide chip, including gene chips, protein chips, cell chips, tissue chips, and others. Many researchers work with small molecule biochips, used for the detection of DNA variations by DNA hybridization, of proteins by the immunoreaction of proteins, and other more specialist analyses such as for DNA sequencing, ligase chain reaction (LCR), and others. Some important biochip detection systems [9, 10] have been developed, such as the fluorescence microscope imaging system and the laser confocal scanner. In all these detection systems, optical design has played a keyrole in obtaining high-clarity images of microscopic objects, and the optical objective is crucial to the detection sensitivity, the resolving power, and the working distance of the detection system. Usually, the bigger the numerical aperture of the objective, the higher its resolving power, and the higher the power of collecting the fluorescence signals bound on the tested object, however to achieve this

structure, the working distance of the objective must also be shorter. For example, when the conventional microscope objective has an NA > 0.6, then its working distance $w_d$ is usually smaller than 1 mm. For example, the Zeiss plan objective 440050, magnification 40×, NA = 0.65, $w_d$ = 0.6 mm, and the Nikon plan objective model 40×, NA = 0.65, and $w_d$ = 0.57 mm.

In this paper, a novel confocal optical system design and a dual laser confocal scanner are described in which the materials and lenses employed are as small as practicable; the optical design and the potential pitfalls of an objective with a long working distance and a high numerical aperture have been considered and resolved for application to biochips. The collecting fluorescence has very high efficiency, and generally the instrument has excellent resolving power and an excellent signal-to-noise ratio.

## 2. CONFOCAL OPTICAL SYSTEM DESIGN AND ANALYSIS

### 2.1. A newly developed confocal optical system design

The design of a confocal optical system with high-performance detection of biological sample slides and biochips centers around the image quality, including the consideration of the resolution, zoom, aberration, and optical transfer functions, each of which can be optimized by using rays tracing calculations. In the process of optical design, all parameters of the optical system structure, including the surface curvature radius of each lens, the thickness of the lenses, the transmitted materials used, the separation distances, and the surface apertures can be varied to obtain an excellent optical specificity and image quality. The functional relationships between the specificity, image quality, and structural parameters of the system can be described as follows:

$$\begin{aligned} \xi_1(\eta_1, \ldots, \eta_i) &= \psi_1 \\ &\vdots \\ \xi_k(\eta_1, \ldots, \eta_i) &= \psi_k, \end{aligned} \tag{1}$$

where $i$ and $k$ are two natural numbers, $\psi_1 \cdots \psi_k$ are various aberrations of the optical specificity and the image quality, $\xi_1 \cdots \xi_k$ are functions of the specificity, the image quality, and the structural parameters of system, $\eta_1 \cdots \eta_i$ correspond to all the structural parameters of system. Based on the polynomial expansion and the minimum binary iterative method, when all structural parameters $\eta_1 \cdots \eta_i$ are modified repeatedly, an approximate minimum aberration will be obtained in (1).

Applying the above optical design method, an optimum confocal optical system structure for the detection of biochips could be defined, as shown in Figure 1. Here, the optical imaging system is composed of sets of objective and magnifying lenses. The objective system is a combination of seven lenses including two doublets and uses only three glass materials, ZK7, ZK11, and ZF2. The objective system has a high numerical aperture of 0.72 for collecting the signal from the object, a focal length of 13.06 mm, and a front focal length of 3.22 mm to provide a working distance of approximately 3.0 mm. There is a parallel ray path between the objective and the magnifying lenses, to which it is convenient to also add the filters and the dichroic mirror for the incident laser when building the confocal scanning system. The magnifying lenses system consists of five lenses. This optical system has a zoom of 3.

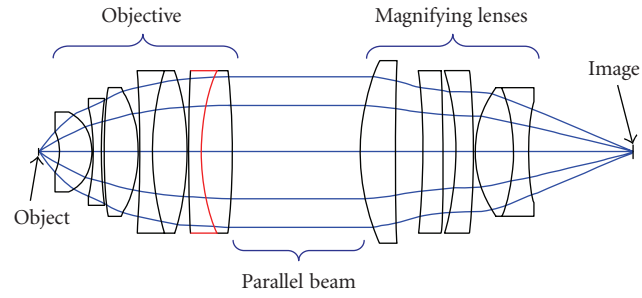


Figure 1: The main optical structure design of the confocal system.

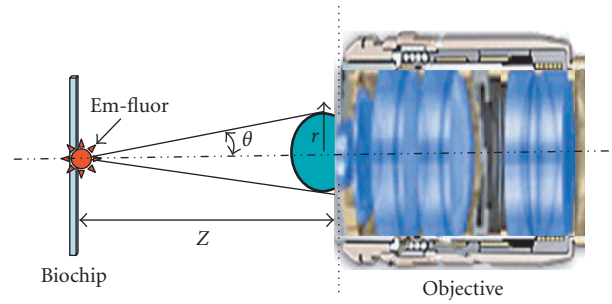


Figure 2: The configuration of the objective collecting fluorescence.

The optical structure parameters of confocal scanning system were optimized in Figure 1, where there are an objective and a magnifying lenses, the objective consists of seven lenses, the magnifying lenses consists of five lenses, there is a parallel beam between the objective and magnifying lenses. The optical structure parameters of confocal scanning system are listed in Table 1. A configuration of the objective collecting fluorescence is shown in Figure 2, where the distance from the focal plane to the front surface of first lens of objective is $Z$, $r$ is the radius of effective aperture of the objective, $\theta$ is the half of aperture angle. The emission fluorescence (Em-fluor) of molecule bound on biochips is ideally a spherical wave, and the fluorescence bound on the biochip collected by the objective as shown in Figure 2 is described approximately by the formula

$$I(Z) \approx \frac{K_0^2}{Z^2} \times \pi \times r^2, \tag{2}$$

where $K_0$ is a constant, $Z$ is the distance from the center of source in the focal plane to the first surface of objective, $r$ is the radius of effective aperture of the objective.

When biochips are placed at the focal plane of the objective, and the objective has a numerical apture NA = $n \times \mathrm{Sin}\theta$,

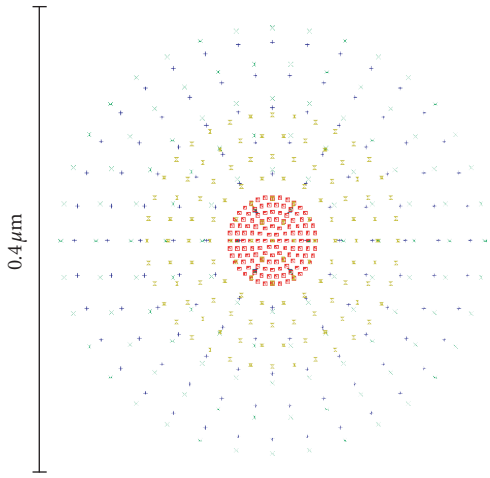


Figure 3: The spot diagram of the scanning probe.

where $n$ is the refractive index, then the formula (2) can be simplified to formula

$$I(Z) \approx \frac{1}{n^2} \times K_0^2 \times \pi \times \mathrm{NA}^2 \times (1 + \mathrm{NA}^2 + \mathrm{NA}^4 + \cdots). \tag{3}$$

Formula (3) indicates that the intensity of the collecting fluorescence of molecules on biochips has a direct ratio to the square of the higher power of the NA.

By developing a structure form using formula (3), we created a confocal optical system with a numerical aperture of 0.72, and an efficiency of collected fluorescence of more than 2-fold better than that of other commercial confocal biochip scanners [9, 10] whose objective has a smaller numerical aperture than 0.5.

### 2.2. Analysis of the new optical system design

In a confocal scanning system, the laser scanning spot probe determines the scanning resolution power. The smaller the laser scanning spot of optical system, the higher the scanning resolution power of the confocal system. The scanning spot diagrams are referenced to the real chief ray as shown in Figure 3. This option allows selection of two other reference points, the centroid and the middle. The centroid is defined by the distribution of the traced rays. The middle is defined so that the maximum ray errors are equal in both the $x$- and the $y$-directions. When a laser with a real beam diameter of about 1 mm is imaged by the objective shown above in Figure 1, then the spot diagram on the focal plane is as shown in Figure 3, where the scale is 0.4 $\mu$m, the spot diameter on the focal plane is smaller than 0.4 $\mu$m, which is an ideal scanning probe beam with a more high resolving power of <0.5 $\mu$m.

The optical speciality and the aberration of the imaging system of our novel optical structure can be analyzed using the optical design software ZEMAX-EE. For the spot diagram shown in Figure 3, the root mean square (RMS) radius on the focal plane is 0.105 $\mu$m, and the geometric radius on the focal plane is 0.183 $\mu$m, which corresponds to a confocal optical system with a scanning resolution power smaller than 0.4 $\mu$m.

The optical path difference (OPD) is a scalar quantity and it is identical to those for ray aberration fans at the tangential and sagittal directions PX and PY, respectively. The data plotted in Figure 4(a) is the optical path difference of the system in Figure 1, which is the difference between the optical path length of the ray and the optical path length of the chief ray. The horizontal scale of graph is the normalized entrance pupil coordinate. The vertical axis scale of graph is one wave, while the OPD maximum of system in Figure 1 is smaller than 5 waves. In Figure 4(a), there is a small optical path difference among 3 wavelengths 570 nm, 620 nm, and 670 nm, but the maximum optical path difference is smaller than 3 waves, which is lower than a normal visible light imaging system of 5 waves and can be used for confocal scanning system very well.

The encircled energy diagram is the percentage of total energy enclosed as a function of distance from either the chief ray or the centroid at the image of a point object, while the diffraction limit curve is for the aberration-free encircled energy computed on-axis. The encircled energy diagram of the system is shown in Figure 4(b), where the horizontal coordinate is the radius, and the vertical coordinate is the normalized fraction of the enclosed energy. The encircled energy diagram shows a diffused intensity spot in focal plane of system, the smaller the radius of encircled energy diagram is, the more the fluorescence energy is collected by the pinhole in the focal plane. In Figure 4(b), the radius of encircled energy diagram is smaller than 10 $\mu$m, where the efficiency of fluorescence collected is near to 100%, when a pinhole with a radius of 10 $\mu$m is set at the focal plane of the magnifying lenses, then the efficiency of collection of the fluorescence of an object is near to the diffraction limit.

Geometric image analysis is used to model extended sources, to analyze useful resolution, to represent the appearance of imaged objects, and to provide intuition as to image rotation. The diffraction image analysis accounts for the finite pass band and other diffraction-related effects of real optical systems based upon Fourier Optics. The diffraction image analysis of the system is shown in Figure 5. The geometric image analysis of the optical system is shown in Figure 5(a), while the diffraction image analysis of the optical system in the object area illuminated by the scanning spot is shown in Figure 5(b), both of which have a high efficiency of 100%. In Figure 5(a), the geometric image analysis shows a nice roundness of model extended sources, there is good image rotation invariability of system. In Figure 5(b), the diffraction image analysis shows a nice uniformity and clear outline of the letter F as an object, there is good image quality of system to the object area illuminated.

### 2.3. The constitution of the confocal optical system

Applying the above optical design parameters, we constructed a new confocal optical scanning system which has been further developed into the advanced confocal scanner specially for biochip application, as illustrated in Figure 6,

Table 1: The optimization data of confocal scanning system. Units are measured in mm.

| Surface | Radius | Thickness | Glass | Semidiameter |
|---|---|---|---|---|
| 1 | −5.900 | 5.10 | ZK11 | 2.80 |
| 2 | −5.608 | 0.20 | — | 5.30 |
| 3 | −23.000 | 1.20 | ZF2 | 6.00 |
| 4 | 46.000 | 0.42 | — | 7.00 |
| 5 | 54.200 | 5.40 | ZK7 | 8.50 |
| 6 | −14.521 | 0.20 | — | 8.50 |
| 7 | −106.500 | 2.00 | ZF2 | 9.00 |
| 8 | 31.840 | 5.40 | ZK7 | 10.75 |
| 9 | −30.760 | 0.20 | — | 10.75 |
| 10 | 156.680 | 2.00 | ZF2 | 10.75 |
| 11 | 24.720 | 4.90 | ZK7 | 10.75 |
| 12 | −79.250 | 100.00 | — | 10.75 |
| 13 | 25.650 | 5.51 | ZK7 | 12.00 |
| 14 | 354.330 | 4.32 | — | 12.00 |
| 15 | −73.450 | 3.15 | ZF2 | 10.75 |
| 16 | −183.900 | 2.00 | — | 10.75 |
| 17 | −32.560 | 2.81 | ZF2 | 10.75 |
| 18 | −79.250 | 0.21 | — | 10.75 |
| 19 | 12.878 | 6.00 | ZK11 | 8.50 |
| 20 | −20.230 | 2.25 | ZF2 | 8.50 |
| 21 | 26.300 | — | — | — |

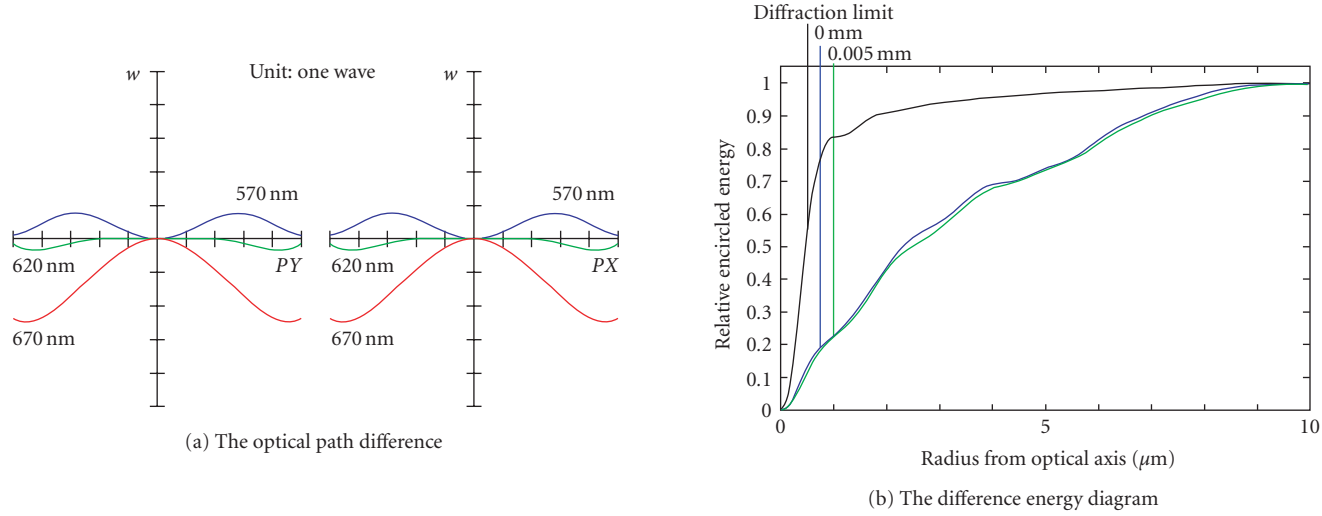


(a) The optical path difference

(b) The difference energy diagram

Figure 4: The optical path difference and the encircled energy diagram of the system.

where the objective and magnifying lenses are designed in Figure 1, two filters for the dye Cy3 and the dye Cy5 are bought from Chroma Corporation, PMT (photomultiplier tube) is bought from Hamamatsu Corporation, laser 1 is a solid laser with wavelength 532 nm and power 25 mW, laser 2 is a semiconductor laser with wavelength 635 nm and power 25 mW, splitter is a dichroic mirror from Chroma Corporation, the mirror is machined into an elliptical mirror with a small hole 1mm in center, XY scanning platform is designed with 2 $\mu$m moving control precision. Pinhole is a small hole with diameter 20 $\mu$m, A/D electronic card is designed with precision 16 bit and frequency 1 MHz. Computer is chosen with PIII CPU or higher CPU speed, biochip is developed by CapitalBio Corporation. It is characterized by an objective with a large numeral aperture of NA = 0.72, a long working distance of 3.0 mm, and a sensitivity of fluorescence detection of about 0.1 fluors/$\mu$m$^2$. Compared to other similar commercial scanners, it has a higher-resolution power and an excellent signal-to-noise ratio. In Figure 6, when the laser beam irradiates the biochip on the XY scanning platform

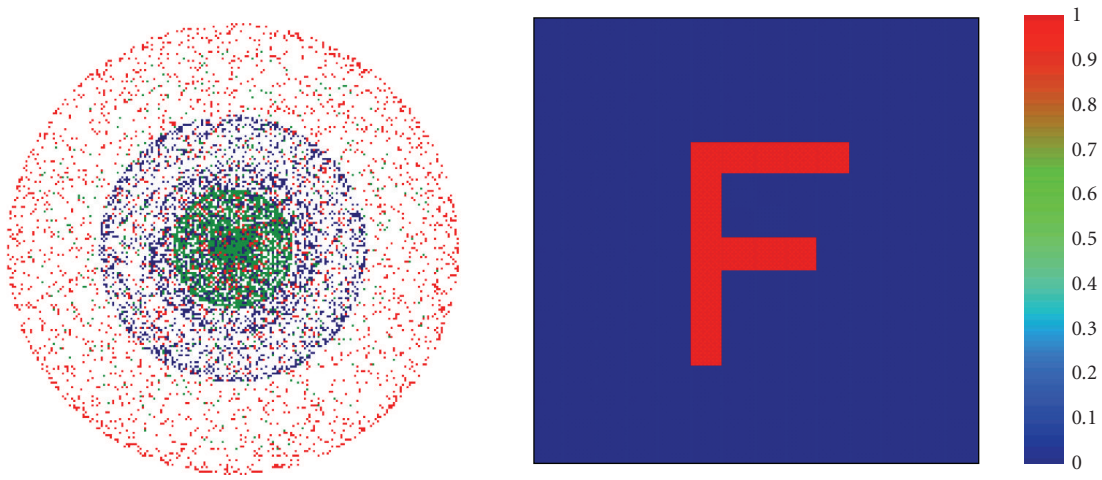


(a) The geometric image analysis (b) The diffraction image analysis

Figure 5: The geometric and diffraction image analyses of the system illustrated in Figure 1.

from the laser 1 with wavelength 532 nm, or from the laser 2 with wavelength 635 nm, the fluorescence of biological sample on the biochip is induced and collected by PMT. After A/D (analogue/digital) transfer is complete, the fluorescence signal from the biochip is loaded into the computer for digital image processing.

When pairs of identical gradient signal biochips from Full Moon ( Full Moon BioSystems, Sunnyvale, Calif, USA) were labeled with either Cy3-tagged or Cy5-tagged probes, and dual color fluorescence was detected by using our newly developed confocal scanner and by another commercial confocal scanner (US popular brand S), the features of the scanning image analyses are shown in Figures 7(a)–7(d), where the right small spot array image is a local area magnifying view for left scanning images. Our newly developed confocal scanner shows a high scanning resolution, an excellent contrast, and a signal-to-noise ratio seen in Figures 7(a) and 7(c). The detection sensitivity of the new confocal scanner was further illustrated in Figure 7(e), where a Full Moon (Full Moon BioSystems, Sunnyvale, Calif, USA) normal molecular density biochip was used and the unit of density is the molecule number per the square micron, and the signal is the relative intensity in the range of 0 to 65 535. In Figure 7(e), a molecule with a density of 0.071 fluors/$\mu$m$^2$ was detected with a signal of 547, where SNR (signal-to-noise ratio) is greater than 2, which indicates that the new confocal scanner is with a sensitivity of fluorescence about 0.1 fluors/$\mu$m$^2$.

## 3. THE APPLICATION TO BIOCHIPS

### 3.1. The gene expression analysis

The gene expression analysis is an important method to study the different gene functions of organisms, which is usually performed on high-density biochips with several tens of thousands of probes in a small 20 mm $\times$ 60 mm area, where dual fluorescent color labels with the dyes Cy3 and Cy5 can be used to produce a gene expression spectrum. In order to analyze the gene expression of biochips, it is important for the scanning system to possess high scanning resolution, an excellent contrast, and signal-to-noise ratio, over a wide range of signal intensities. The newly developed confocal optical scanning system can be readily used for the gene expression analysis of biochips. The gene expression spectrum for a high-yield variety of cotton as shown in Figure 8 was obtained by using the developed confocal scanner.

In Figure 8, the dual fluorescent color-labeled biochips were hybridized with 15 reference probes at the beginning of first row and with 687 gene reporter probes representing expressed genes from the two cottons. Messanger RNA from common cotton was labeled with Cy3, and mRNA from a high-yield cotton was labeled with Cy5. The dual fluorescent color-labeled biochips were scanned twice using the new confocal scanner, where one scan was illuminated by the green laser with a wavelength 532 nm to induce fluorescence of Cy3, and the second scan was illuminated by the red laser with a wavelength 635 nm to induce the fluorescence of Cy5. Figure 8(a) is the image of the gene expression spectrum of the common cotton labeled with Cy3, and Figure 8(b) is the image of the gene expression spectrum of the high-yield cotton labeled with Cy5. Figure 8(c) is the combined images of the gene expression spectrums from both the high-yield cotton and the common cotton, where there is an obvious color change if there is a difference between the level of gene expression of mRNAs labeled by Cy3 and by Cy5. Figure 8(d) is the scatter plot of gene expression to analyze the differences between the gene message labeled with Cy3 to message labeled with Cy5, where the identical level of expression of the same genes in the two plant varieties distributes along the line direction of 45 degrees with increasing relative intensity of signals. The larger the difference of gene expression between the two varieties, the farther the position of gene in the scatter plot is away from the 45-degree line.

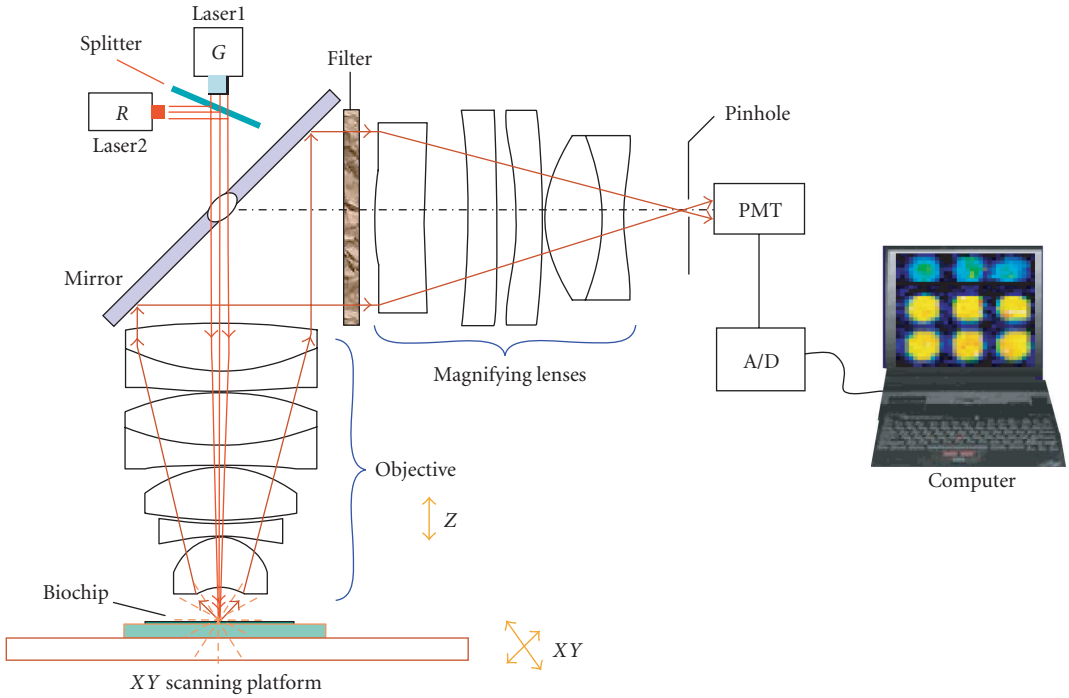


Figure 6: The newly developed confocal optical scanning system.

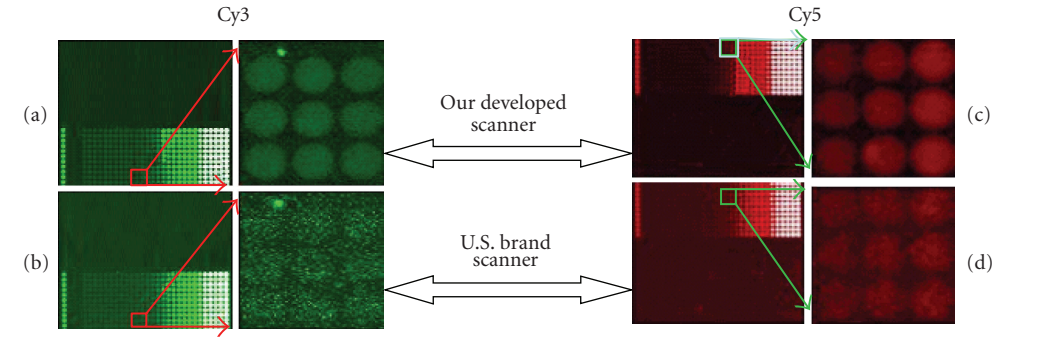


| Images | | | | | | | | | | | | | | | | | | |
|---|---|---|---|---|---|---|---|---|---|---|---|---|---|---|---|---|---|---|
| | 1 | 2 | 3 | 4 | 5 | 6 | 7 | 8 | 9 | 10 | 11 | 12 | 13 | 14 | 15 | 16 | 17 | 18 |
| Density | 0.071 | 0.14 | 0.28 | 0.561 | 1.12 | 2.24 | 4.49 | 8.97 | 17.9 | 35.9 | 71.8 | 144 | 287 | 574 | 1150 | 2300 | 4590 | 9190 |
| Signal | 547 | 565 | 608 | 617 | 628 | 651 | 712 | 810 | 924 | 1140 | 1520 | 2267 | 3931 | 6749 | 13385 | 25907 | 51660 | 65414 |

(e)

Figure 7: The analysis features of the newly developed confocal scanner.

In Figure 8(d), except for 15-reference probes at row 1, there are 36 genes with a 2-fold signal difference between the common cotton and the high-yield cotton, distributed over a broad range of relative signal intensities, which shows that there are 36 important genes to improve the yield of cotton.

### 3.2. The detection of immunoreaction of proteins

The new confocal scanner is also useful for fluorescence detection of the immunoreactions of proteins on chips. We describe here a protein microarray chip for the parallel detection of autoantibodies in the serum of patients with autoimmune diseases, including systemic lupus erythmatosus (SLE), mixed connective tissue disease (MCTD), Sjögren's syndrome (SS), Sjögren's syndrome A (SSA), Sjögren's syndrome B(SSB), Smith (Sm), Ribonucleoprotein (RNP), Scleroderma (Scl), systemic sclerosis (SSc), dermotomyositis (DM), double-stranded DNA(dsDNA), Phosphate-Buffered Saline Tween-20(PBST), and polymyositis (PM). Purified autoantigens (SSA-52, SSA-60, SSB, Sm, RNP-68, Scl-70,

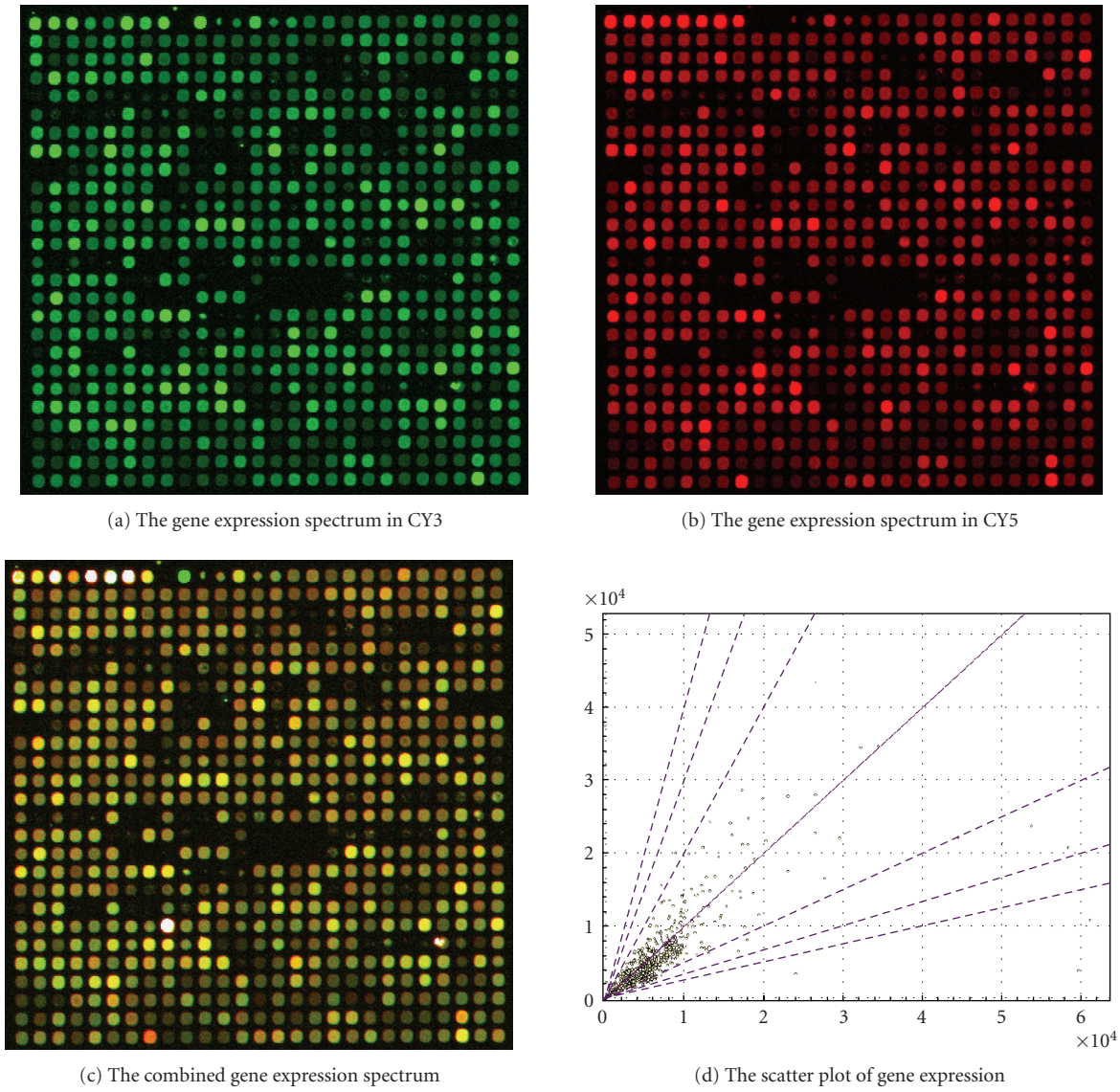


(a) The gene expression spectrum in CY3

(b) The gene expression spectrum in CY5

(c) The combined gene expression spectrum

(d) The scatter plot of gene expression

Figure 8: The gene expression spectra of a high-yield cotton compared to a common cotton variety.

Jo-1, dsDNA, centromere B, Ribosomal P0, and extracts of Hep-2 cells) are immobilized on the gel chip as shown in Figure 9(a), where QC—quality control, BC—blank control, RC—reaction control, NC—negative control, 1-Jo-1, 2-Sm, 3-Scl-70, 4-CENP-B, 5-dsDNA, 6-SSB, 7-SSA-52, 8-Extracts of Hep-2 cells, 9-SSA-60, 10-Ribosomal P0, 11-RNP-68. The protein microarray chip was incubated with 30 $\mu$L of a five diseases-mixed serum (diluted 1 : 100 with PBST) for 30 minutes at room temperature. After being rinsed and washed one time for 5 minutes with PBST, the chip was incubated with 30 $\mu$L of Cy3-labeled goat antihuman IgG antibody for 30 minutes at room temperature. After another rinse and 5-minutes PBST wash, the chip was briefly centrifuged to dry it. The mixed serum of SLE, SS, SSc, MCTD, DM, and PM positive sera patient was tested on the protein microarray chip, which was then scanned using our confocal scanner. The result of scanning image in Figure 9(b) clearly showed that this mixed sera contained anti-Jo-1 at row 2 from column 1 to column 3, anti-Sm at row 2 from column 4 to column 6, anti-Scl-70 at row 2 from column 7 to column 9, anticentromere B at row 3 from column 1 to column 3, anti-dsDNA at row 3 from column 4 to column 6, anti-SSB at row 3 from column 7 to column 9, anti-SSA-52 at row 4 from column 1 to column 3, antinuclear antibodies at row 4 from column 7 to column 9, anti-SSA-60 at row 5 from column 1 to column 3, anti-Ribosomal P0 at row 5 from column 4 to column 6, and anti-RNP-68 at row 5 from column 7 to column 9.

## 4. DISCUSSION AND CONCLUSION

This developed confocal scanner is good for some applications of biochips, such as DNA hybridization and immunoreaction of proteins. The long workingdistance of the newly

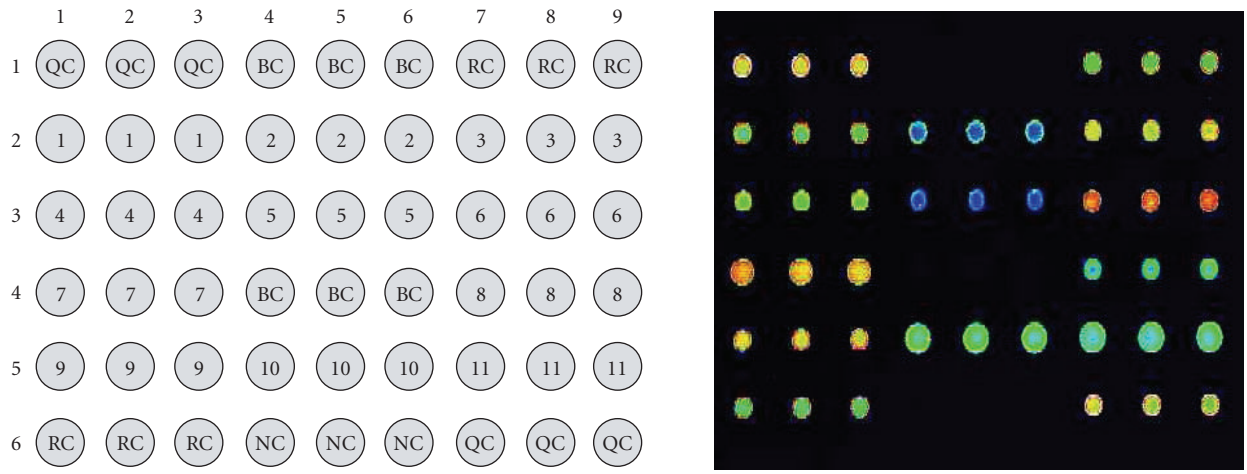


(a) The probe design of protein chip

(b) The scanning image of protein chip

Figure 9: The application of protein chip for autoantibodies in patients serum.

developed confocal scanner has a particular advantage for work with biochips enclosed with a hybridization gasket, or conventional microscope slides with thick covers, or even with an uncovered liquid surface. This feature is necessary for observation of real-time (RT) events on the chip surfaces, such as monitoring RT-fluorescence PCR. The high scanning resolution power available with a scanning beam of 0.4 $\mu$m and with a sensitivity of detected fluorescence of 0.1 fluors/$\mu$m$^2$ are both important for obtaining an excellent images of small objects with quite clear definition, high contrast, and with a high signal-to-noise ratio. This improved clarity of the images could be seen when comparing scans of a Full Moon normal molecular density biochip by using our developed confocal scanner with that of using another commercial confocal scanner (see Figure 7).

When compared to other common microscope objective designs where the objective of a typical microscope has a numerical aperture of NA = 0.65 and a working distance smaller than 1 mm (such as the Zeiss plan objective 440050, magnification 40×, NA = 0.65, $w_d$ = 0.6, $w_d$ = 0.6 mm, and the Nikon plan objective model 40×, NA = 0.65, $w_d$ = 0.6, $w_d$ = 0.57 mm), it is obvious that the optical design of the newly developed confocal scanning system is highly advanced, with an optimum combination of lenses, including a high numerical aperture of 0.72, a long working distance of 3.0 mm. The use of only 7 lenses and only 3 different kinds of optical glasses of ZK7, ZK11, and ZF2 is also beneficial. The limited number of glasses and lenses reduces the compound aberration in the use of large numbers of lenses and multiple glasses. In addition, these glass materials favor manufacture with small material error and small machining error.

Furthermore, the developed confocal scanner can be used for scanning cells and tissues slide, and because the high numerical aperture optical design has a very short focal depth 0.7 $\mu$m, it is also good for the tomography imaging of a cubic object.

## ACKNOWLEDGMENTS

This work is supported by the National Foundation of High Technology of China Grants no. 2006AA020701 and 2006AA020803, the National Program on Key Basic Research Projects 973 of China (2006CB705700), the Nature Science Foundation of Zhejiang Province (2006C21G3210005), the Tsinghua Foundation (052205003), and the Tsinghua-Yuyuan Medicine Foundation (40000510B). Keith Kmitchelsonis thankfully acknowledged for checking English. Zhang Liang, Zhao Zhixian, and their groups are thankfully acknowledged for undertaking the gene expression analysis and protein immunoreactions.

## REFERENCES

[1] E. Seeram, *Computed Tomography: Physical Principles, Clinical Applications, and Quality Control*, Saunders, Philadelphia, Pa, USA, 2nd edition, 2001.

[2] Y. Tang, M. Kim, D. Carrasco, A. L. Kung, L. Chin, and R. Weissleder, "In vivo assessment of RAS-dependent maintenance of tumor angiogenesis by real-time magnetic resonance imaging," *Cancer Research*, vol. 65, no. 18, pp. 8324–8330, 2005.

[3] S. Gross and D. Piwnica-Worms, "Real-time imaging of ligand-induced IKK activation in intact cells and in living mice," *Nature Methods*, vol. 2, no. 8, pp. 607–614, 2005.

[4] F. Forsberg, "Ultrasonic biomedical technology; marketing versus clinical reality," *Ultrasonics*, vol. 42, no. 1–9, pp. 17–27, 2004.

[5] J. C. Canman, L. A. Cameron, P. S. Maddox, et al., "Determining the position of the cell division plane," *Nature*, vol. 424, no. 6952, pp. 1074–1078, 2003.

[6] T. A. Patterson, E. K. Lobenhofer, S. B. Fulmer-Smentek, et al., "Performance comparison of one-color and two-color platforms within the microarray quality control (MAQC) project," *Nature Biotechnology*, vol. 24, no. 9, pp. 1140–1150, 2006.

[7] S. P. Fodor, J. L. Read, M. C. Pirrung, L. Stryer, A. T. Lu, and D. Solas, "Light-directed, spatially addressable parallel chemical synthesis," *Science*, vol. 251, no. 4995, pp. 767–773, 1991.

[8] P. O. Brown and D. Botstein, "Exploring the new world of the genome with DNA microarrays," *Nature Genetics*, vol. 21, supplement 1, pp. 33–37, 1999.

[9] L. Warren, D. Bryder, I. L. Weissman, and S. R. Quake, "Transcription factor profiling in individual hematopoietic progenitors by digital RT-PCR," *Proceedings of the National Academy of Sciences of the United States of America*, vol. 103, no. 47, pp. 17807–17812, 2006.

[10] D. Robyr, Y. Suka, I. Xenarios, et al., "Microarray deacetylation maps determine genome-wide functions for yeast histone deacetylases," *Cell*, vol. 109, no. 4, pp. 437–446, 2002.

Hindawi Publishing Corporation
International Journal of Biomedical Imaging
Volume 2007, Article ID 29817, 10 pages
doi:10.1155/2007/29817

*Research Article*

# Synthesis and Bioconjugation of Gold Nanoparticles as Potential Molecular Probes for Light-Based Imaging Techniques

**Raja Gopal Rayavarapu,[1] Wilma Petersen,[1] Constantin Ungureanu,[1] Janine N. Post,[2] Ton G. van Leeuwen,[1] and Srirang Manohar[1]**

[1] *Biophysical Engineering Group, Institute for Biomedical Technology (BMTI), Faculty of Science and Technology, University of Twente, P.O. Box 217, 7500 AE Enschede, The Netherlands*
[2] *Molecular Cell Biology Group, Polymer Chemistry and Biomaterials, Institute for Biomedical Technology (BMTI), Faculty of Science and Technology, University of Twente, P.O. Box 217, 7500 AE Enschede, The Netherlands*

Received 15 January 2007; Accepted 14 June 2007

Recommended by Wenxiang Cong

We have synthesized and characterized gold nanoparticles (spheres and rods) with optical extinction bands within the "optical imaging window." The intense plasmon resonant driven absorption and scattering peaks of these nanoparticles make them suitable as contrast agents for optical imaging techniques. Further, we have conjugated these gold nanoparticles to a mouse monoclonal antibody specific to HER2 overexpressing SKBR3 breast carcinoma cells. The bioconjugation protocol uses noncovalent modes of binding based on a combination of electrostatic and hydrophobic interactions of the antibody and the gold surface. We discuss various aspects of the synthesis and bioconjugation protocols and the characterization results of the functionalized nanoparticles. Some proposed applications of these potential molecular probes in the field of biomedical imaging are also discussed.



## 1. INTRODUCTION

Optical imaging encompasses a multitude of techniques for the elucidation of morphology, molecular function, and metabolism of tissue with the general objective of detecting, diagnosing, staging, and treatment monitoring of disease. Progression of disease is usually accompanied by changes in physiology and pathology that are manifested as location-specific changes in optical properties thereby providing contrast for optical imaging to study disease.

Optical imaging techniques span the range from surface to bulk imaging systems with applications ranging from "optical biopsies" to full human breast imaging with resolutions that cover the microscopic to macroscopic. Some important imaging techniques for superficial tissue imaging are confocal microscopy [1], two-photon microscopy [2], and optical coherence tomography (OCT) [3]. Techniques that permit subsurface to deep imaging are diffuse optical imaging (DOT) [4] and photoacoustic imaging [5].

The interaction of visible and near-infrared (NIR) light with tissue is dominated by

(a) absorption processes which are due to the presence of various chromophores such as hemoglobin, oxyhemoglobin, melanin, water, and lipids [6];

(b) scattering processes due to the cell membrane and cell structures such as the nucleus, mitochondria, lysosomes [6].

Penetration of light in tissue is dependent on the extent of the two processes above and is low in the high-energy visible region of the spectrum. This is due to high absorption by hemoglobin and severe light scattering. In the wavelength regime between 600 nm and 1100 nm, absorption and scattering losses are minimal permitting high-light penetration. This is the so-called "optical imaging window" which is exploited for deep imaging in tissue [7].

The sensitivity and specificity of optical imaging techniques to visualize a pathological disorder are governed by contrast: the ability of the disease to differentially scatter or absorb light compared with nonpathological tissue and background noise. This native or endogenous contrast may not be sufficient and in any case, the interactions of light with tissue

are not disease-specific. Therefore, there is a role for exogenously administered contrast enhancing agents which have affinity for the disease site through biochemical interactions, providing not only sensitive but also disease-specific signals.

Contrast agents for optical imaging thus far have near-infrared dyes based on cyanine dyes [8] such as Indocyanine Green [9], but in the last few years, gold nanoparticles [10–12] have emerged as prime candidates due to their unusual optical properties and inherent biocompatibility.

Gold metal nanoparticles (NPs) exhibit narrow and intense absorption and scattering bands due to the phenomenon of plasmon resonance. This occurs at the resonance condition of the collective oscillation that the conduction electrons experience in an electromagnetic field of the appropriate wavelength [13]. The plasmon resonant condition of gold NPs depends upon their size, shape, structure (solid or hollow), and upon the refractive index of the embedding medium. Spherical gold nanoparticles have a single plasmon resonant extinction peak at around 520 nm, which does not shift extensively with changes in size and refractive-index of the surrounding medium. This is a wavelength at which light penetration in tissue is poor due to strong scattering and absorption by hemoglobin, and gold nanospheres are not useful in contrast enhancement for deep tissue imaging.

Rod-shaped NPs exhibit two plasmon resonances due to oscillation of the conduction electrons along the short axis as well as along the long axis of the particles. The former plasmon band is called the transverse resonance and the latter the longitudinal resonance. While the transverse plasmon band occurs in the neighborhood of 520 nm, the longitudinal band is red-shifted. The extent of the red-shift depends on the aspect ratio of the nanorod; the higher the aspect ratio, the further the shift. Thus by tailoring the length and/or width of these particles, their extinction peaks may be made to cover the low-energy visible to infrared wavelength regions.

The intense scattering and absorption of light, that occurs under the plasmon resonant condition coupled with the ability to tune the resonance into the near-infrared (NIR) by manipulating the aspect ratio, make gold nanorods extremely attractive as contrast agents for optical imaging techniques. Further, gold-protein chemistry is well developed and several bioconjugation protocols are available in the literature, which allows the combination of the targeting functionality of antibodies with such gold NPs. The inertness and biocompatibility of gold in general hold promise the use of gold NPs for in vivo imaging applications.

Gold NPs can be synthesized using wet chemical methods which are based on the reduction of gold salts by reagents such as sodium borohydride and ascorbic acid. Seed-mediated methods dominate wet chemical synthesis routes. These involve the reduction of gold using weak reducing agents onto small nanospheres of gold as seed, in the presence of shape-directing surfactants usually cetyl trimethylammonium bromide (CTAB). These methods may be distinguished into those that use silver ion assistance in growth solutions and those that do not.

Murphy and coworkers described the three-step growth protocol [14, 15], where medium to high aspect ratio nanorods could be synthesized, without the use of silver nitrate. Seed particles are generated by reducing gold salt using sodium borohydride in the presence of sodium citrate. The spheres are coated with a layer of negatively charged citrate ions that maintain colloid stability against aggregation by electrostatic repulsion. These spheres seed a growth solution comprising gold salt, CTAB, and ascorbic acid in three steps thereby slowing down reduction. The mechanism of nanorod formation by this method is not yet fully understood. Murphy et al. [15] proposed that the polar $CTA^+$ head group of the surfactant binds with greater preference to certain crystallographic faces thereby passivating them to the deposition of gold. The other faces, on the other hand, would be exposed for gold to be reduced on, thereby producing anisotropic growth into rods.

The methods using silver nitrate in the growth solutions were proposed by Jana et al. [16], but modified by Nikoobakht and El-Sayed [17] to achieve spectacular yields of nanorods with excellent monodispersity. Importantly, they also showed that changing the quantity of $Ag^+$ ions in the growth solution allows for fine-tuning of the aspect ratios of the nanorods. The mechanism at work in this protocol has been debated in the recent past. One mechanism postulates CTAB as a soft template which elongates on addition of $Ag^+$ ions which occupy regions between the $CTA^+$ head groups to reduce the repulsion between the head groups [17]. A second mechanism invokes the CTAB passivation concept with additional adsorption of silver bromide on facets slowing down reduction and producing rods shorter than those made without using $Ag^+$ [18]. A third mechanism which has appeared recently [19] proposes the underpotential deposition of $Ag^0$ on certain faces, followed by CTAB binding, which serves to stabilize the faces, and allows gold reduction on other faces resulting in rod formation.

In this article, we present our experiences in synthesizing gold nanospheres and nanorods using slight modifications of the protocols discussed above. Our goal is to obtain nanorods whose aspect ratios can be tuned to obtain plasmon peaks between 650 nm–850 nm. Next, we conjugate the gold nanospheres and gold nanorods to the HER81 monoclonal antibody using electrostatic and hydrophobic interactions. The conjugation does not use modifications of the bilayer charge of nanorods nor does it use any linkers. We discuss various aspects of these protocols and postulate a possible mechanism for the bioconjugation of the antibody with the gold nanorods. We also discuss the feasibility of using these molecular probes for contrast enhancement of photoacoustic cancer imaging using simulations.

## 2. EXPERIMENTAL SECTION: MATERIALS AND METHODS

### 2.1. *Gold nanorods using the silver-assisted single surfactant growth method*

As mentioned earlier, the seed-mediated protocol requires the use of small gold nanospheres to seed growth solutions with silver nitrate as per the protocol of Nikoobakht and El-Sayed [17].

Table 1: Mean aspect ratios, lengths, widths, and longitudinal plasmon peaks for nanorods synthesized using the silver-assisted growth method.

| Sample | Volume of $AgNO_3$ ( $\mu$L) | Aspect ratio (R) | Length (nm) | Width (nm) | LP band (nm) |
|---|---|---|---|---|---|
| 1 | 50 | $2.3 \pm 0.3$ | $44.8 \pm 4.1$ | $19.8 \pm 2.9$ | 675 |
| 2 | 100 | $2.85 \pm 0.6$ | $45.1 \pm 5.5$ | $15.8 \pm 3.1$ | 764 |
| 3 | 150 | $3.0 \pm 0.6$ | $41.7 \pm 3.9$ | $13.9 \pm 2.3$ | 788 |
| 4 | 200 | $3.1 \pm 0.5$ | $52.0 \pm 4.6$ | $16.8 \pm 2.8$ | 831 |
| 5 | 250 | $3.6 \pm 0.6$ | $51.0 \pm 4.4$ | $14.1 \pm 2.1$ | 850 |

The following are the reagents used for the synthesis of the gold seed and gold nanorods.

Tetrachloroauric acid ($HAuCl_4 \cdot 3H_2O$) was purchased from Acros Organics (Belgium), hexadecyltrimethylammonium bromide (CTAB > 99%), sodium borohydride ($NaBH_4$, 99%), and ascorbic acid (99%) from Aldrich (The Netherlands) and silver nitrate ($AgNO_3$, 99.8%) from Merck (Germany). Prior to use, all glassware was cleaned with hydrofluoric acid (HF), further with aqua regia ($HCl/HNO_3$) and rinsed twice with deionized water.

*Gold seed of 3.5 nm diameter*

The synthesis was done using protocols of Nikoobakht and El-Sayed [17] with slight modifications. A solution of CTAB (5 mL; 0.2 M) was sonicated for 20 minutes at 40°C in a water bath. A solution of $HAuCl_4 \cdot 3H_2O$ (5 mL; 0.0005 M) was added with continuous stirring under inert conditions (nitrogen environment). Then, an ice-cold aqueous solution of $NaBH_4$ (0.6 mL; 0.01 M) was added at once with vigorous stirring for 1 minute. This seed solution (CTAB-capped) is further used during growth stage of nanorods.

*Gold nanorods of varying aspect ratios*

Five identical conical flasks containing 10 mL of a growth solution that consists of CTAB (5 mL; 0.2 M) and $HAuCl_4 \cdot 3H_2O$ (5 mL; 0.001 M) were prepared. The color of the growth solution is dark-yellow. $AgNO_3$ (50, 100, 150, 200, and 250 $\mu$L of 0.006 M) was added to the five identical growth solution flasks in an amount that was chosen so as to yield desired aspect ratios for the resulting nanorods. Following this, the mild reducing agent ascorbic acid (70 $\mu$L; 0.1 M) was added to each growth solution conical flask to give colorless solutions. Finally, 14 $\mu$L of preformed CTAB-capped seed solution was added to each conical flask, and mixtures were gently mixed. After 3 hours at 24°C, the nanorod suspension turned into a dark-blue solution with a brownish opalescence. These solutions were concentrated by centrifuging twice at 12000 g for 20 minutes which also enabled removal of the excess unbound CTAB. The centrifuged gold nanorods which are dispersed in water were stored at 4°C.

### 2.2. Characterization of gold nanoparticles

Electron microscopy of the NPs was performed using a CM 30 Philips transmission electron microscope (TEM) or a Zeiss-1550 high-resolution scanning electron microscope (HRSEM). Particle sizes were estimated using NI Vision module (Labview, National Instruments) on the digital SEM images with at least 250 particles considered in each case. Extinction spectra of NPs (and bioconjugated NPs) were measured using the Shimadzu PC3101 UV-Vis-NIR spectrophotometer.

The concentration of nanorods synthesized was estimated using the relation $A = cd\varepsilon$, where $A$ is the measured absorbance, $c$ the concentration in moles (M), $\varepsilon$ the molar extinction coefficient ( $M^{-1}cm^{-1}$), and $d$ the path length of the cuvette used to record the spectra. The derived molar extinction coefficients can be compared with $\varepsilon$ values from a recent report, estimated for a range of aspect ratios of nanorods by measuring the gold content in sols using inductively coupled plasma (ICP) atomic emission spectroscopy [19].

### 2.3. Bioconjugation of HER81 mAb to gold nanoparticles

Conjugation was achieved using combination of electrostatic and hydrophobic binding interactions. The particles chosen for bioconjugation were 25 nm citrate-capped gold spheres (Aurion, Wageningen, The Netherlands), and silver-assisted surfactant mediated gold nanorods with aspect ratios of approximately 2.85 (see Table 1) with the longitudinal plasmon peak at 764 nm. The anti-HER2 mouse monoclonal antibody (mAb) (Immunicon, USA) was chosen as the targeting moiety. The antibody designated as HER81 recognizes Human EGF receptor 2, HER2. HER2, also called erbB2, is a member of the epidermal growth factor receptor (EGFR) family and is overexpressed in 20–40% of human breast cancers [20].

In general, for optimum conjugation, it is recommended that the pH of the antibody and gold sol be maintained at or slightly higher than the isoelectric point (pI) of the antibody [21]. The isoelectric (pI) point of HER81 mAb was determined using the Pharmacia PhastSystem isoelectric focusing (IEF). The pH of the antibody was adjusted with dialysis in 5mM sodium acetate buffer and the pH of the colloidal gold was adjusted with 0.1 M KOH, to approximately 0.5 pH units above this value.

Next, the minimum protecting amount of antibody to be used for the conjugation is determined. This is the amount of protein that is required to maintain colloidal stability of the conjugated NPs upon addition of NaCl [21] as judged by colorimetric analysis; as long as the conjugated NPs turns blue, particle aggregation takes place implying that the amount of protein is not sufficient to stabilize the suspension. By trial, different amounts of antibody are added to samples of the

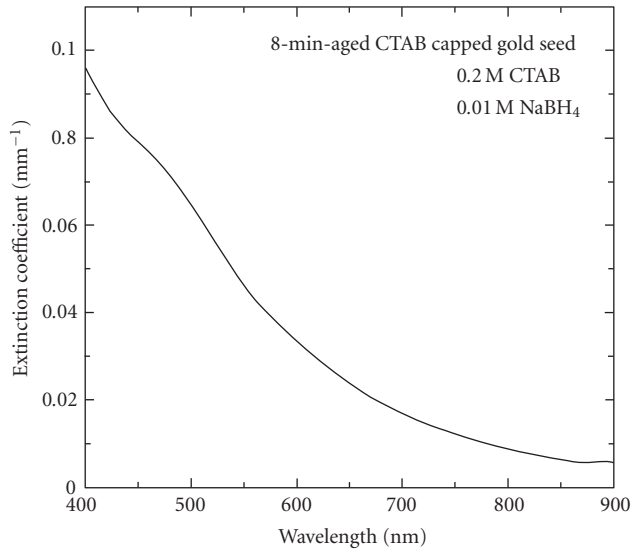


Figure 1: Optical extinction spectrum of preformed 8-minute-aged CTAB-capped gold nanospheres as seed for nanorod synthesis.

gold sol, gently mixed, and allowed to stand at room temperature for 2 minutes. Spectroscopic analysis reveals which sample remains stable; the minimum amount of protein added is then ascertained and is used for subsequent conjugation of the gold sol.

To block the free surfaces on the gold, 10% bovine serum albumin (BSA) in dialyzed buffer (sodium acetate), maintained at the same pH as the antibody solution, is used. The BSA was added to the conjugate to a final concentration of 1% and was allowed to incubate for 5 minutes. The resultant was then centrifuged for 30 minutes at 12000 g to remove excess protein and incompletely stabilized particles. The resulting pellet is dispersed in phosphate buffered saline (PBS) containing 1% BSA and stored at 4°C.

### 2.4. Cell culture and cell-bioconjugate incubation

The HER2 positive mammary adenocarcinoma (SKBR3) cell line was used as a positive cell line; Chinese hamster ovary (CHO) cells were used as an HER2 negative cell line. The cells were cultured in RPMI 1640 medium (Invitrogen) supplemented with glutamine, 10% FBS (Fetal Bovine Serum) with antibiotics. Cells were maintained in an incubator at 37°C and 5% $CO_2$.

The cells were detached from the tissue culture plate using trypsin. The cells were replated onto 12 mm glass cover slips in a 6-well tissue culture plate, and allowed to grow for 2 days at 37°C, 5% $CO_2$. When the cells grew to 80% confluence on the cover slips, the cells were rinsed with phosphate buffered saline (PBS) and fixed in 4% paraformaldehyde (PFA) for 15 minutes at room temperature.

### 2.5. Immunostaining and confocal microscopy

After fixation, immunostaining was performed on the cells. The cells were incubated with 100 $\mu$L of conjugated gold nanoparticles at a concentration of $9.7 \times 10^{10}$ particles per mL for 2 hours followed by silver enhancement performed using a silver-staining kit (Aurion, Wageningen, The Netherlands).

Confocal microscopy reflection images of the cells on cover slips were recorded on a Zeiss LSM 510 confocal laser scanning microscope using a C-Apochromat 63 X/1.4 numerical aperture (NA) water-immersion objective. An excitation wavelength of 543 nm was chosen and reflection images recorded using a 500–550 nm bandpass filter. All images were acquired with pinhole diameters of 178 $\mu$m. Care was taken to ensure that the excitation intensity as well as detector and amplifier gains were maintained at the same values for all images to facilitate comparison.

## 3. RESULTS

### 3.1. Synthesis of gold nanorods

We used seed particles within about 8 minutes of formation in the subsequent growth phase. The optical extinction spectrum of 8-minute-aged seed is shown in Figure 1.

Figure 2 shows the extinction spectrum and HR-SEM image of the nanorods synthesized using 50 $\mu$L $AgNO_3$ in the growth solution. The peak at 675 nm can be attributed to longitudinal plasmon resonance and the peak in the vicinity of 516.5 nm to transverse plasmon resonance.

Examination of the SEM image and determination of the mean sizes confirm that the NPs produced consist of monodisperse nanorods of aspect ratio of $2.3 \pm 0.3$, with a small number of large spheres; the latter's extinction peak coinciding with the transverse plasmon band of the nanorods. Figure 3 shows the extinction spectrum and the SEM image for the sample produced using 250 $\mu$L of silver nitrate. It is seen that the longitudinal plasmon band is shifted to 850 nm. Sizing from the SEM image yields an average aspect ratio of $3.6 \pm 0.6$. Figure 4 shows the size distribution of the 2 specimens.

The values of the molar extinction coefficient for the 2 cases above are $3.3 \pm 0.3 \times 10^9$ and $5.5 \pm 0.3 \times 10^9$ $M^{-1}cm^{-1}$ obtained by extrapolation of the data as reported in [19]. With this, we arrive at the concentration of the nanorods with peak at 675 nm as $4.3 \pm 0.3 \times 10^{11}$ NR/mL; for nanorods with the peak at 850 nm as $1.3 \pm 0.7 \times 10^{11}$ NR/mL.

Figure 5 shows the consolidated normalized extinction spectra of 5 nanorod solutions, having identical growth solutions with varying silver nitrate volumes. The spectra were normalized to the peak at 516 nm, which is due to a combination of the transverse plasmon resonance of the nanorods and the signature peak of gold nanospheres. It is seen that with higher silver nitrate volumes the extent of red-shifting increases [22]. The details of the observed changes in aspect ratios and plasmon bands are presented in Table 1.

### 3.2. Bioconjugation of gold nanospheres and gold nanorods

A signature for successful binding of protein to gold NPs is a red-shifted and amplitude reduced plasmon band. Both

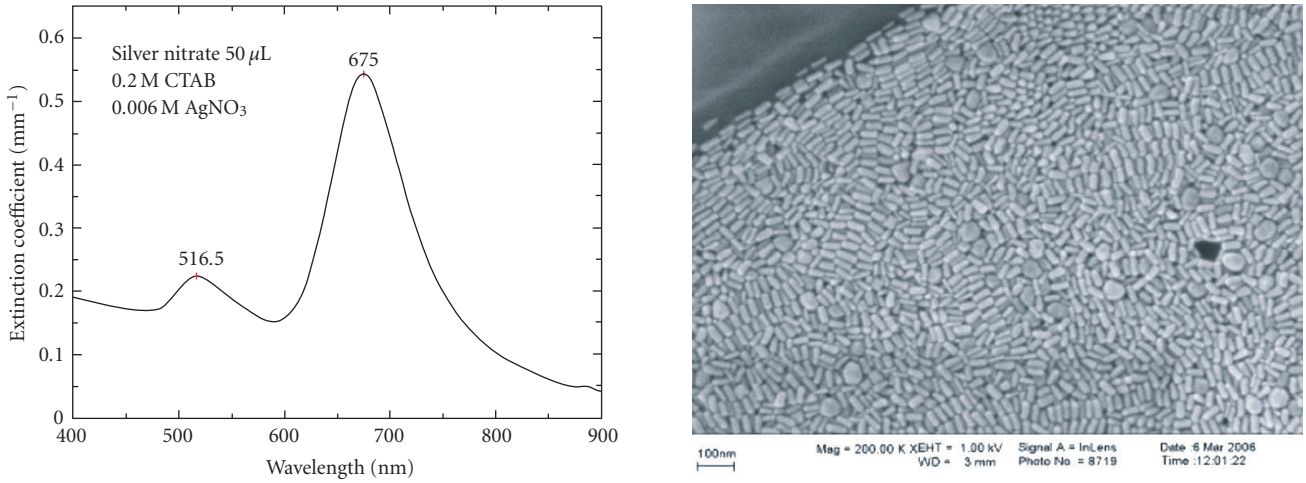


(a) (b)

Figure 2: Gold nanorods synthesized using 50 $\mu$L of silver nitrate in growth solution. (a) Optical extinction spectrum showing the transverse plasmon peak at 516.5 nm and the longitudinal plasmon peak at 675 nm. The amplitude of the longitudinal plasmon peak is higher than transverse plasmon peak which indicates the formation of high yield of nanorods compared to spheres. (b) High-resolution scanning electron microscope (SEM) image of gold nanorods showing high monodispersity. Few nanospheres are observed.

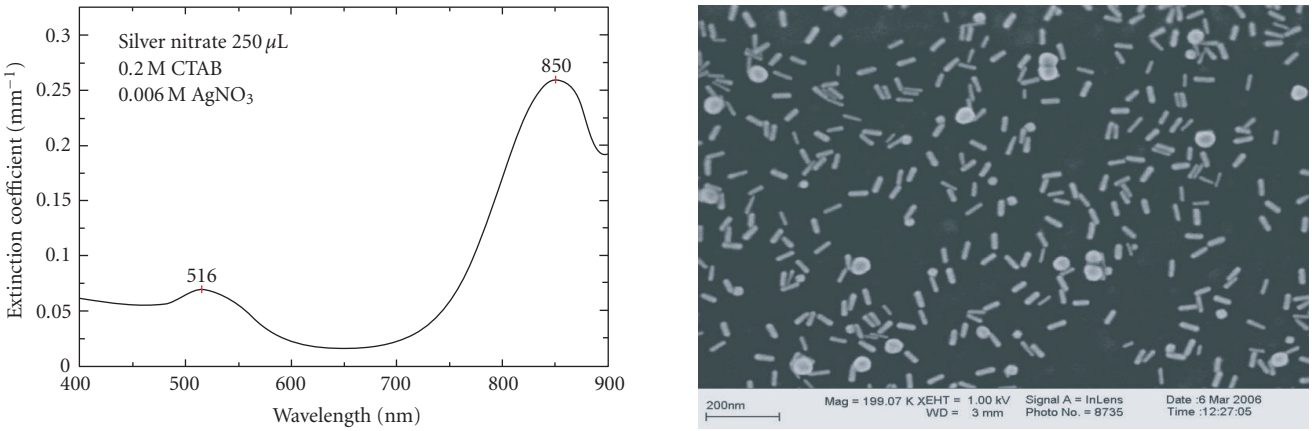


(a) (b)

Figure 3: Gold nanorods synthesized using 250 $\mu$L of silver nitrate in growth solution. (a) Optical extinction spectrum showing the transverse plasmon peak at 516 nm and the longitudinal plasmon peak at 850 nm. (b) High-resolution scanning electron microscope (SEM) image.

these effects are due to the formation of the inhomogeneous layer of protein on the gold particle surface that leads to the modification of refractive index of the embedding medium.

Figure 6(a) shows the extinction spectrum of gold nanospheres before and after incubation with HER81. Figure 6(b) is the corresponding situation with gold nanorods before and after incubation with the HER81 mAb. In both cases, the characteristic red-shift in the extinction peak of the plasmon bands is seen.

Not too much should be read into the amplitude changes of the extinction spectra since centrifugation of the bioconjugate to remove unbound protein, redispersion in water, and other procedures results in a change in the concentration of the NPs used for spectroscopy.

Figure 7(a) show confocal reflectance image (on left) and bright field image (on right) of the HER81 mAb/gold sphere conjugates incubated with SKBR3 cells. As discussed in the experimental section, silver enhancement was used by which silver is reduced onto the gold particles forming large clusters around 500 nm in size. This then enables visualization under the microscope. The HER2 receptors are localized to the cell membranes of SKBR3 cells. The high intensities in both images at the cell membrane are then evidence of the preservation of the functionality of the antibody and also illustrate successful conjugation. The images in Figure 7(b), which show the situation with the negative control using the CHO cells, display no such accumulation of gold particles. Also, adding nonantibody conjugated gold NPs to the SKBR3 cells did not result in accumulation of the nanorods, indicat-

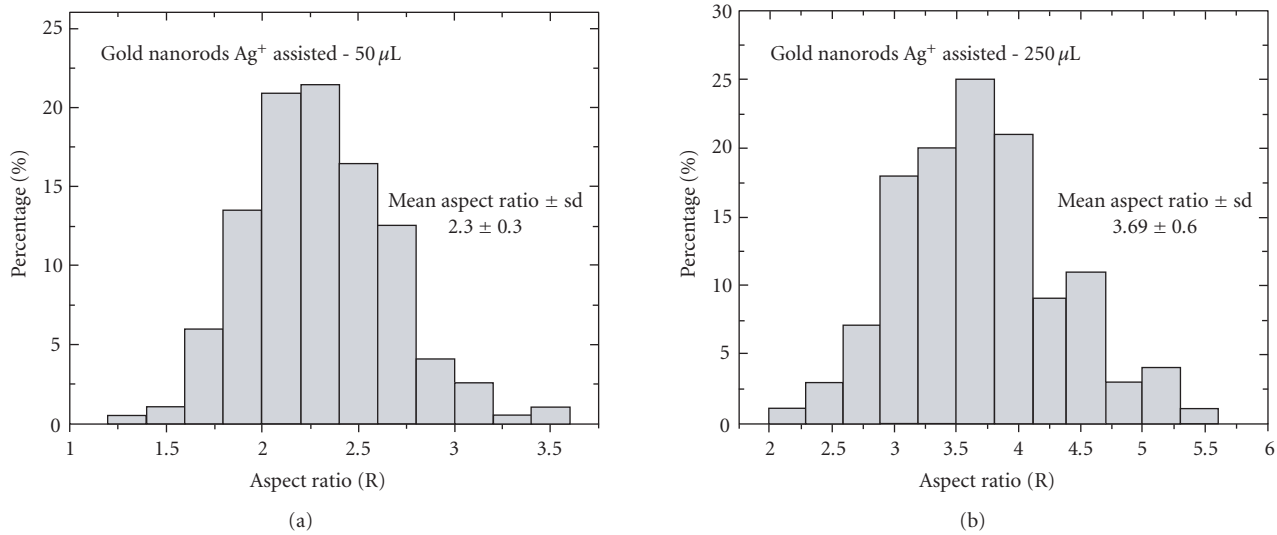


Figure 4: Histograms of gold nanorod aspect ratios synthesized with (a) 50 $\mu$L silver nitrate, mean aspect ratio of 2.3 ± 0.3 (mean length 44.8 ± 4.1 nm, mean width 19.8 ± 2.9 nm); and with (b) 250 $\mu$L silver nitrate, mean aspect ratio of 3.6 ± 0.6 (mean length 51.0 ± 4.4 nm, mean width 14.1 ± 2.1).

ing the specificity of the HER81 antibody-nanorod conjugate (data not shown).

Figures 8(a) and 8(b) are the results of the corresponding controls using the HER81 mAb/gold nanorods.

## 4. DISCUSSION

### 4.1. Gold nanorod synthesis

The end products of the seed-mediated growth protocols are crucially dependent on the nature of the seed, upon their size and upon the capping agents used. Additionally, the constituents and their concentrations in the growth solution influence the outcome of the synthesis products. The addition of silver ions in the growth solution and the use of preformed CTAB stabilized seed in the protocol of Nikoobakht and El-Sayed [17] produced not only a high yield of monodisperse nanorods but fine tunability of aspect ratios.

There are many unanswered questions regarding the mechanism of formation of gold nanorods using the silver-assisted protocol and this has been the topic of several studies [15, 17–19]. Recent reports of Orendorff and Murphy [19], and Liu and Guyot-Sionnest [23] provide some insights into the mechanisms that could be involved in the synthesis. It is postulated that silver ions are reduced by ascorbic acid even though it is a weak reducing agent, by the phenomenon of underpotential deposition (UPD). This is reduction of silver in monolayers on the growing gold nanorod surface at a potential less than the standard reduction potential [19]. The deposition is not uniform on the gold surface but occurs faster on the sidewalls compared with the end faces. Remarkably, the sidewalls in the case of nanorods produced with silver assistance using CTAB protected seed bear Au{110} faces, while the end faces have Au{100} faces. This is in contrast to the rods prepared by using citrate-capped seed without $Ag^+$. This faster passivation of the sidewalls is followed by CTAB

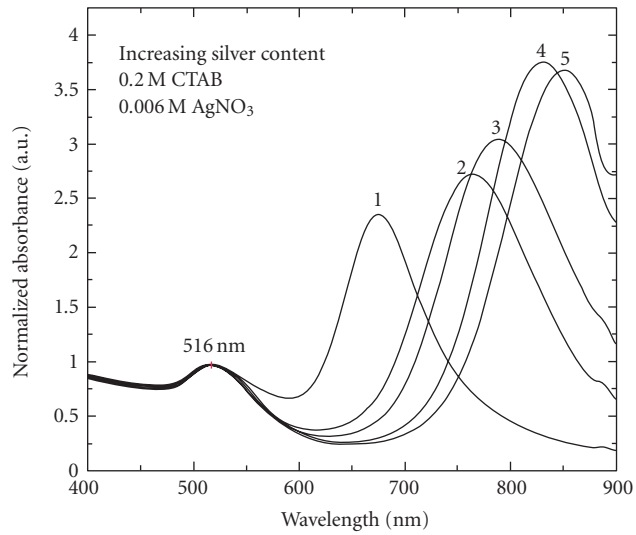


Figure 5: Normalized extinction spectra of gold nanorods with increasingly red-shifted longitudinal plasmon bands, synthesized using 50, 100, 150, 200, and 250 $\mu$L of silver nitrate in the growth solution for curves 1–5, respectively. Normalization of the spectra is done with respect to the transverse plasmon peak amplitudes.

binding possibly via bromide ions. This inhibits the reduction of gold, which deposits on the end faces. Ultimately, the end faces are also stabilized preventing the formation of very long nanorods. The model claims also to explain the increase in aspect ratio of the nanorods produced with higher concentration of silver ions used, by proposing that higher UPD of silver monolayers occur on the sidewalls which one assumes reducing the width of the nanorods thus increasing the aspect ratios [19].

Indeed, we observe some phenomena that are consistent with the above model. We are able to synthesize gold

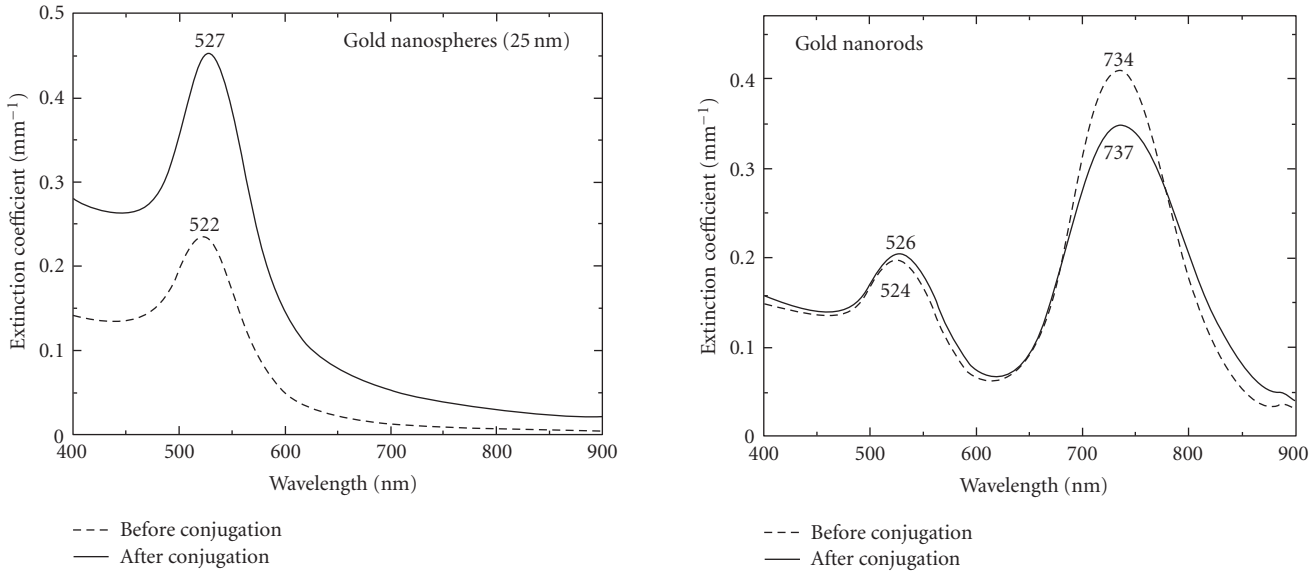


Figure 6: Extinction spectra before and after incubation of HER81 with (a) gold nanospheres, (b) gold nanorods. In both cases, a red shift in plasmon band(s) occurs after incubation with the antibody signifying successful bioconjugation.

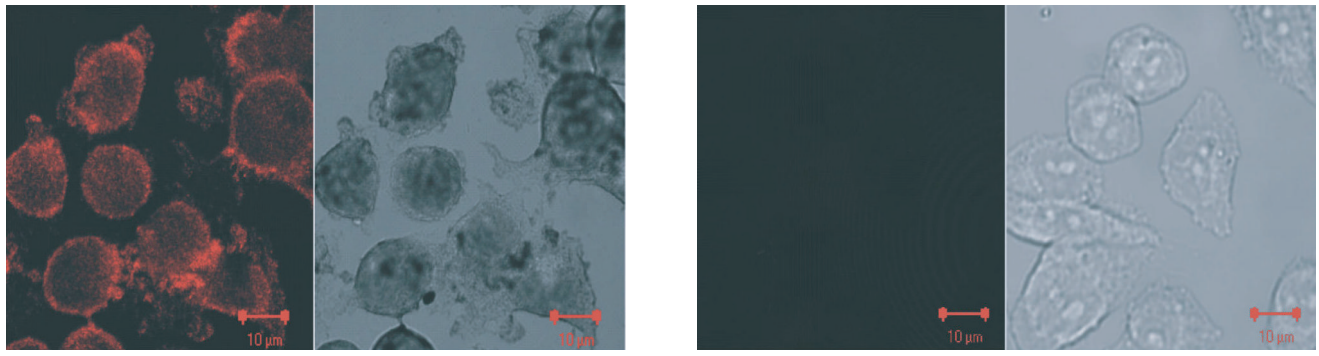


Figure 7: Confocal reflectance images (left) and bright field images (right) of (a) SKBR3 cells incubated with silver-stained HER81/gold sphere conjugates, (b) CHO cells under the same conditions. Care was taken to maintain the same acquisition parameters in both cases. The silver-stained bioconjugates are detected at the cell membranes of SKBR3 cells where HER2 is localized. This indicates successful conjugation and retention of functionality of the antibody after conjugation. No such accumulation of HER81/gold sphere conjugates is demonstrated in HER2 negative CHO cells.

nanorods only up to an aspect ratio of 3.6, as shown in Figure 3. Addition of higher volumes of silver nitrate produces no further increase in the aspect ratios of the particles. These particles have an average length of 51 nm. This supports the idea that ultimately complete passivation of the entire nanorod surface occurs preventing further gold deposition even though the reagents have not been exhausted. Further, we observe that nanorods that are made with increasing $Ag^+$ volumes have smaller diameters with the lengths practically unchanged or only slightly increasing (see Table 1). The above model can also explain this. It must be mentioned that the model does not have an appealing explanation regarding the ability to tune the aspect ratios so precisely by $Ag^+$ variation. It is very likely that the model will have to undergo refinements or even major changes before it is universally accepted.

### 4.2. *Gold nanoparticle—antibody conjugation*

The noncovalent conjugation of proteins to colloidal gold is usually due to a combination of electrostatic and hydrophobic interactions. Citrate-capped gold NPs are negatively charged due to a layer of negative citrate ions. Positively charged amino groups of the antibody will be attracted to the gold surface, and when the protein comes close enough for binding, the hydrophobic pockets of the protein will make contact and bind with the gold [24]. A general guideline to

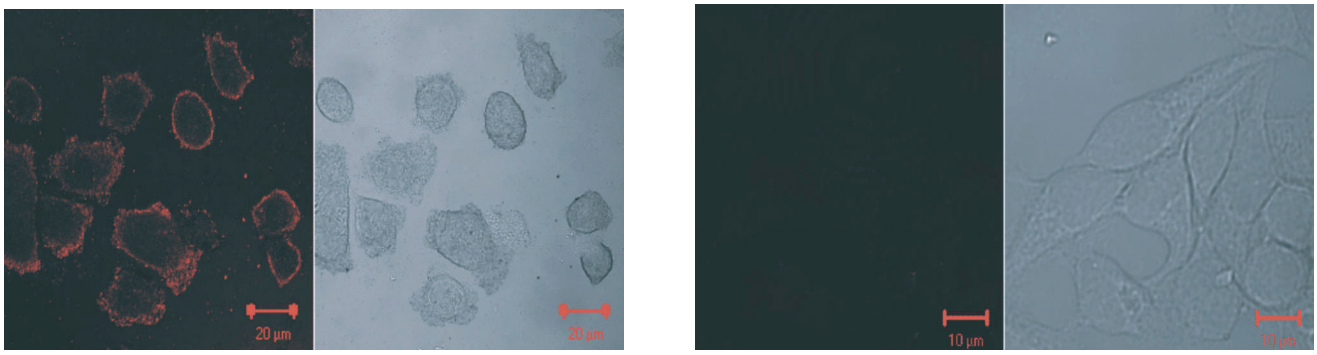


(a) (b)

Figure 8: Corresponding images as in Figure 7 for bioconjugates consisting of silver-stained HER81/gold nanorod conjugates incubated with (a) SKBR3 cells and (b) CHO cells. Care was taken to maintain the same acquisition parameters in both cases. The bioconjugates are accumulated at the cell membranes of SKBR3 cells where HER2 is localized. As expected, no such accumulation takes place in the case of HER2 negative CHO cells.

Table 2: Important optical imaging techniques that utilize absorption and scattering contrasts in biology and medicine.

| Technique | Imaging depth | Imaging resolution | Mechanism | Typical imaging applications |
|---|---|---|---|---|
| Confocal microscopy [1] | 500 $\mu$m | > 250 nm | Scattering /absorption | Tissue surfaces |
| Two-photon microscopy [2] | 800 $\mu$m | > 250 nm | Absorption | Tissue surfaces |
| Optical coherence tomography [3] | 2 mm | 1 $\mu$m | Scattering | Surfaces/subsurfaces of tissue |
| Diffuse optical tomography [4] | > 20 mm | $\approx$ 10 % depth | Scattering/absorption | Small animal; human breast and brain |
| Photoacoustic imaging [5] | > 20 mm | <1 mm (detector bandwidth limited) | Absorption | Subsurface to deep imaging; small animal; human breast |

optimize the bioconjugation is that the pH of the antibody and the gold sol must be maintained at or slightly above the isoelectric point of the antibody [24]. Following this, procedure for citrate-capped gold nanospheres with the HER81 antibody resulted in good bioconjugation as shown by the spectroscopy and bioactivity studies (Figure 7).

With nanorods, the situation is more complex as compared with nanospheres. The sidewalls of the nanorods are expected to be stabilized with a bilayer of CTAB, which imparts a positive charge to the gold. Huang et al. [25] first changed the positively charged surface to a negatively charged one by exposing the nanorods to poly(styrenesulfonate) PSS polyelectrolyte solution. The PSS-capped nanorods were then treated in the same way as in Section 2.3 with the conjugation being done with anti-EGFR monoclonal antibodies.

Zeta potentials of the gold nanorod solution as originally prepared were determined to be +55 mV. Centrifugation to remove the excess unbound CTAB and redispersion of the rods in water saw a reduction in the zeta potential to +7.5 mV, which also points to a low stability. We surmise that inspite of the net positive charge, the unpassivated end faces would be negatively charged due to the presence of $AuCl^{-2}$ ions [21]. We therefore performed the same protocol (as in Section 2.3) and found that the bioconjugation indeed was achieved as demonstrated by the red-shifted extinction spectra as seen in Figure 6. Further, confocal microscopy successfully detected the bioconjugates on the HER2 positive cell line (Figure 8), indicating the success of the conjugation.

We believe that the mechanism of conjugation is the same as that in the case of gold nanospheres that is electrostatic and hydrophobic physisorption. It is also likely that at the pH at which the antibody is maintained, the Fc fragment of the antibody that is rich in positively charged amino acids such as lysine will bind to the negatively charged chloride ion layer on the exposed end faces of the rods. We intend to perform studies that will elucidate this aspect. Further, we will perform the protocol of first capping the nanorods with PSS for example, and then comparing the antigen binding affinity constants of the bioconjugates from the two methods.

### 4.3. Potential contrast enhancing applications

The scattering and absorption bands of the synthesized nanorods span the wavelength regime between 675–850 nm that is of interest to optical imaging. This occupies the most important part of the "optical imaging window" where light penetration in tissue is high due to reduced scattering and absorption coefficients. Optical imaging techniques (Table 2) that rely on scattering and/or absorption contrast to detect pathological tissue could benefit from the use of such nanoparticles with or without targeting capability.

Our goal is to employ these particles as contrast agents for photoacoustic cancer imaging, which has been proposed earlier by Oraevsky and coworkers [26, 27]. Photoacoustic imaging relies on optical absorption for its signals. When photons are absorbed, nonradiative de-excitation of the absorbed optical energy takes place with the release of localized heat. The local thermal expansion that results produces pressure transients [5]. When illuminated with pulsed laser light, a tumor site by virtue of its higher absorption with respect to the healthy background tissue, due to angiogenesis [28], will act as a source of bipolar photoacoustic pulses. This ultrasound propagates with minimal distortion to the surface where it is detected using appropriate wideband detectors. The time-of-flight, amplitude, and peak-peak time of the bipolar PA pulse possess information regarding the location, absorption, and dimensions of the source, thereby permitting a reconstruction of the tumor site [29, 30].

It is known that the NIR optical absorption contrast of tumors versus healthy tissue, measured using optical mammographic methods, is between 1.5 and 3. Clinical trials of optical mammography are being conducted worldwide but at present, it seems implausible that intrinsic contrast alone will provide sufficient sensitivity and specificity, and targeted contrast enhancement is likely to be required [31]. Since the same contrast mechanism of optical absorption is operative in photoacoustic imaging as well, a similar conclusion may be anticipated.

An impression of the feasibility of using the nanorods synthesized for contrast enhancement is now discussed. The absorption cross-section of a nanorod at a wavelength, say 800 nm, is estimated using discrete dipole approximation (DDSCAT) simulations [32, 33] as $C_{\text{abs}} = 2.8 \times 10^{-14}\ \text{m}^2$. A typical average optical absorption coefficient for an invasive ductal carcinoma is $\mu_a = 0.008\ \text{mm}^{-1}$ at 800 nm. In order to achieve contrast enhancement, a certain number density of gold nanorods is required to exhibit higher absorption than the intrinsic value and may be calculated as

$$\rho_{\text{NR}} \geq \frac{\mu_a}{C_{\text{abs}}}. \tag{1}$$

This gives $\rho_{\text{NR}} = 2.8 \times 10^8\ \text{NR/cm}^3$. Further photoacoustic signals can be enhanced by a thermal nonlinearity mechanism to 3 orders of magnitude higher [34], then the modified number density of nanorods required is only $\rho_{\text{NR}} = 2.8 \times 10^5\ \text{NR/cm}^3$.

Published studies report that most tumour cell types express from $2\times10^4$ to $20\times10^4$ ErbB2 receptors/cell [12]. Let us assume arbitrarily that $2 \times 10^3$ of these sites per cell are occupied by conjugated nanorods. Further, if we assume that 1% of cells at a tumor site overexpress HER2 results in a figure of $2 \times 10^6$ cancer cells/cm$^3$. This will then lead to an estimation of the density of binding sites of the order of $10^9\ \text{cm}^{-3}$. Comparison of $\rho_{\text{NR}}$ and the estimated figure of density of binding sites leads us to believe that contrast enhancement will be possible.

We intend to test these molecular probes in small animal photoacoustic imaging. Contrast enhancement with untargeted PEG-coated nanoparticles will be studied. Accumulation of the contrast agent at the tumor site will depend on enhanced permeation and retention (EPR). Active targeted studies will follow, with conjugated nanoparticles administered to the animal via the tail vein. In all studies, emphasis will be on ascertaining the sensitivity/efficacy of the technique with and without contrast agent.

## 5. CONCLUSIONS

We have synthesized gold nanorods with optical extinction peaks in the region from 675–850 nm making these eminently suited for scattering and absorption contrast enhancements in optical imaging. We have performed bioconjugation of these nanorods with HER81 antibodies, which bind with high efficiency to HER2 receptors expressed by SKBR3 breast carcinoma cells. We demonstrated in fixed cell studies that the targeting functionality of the antibody moiety remains viable. However, it must be mentioned that the situation *in vivo* will be complex compared to the simplified situation *in vitro*. Other unresolved issues remain at present. One of these is regarding toxicity and cellular uptake of these particles *in vivo*. Further, whether these molecular probes will be able to extravasate into the tumor tissue through leaks in the vasculature has not yet been studied. These are some lines of research that we intend to follow in the near future.

## ACKNOWLEDGMENTS

We acknowledge fruitful discussions with Dr. Henk-Jan van Manen, Dr. Rolf Vermeij, and Dr. Christian Blum in various aspects related to bioconjugate chemistry, cell growth, and microscopy studies. The assistance of Sam Mathew (IIT Bombay) in early synthesis experiments is acknowledged. We thank Dr. Christina Graf (University of Wuerzburg) for discussions regarding the synthesis protocols. Peter van de Plas (Aurion, Wageningen, The Netherlands) is acknowledged for advice and tips on the use of bioconjugation protocols. We received the HER81 mAb and SKBR3 cells from Dr. Leon Terstappen and Dr. Arjan Tibbe (Immunicon). Electron Microscopy was carried out by Mark Smithers and Dr. Enrico Keim (CMAL/MESA$^+$). We thank Frank Roesthuis (LT/TNW) for the use of fume hoods in the clean room. The research is funded by the University of Twente through the thrust area program NIMTIK, and by the Nederlandse Wetenschappelijk Organisatie (NWO) and Stichting Technische Wetenschappen (STW) through project TTF 6527. Simulations of optical properties of particles were performed using supercomputing facilities of the National Computing Facilities Foundation (NCF) supported by the NWO.

## REFERENCES

[1] J. A. Conchello and J. W. Lichtman, "Optical sectioning microscopy," *Nature Methods*, vol. 2, no. 12, pp. 920–931, 2005.

[2] F. Helmchen and W. Denk, "Deep tissue two-photon microscopy," *Nature Methods*, vol. 2, no. 12, pp. 932–940, 2005.

[3] J. G. Fujimoto, "Optical coherence tomography for ultrahigh resolution in vivo imaging," *Nature Biotechnology*, vol. 21, no. 11, pp. 1361–1367, 2003.

[4] D. A. Boas, D. H. Brooks, E. L. Miller, et al., "Imaging the body with diffuse optical tomography," *IEEE Signal Processing Magazine*, vol. 18, no. 6, pp. 57–75, 2001.

[5] M. Xu and L. V. Wang, "Photoacoustic imaging in biomedicine," *Review of Scientific Instruments*, vol. 77, no. 4, Article ID 041101, 22 pages, 2006.

[6] R. Richards-Kortum and E. Sevick-Muraca, "Quantitative optical spectroscopy for tissue diagnosis," *Annual Review of Physical Chemistry*, vol. 47, pp. 555–606, 1996.

[7] B. J. Tromberg, N. Shah, R. Lanning, et al., "Non-invasive in vivo characterization of breast tumours using photon migration spectroscopy," *Neoplasia*, vol. 2, no. 1-2, pp. 26–40, 2000.

[8] K. Licha, "Contrast agents for optical imaging," in *Contrast Agents II: Optical, Ultrasound, X-Ray and Radiopharmaceutical Imaging*, vol. 222 of *Topics in Current Chemistry*, chapter 2.1, pp. 1–29, Springer, Berlin, Germany, 2002.

[9] X. Intes, J. Ripoll, Y. Chen, S. Nioka, A. G. Yodh, and B. Chance, "In vivo continuous-wave optical breast imaging enhanced with indocyanine green," *Medical Physics*, vol. 30, no. 6, pp. 1039–1047, 2003.

[10] A. W. H. Lin, N. A. Lewinski, J. L. West, N. J. Halas, and R. A. Drezek, "Optically tunable nanoparticle contrast agents for early cancer detection: model-based analysis of gold nanoshells," *Journal of Biomedical Optics*, vol. 10, no. 6, Article ID 064035, 10 pages, 2005.

[11] J. Perez-Juste, I. Pastoriza-Santos, L. Liz-Marzan, and P. Mulvaney, "Gold Nanorods: Synthesis, Characterization and Applications," *Coordination Chemistry Reviews*, vol. 249, pp. 1870–1901, 2005.

[12] K. Sokolov, M. Follen, J. Aaron, et al., "Real-time vital optical imaging of precancer using anti-epidermal growth factor receptor antibodies conjugated to gold nanoparticles," *Cancer Research*, vol. 63, no. 9, pp. 1999–2004, 2003.

[13] D. A. Stuart, A. J. Haes, C. R. Yonzon, E. M. Hicks, and R. P. Van Duyne, "Biological applications of localised surface plasmonic phenomenae," *IEE Proceedings Nanobiotechnology*, vol. 152, no. 1, pp. 13–32, 2005.

[14] A. Gole and C. J. Murphy, "Seed-mediated synthesis of gold nanorods: role of the size and nature of the seed," *Chemistry of Materials*, vol. 16, no. 19, pp. 3633–3640, 2004.

[15] C. J. Murphy, T. K. Sau, A. M. Gole, et al., "Anisotropic metal nanoparticles: synthesis, assembly, and optical applications," *Journal of Physical Chemistry B*, vol. 109, no. 29, pp. 13857–13870, 2005.

[16] N. R. Jana, L. Gearheart, and C. J. Murphy, "Seed-mediated growth approach for shape-controlled synthesis of spheroidal and rod-like gold nanoparticles using a surfactant template," *Advanced Materials*, vol. 13, no. 18, pp. 1389–1393, 2001.

[17] B. Nikoobakht and M. A. El-Sayed, "Preparation and growth mechanism of gold nanorods (NRs) using seed-mediated growth method," *Chemistry of Materials*, vol. 15, no. 10, pp. 1957–1962, 2003.

[18] T. K. Sau and C. J. Murphy, "Seeded high yield synthesis of short au nanorods in aqueous solution," *Langmuir*, vol. 20, no. 15, pp. 6414–6420, 2004.

[19] C. J. Orendorff and C. J. Murphy, "Quantitation of metal content in the silver-assisted growth of gold nanorods," *Journal of Physical Chemistry B*, vol. 110, no. 9, pp. 3990–3994, 2006.

[20] D. J. Slamon, G. M. Clark, S. G. Wong, W. J. Levin, A. Ullrich, and W. L. McGuire, "Human breast cancer: correlation of relapse and survival with amplification of the HER-2/neu oncogene," *Science*, vol. 235, no. 4785, pp. 177–182, 1987.

[21] D. A. Handley, "Methods for synthesis of colloidal gold," in *Colloidal Gold: Principles, Methods, and Applications*, pp. 13–32, Academic Press, New York, NY, USA, 1989.

[22] B. Nikoobakht and M. A. El-Sayed, "Evidence for bilayer assembly of cationic surfactants on the surface of gold nanorods," *Langmuir*, vol. 17, no. 20, pp. 6368–6374, 2001.

[23] M. Liu and P. Guyot-Sionnest, "Mechanism of silver(I)-assisted growth of gold nanorods and bipyramids," *Journal of Physical Chemistry B*, vol. 109, no. 47, pp. 22192–22200, 2005.

[24] G. T. Hermanson, "Preparation of colloidal-gold-labeled proteins," in *Bioconjugate Techniques*, pp. 593–605, Academic Press, New York, NY, USA, 1996.

[25] X. Huang, I. H. El-Sayed, and M. A. El-Sayed, "Cancer cell imaging and photothermal therapy in the near-infrared region by using gold nanorods," *Journal of the American Chemical Society*, vol. 128, no. 6, pp. 2115–2120, 2006.

[26] J. A. Copland, M. Eghtedari, V. L. Popov, et al., "Bioconjugated gold nanoparticles as a molecular based contrast agent: implications for imaging of deep tumors using optoacoustic tomography," *Molecular Imaging and Biology*, vol. 6, no. 5, pp. 341–349, 2004.

[27] M. Eghtedari, M. Motamedi, V. L. Popov, N. A. Kotov, and A. A. Oraevsky, "Optoacoustic imaging of gold nanoparticles targeted to breast cancer cells," in *Photons Plus Ultrasound: Imaging and Sensing*, vol. 5320 of *Proceedings of the SPIE*, pp. 21–28, San Jose, Calif, USA, January 2004.

[28] P. Carmeliet and R. K. Jain, "Angiogenesis in cancer and other diseases," *Nature*, vol. 407, no. 6801, pp. 249–257, 2000.

[29] S. Manohar, A. Kharine, J. C. G. van Hespen, W. Steenbergen, and T. G. van Leeuwen, "Photoacoustic mammography laboratory prototype: imaging of breast tissue phantoms," *Journal of Biomedical Optics*, vol. 9, no. 6, pp. 1172–1181, 2004.

[30] S. Manohar, A. Kharine, J. C. G. van Hespen, W. Steenbergen, and T. G. van Leeuwen, "The Twente Photoacoustic Mammoscope: system overview and performance," *Physics in Medicine and Biology*, vol. 50, no. 11, pp. 2543–2557, 2005.

[31] H. Rinneberg, D. Grosenick, K. T. Moesta, et al., "Scanning time-domain optical mammography: detection and characterization of breast tumors in vivo," *Technology in Cancer Research and Treatment*, vol. 4, no. 5, pp. 483–496, 2005.

[32] B. T. Draine and P. J. Flatau, "User Guide for the Discrete Dipole Approximation Code DDSCAT.6.1," http://arxiv.org/abs/astro-ph/0409262.

[33] B. T. Draine and P. J. Flatau, "Discrete-dipole approximation for scattering calculations," *Journal of the Optical Society of America*, vol. 11, no. 4, pp. 1491–1499, 1994.

[34] I. G. Calasso, W. Craig, and G. J. Diebold, "Photoacoustic point source," *Physical Review Letters*, vol. 86, no. 16, pp. 3550–3553, 2001.

Hindawi Publishing Corporation
International Journal of Biomedical Imaging
Volume 2007, Article ID 49791, 5 pages
doi:10.1155/2007/49791

*Research Article*

# In Vivo Evaluation of the Nitroimidazole-Based Thioflavin-T Derivatives as Cerebral Ischemia Markers

**Taiwei Chu, Zejun Li, Xinqi Liu, and Xiangyun Wang**

*Bejing National Laboratory for Molecular Sciences (BNLMS), Department of Applied Chemistry, College of Chemistry and Molecular Engineering, Peking University, Beijing 100871, China*

Received 10 April 2007; Accepted 5 July 2007

Recommended by Wei Liang

Timely imaging and accurate interpretation of cerebral ischemia are required to identify patients who might benefit from more aggressive therapy, and nuclear medicine offers a noninvasive method for demonstrating cerebral ischemia. Three nitroimidazole-based thioflavin-T derivatives, *N*-[4-(benzothiazol-2-yl)phenyl]-3-(4-nitroimidazole-1-yl) propanamide (4NPBTA), *N*-[4-(benzothiazol-2-yl)phenyl]-3-(4-nitroimidazole-1-yl)-*N*-methylpropanamide (4NPBTA-1), and *N*-[4-(benzothiazol-2-yl)phenyl]-3-(2-nitroimidazole-1-yl) propanamide (2NPBTA), were radioiodinated and evaluated as possible cerebral ischemia markers. In normal mice, these compounds showed good permeation of the intact blood-brain barrier (BBB), high initial brain uptake, and rapid washout. In gerbil stroke models that had been subjected to right common carotid artery ligation to produce cerebral ischemia, [$^{131}$I]2NPBTA, uptake in the right cerebral hemisphere decreased more slowly than that of the left, and the right/left hemisphere uptake ratios increased with time. Also, the right/left hemisphere uptake ratios correlated positively with the severity of the stroke. The results showed that [$^{131}$I]2NPBTA had a specific location in the cerebral ischemic tissue. This represented a first step in finding new drugs and might provide a possible cerebral ischemic marker.



## 1. INTRODUCTION

Stroke is the third cause of mortality and the first cause of disability in adults [1, 2]. As cerebral ischemia cannot be predicted, timely imaging and accurate interpretation are required to identify patients who might benefit from more aggressive therapy. Although computed tomography (CT) and magnetic resonance imaging (MRI) have been important and widely used clinical imaging techniques, there are some shortcomings in the imaging of acute stroke, such as the limited brain coverage. Nuclear medicine offers a noninvasive method for demonstrating cerebral ischemia. However, up to now, the markers of cerebral ischemia were scarce [2, 3].

The ideal cerebral ischemia markers should not only permeate across the BBB but also accumulate in the brain ischemia. Recently, Mathis et al. synthesized a series of thioflavin-T derivatives, which had the "benzothiazole-aniline" backbone and showed good permeation across the BBB [4–6]. Also it is well known that the nitroimidazole derivatives can selectively accumulate in hypoxic tissue and be used to image tumor hypoxia [7–9] and cerebral ischemia [10, 11]. In our previous study, three nitroimidazole-based thioflavin-T derivatives were synthesized and radiolabeled with iodine-131 (see Figure 1): *N*-[4-(benzothiazol-2-yl)-phenyl]-3-(2-nitroimidazole-1-yl) propanamide (2NPBTA), *N*-[4-(benzothiazol-2-yl)phenyl]-3-(4-nitroimidazole-1-yl)-propanamide (4NPBTA), and *N*-[4-(benzothiazol-2-yl) phenyl]-3-(4-nitroimidazole-1-yl)-*N*-methylpropanamide (4NPBTA-1). In vitro and in vivo results showed that they could bind to viable hypoxic tumor cells [12]. In this paper, their permeability across the BBB into the normal brain and *in vivo* evaluation in the gerbil cerebral ischemia models were investigated.

## 2. MATERIALS AND METHODS

No-carrier-added Na[$^{131}$I] (aqueous solution) was obtained from China Institute of Atomic Energy. 2NPBTA, 4NPBTA, and 4NPBTA-1 were synthesized and radiolabeled with iodine-131 in our laboratory [12].

Kunming mice were obtained from Breeding Center of the Institute of Zoology and adult Mongolian gerbils from Breeding Center of Capital University of Medical Sciences.

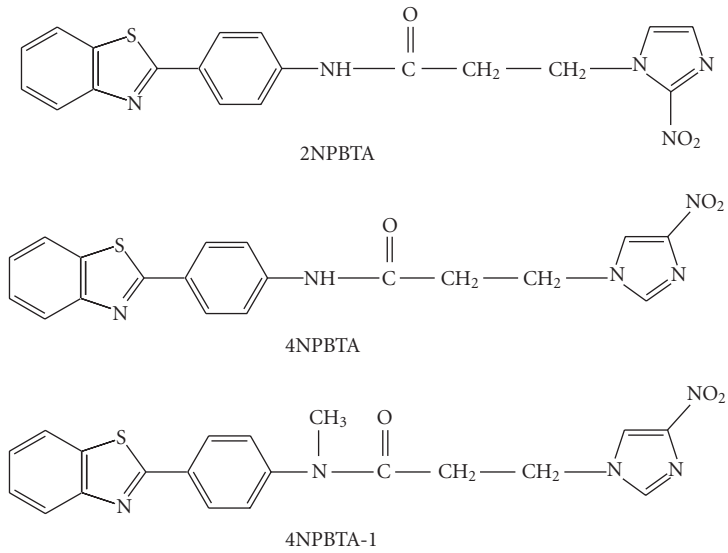


Figure 1: Structures of [$^{131}$I]2NPBTA, [$^{131}$I]4NPBTA, and [$^{131}$I]4NPBTA-1.

All experiments were carried out following the principles of laboratory animal care and the China law on the protection of animals. Radioactivity in the brain of the animals was assayed using a Cobra II series auto-gamma counting system (Packard).

### 2.1. Brain uptake and clearance in normal mice

Brain uptake and clearance were performed using normal Kunming mice (males, ∼20 g). Each mouse received a 0.1 mL (2 $\mu$Ci, MBq) dose of [$^{131}$I]2NPBTA, [$^{131}$I]4NPBTA, or [$^{131}$I]4NPBTA-1 by tail vein injection. Such injection solution (0.1 mL) was taken as standard for calculating the percent injected dose per gram of tissue, that is, %ID/g. At 2 and 30 minutes postinjection, mice were killed without anesthesia by cervical dislocation in groups of five. The brain was removed, weighed, and counted. The brain uptake (the percent injected dose per gram of tissue, %ID/g) was calculated. The 2-to-30 minutes ratios of %ID/g of the brain were calculated. The final results were expressed as mean ± standard deviation (SD).

### 2.2. Evaluation in gerbil cerebral ischemia models

Adult Mongolian gerbils (males, ∼100 g) were used for cerebral ischemia models. A right common carotid artery ligation was performed to produce cerebral hypoxia-ischemia (HI) as initially described by Levine and Payan [13]. Gerbils were anesthetized intraperitoneally (i.p.) with 3.5% chloral hydrate (1 mL), and the four limbs were fixed. A midline anterior incision was made, the right common carotid artery was isolated and ligated with 6–0 surgical sutures distally and proximally. Then the vessel was transected to assure no flow. Thereafter, the incision was closed, and the gerbils were allowed to awake. Gerbils were ranked by the modified stroke index (SI) described by Ohno et al. [14]. Gerbils with total stroke indices of >10 were used for injection. [$^{131}$I]2NPBTA, [$^{131}$I]4NPBTA, or [$^{131}$I]4NPBTA-1 (0.5 mL, 10 $\mu$Ci, MBq) was injected i.p. into the gerbils. Such injection solution (0.5 mL) was taken as standard for calculating the percent injected dose per gram of tissue, that is, %ID/g. Then, animals were housed in controled animal facilities. They were given food and water *ad libitum*. The gerbils were sacrificed without anesthesia by cervical dislocation in groups of three at 4, 8, and 12 houers after injection. The whole brain was removed, placed on dry ice for about 2 minutes, and then cut in half along the cerebral longitudinal fissure. The right and left halves were weighed and radioactivity counted. The %ID/g was determined for the right and left hemispheres. The right/left hemispheral uptake ratios, that is, the ratios of ischemic brain to normal brain, were also calculated. The final results were expressed as mean ± standard deviation (SD). The observed significance level ($P$ value) was determined using Student's t-test.

### 2.3. Evaluation of 2NPBTA following repetitive administration

[$^{131}$I]2NPBTA (0.1 mL, 2 $\mu$Ci) was injected intraperitoneally (i.p.) into the gerbils subjected to right common carotid artery ligation at 0, 60, 120, 180, and 240 minutes. Such injection solution (0.1 mL) was taken as standard for calculating the percent injected dose per gram of tissue, that is, %ID/g. Before sacrifice, the stroke index was determined. Gerbils were sacrificed (no anesthesia) by cervical dislocation 120 minutes after the final injection. The whole brain was removed, blotted free of excess blood, placed on dry ice for about 2 minutes, and then sliced coronally at approximately 3-mm intervals, yielding a total of five coronal slices, designated A–E, from rostral to caudal ends. Each slice was then cut in half at the midsagittal plane, and the right and left

Table 1: Brain uptake and clearance.

| Compound | 2 min (ID%/g) | 30 min (ID%/g) | Ratio of 2-to-30 min |
|---|---|---|---|
| [$^{131}$I]2NPBTA | 2.93±0.39 | 0.47±0.11 | 6.2 |
| [$^{131}$I]4NPBTA | 2.90±0.31 | 0.30±0.10 | 9.7 |
| [$^{131}$I]4NPBTA-1 | 3.31±0.50 | 0.61±0.16 | 5.4 |

Table 2: Uptake in the gerbil ischemic and normal brain hemisphere (%ID/g).

| Brain | [$^{131}$I]2NPBTA | | | [$^{131}$I]4NPBTA | | | [$^{131}$I]4NPBTA-1 | | |
|---|---|---|---|---|---|---|---|---|---|
| | 4 h | 8 h | 12 h | 4 h | 8 h | 12 h | 4 h | 8 h | 12 h |
| Right | 0.042±0.005 | 0.034±0.006 | 0.025±0.004* | 0.046±0.006 | 0.022±0.001 | 0.020±0.004 | 0.040±0.008 | 0.017±0.001 | 0.015±0.002 |
| Left | 0.036±0.004 | 0.025±0.003 | 0.014±0.002 | 0.038±0.001 | 0.018±0.005 | 0.016±0.003 | 0.034±0.010 | 0.013±0.002 | 0.012±0.002 |
| Right/Left | 1.18±0.13 | 1.39±0.10(**) | 1.76±0.10(***) | 1.22±0.16 | 1.28±0.28(**) | 1.24±0.03(**) | 1.18±0.02 | 1.26±0.28(**) | 1.27±0.13(**) |

Each value is mean ± SD
(*) .05 > $P$ value > .01 as compared with left brain.
(**) $P$ value > .05 as compared with 4 hours.
(***) $P$ value < .01 as compared with 4 hours.

halves were weighed and radioactivity counted. The %ID/g of all brain slices was determined.

## 3. RESULTS

### 3.1. Normal brain uptake and clearance

High brain uptake and low nonspecific binding, as measured by the ratio of brain uptake at 2 and 30 minutes, will generally improve the quality of brain tomographic studies [5]. It can be seen from Table 1 that the brain uptake of the three compounds was high at 2 minutes, and low binding at 30 minutes. As a result, the ratio of brain uptake at 2 and 30 minutes for [$^{131}$I]2NPBTA, [$^{131}$I]4NPBTA, and [$^{131}$I]4NPBTA-1 reached 6.2, 9.7, and 5.4, correspondingly. Thus, these compounds showed not only good permeation across the BBB into the brain at the early stage postinjection but also fast clearance from the normal brain tissue soon, making them worthy of further study as brain ischemia markers.

### 3.2. Uptake in ischemic and normal brain hemisphere of gerbil

The uptake of [$^{131}$I]2NPBTA, [$^{131}$I]4NPBTA, and [$^{131}$I]4NPBTA-1 in the ischemic brain hemisphere (right) and normal brain hemisphere (left) at 4, 8, and 12 hours after administration is presented in Table 2. The right/left (ischemic/normal) hemispheral uptake ratios were also calculated. The uptake in the right hemisphere was higher than that in the left at 4, 8, and 12 hours postinjection for [$^{131}$I]2NPBTA. This indicated that the clearance from ischemic brain tissue was slower than that from normal brain tissue. This was attributed to the selective accumulation of 2-nitroimidazole in hypoxic or ischemic conditions [15, 16]. The right/left uptake ratios, that is, the uptake ratios of ischemic to normal brain tissues were gradually increasing for [$^{131}$I]2NPBTA, from 1.18 at 4 hours to 1.76 at 12 hours. Similar to the finding of Read et al. that 30% of penumbral tissue of ischemic stroke was present at an average of approximately 20 hours using the hypoxia marker $^{18}$F-labeled fluoromisonidazole [17], the time for [$^{131}$I]2NPBTA was over 12 hours or even longer. As for [$^{131}$I]2NPBTA, the difference between the uptake of the right hemisphere and the left hemisphere was significant (.05 > $P$ > .01) at 12 hours, and the difference of the right/left uptake ratios between 12 hours and 4 hours was very significant ($P$ < .01).

Unfortunately, as for [$^{131}$I]4NPBTA and [$^{131}$I]4NPBTA-1, the differences between ischemic and normal brain tissues were not significant among all groups ($P$ > .05).

### 3.3. Uptake of [$^{131}$I]2NPBTA following repetitive administration

Figure 2 shows the uptake of [$^{131}$I]2NPBTA in coronal brain slices from 4 gerbils subjected to right common carotid ligation after multiple injections. Uptake was measured 2 hours after the last injection. The brain of each gerbil was divided into five 3-mm coronal sections, designated A–E, from rostral to caudal ends. The stroke indices ranging from 0 to 13 were indicated above the histograms for each animal. Increased uptake of [$^{131}$I]2NPBTA in ischemic hemispheres was found. The right/left hemisphere uptake ratios were 1.1, 0.9, 0.9, 1.1, and 0.9 from A to E for stroke index = 0 and 1.2, 1.2, 1.1, 1.3, 1.1 for stroke index = 4. For stroke indices = 11 and 13, they were 1.5, 2.0, 1.8, 1.7, 1.5 and 1.3, 2.4, 2.2, 2.0, 1.4. In the gerbil with no evidence of ischemia (stroke index 0), there was no evident right/left difference in any coronal sections. In the gerbil with a stroke index of 4, there was slight right/left difference. The gerbils with markedly symptomatic ischemia (stroke indices 11 or 13) showed a 2-fold

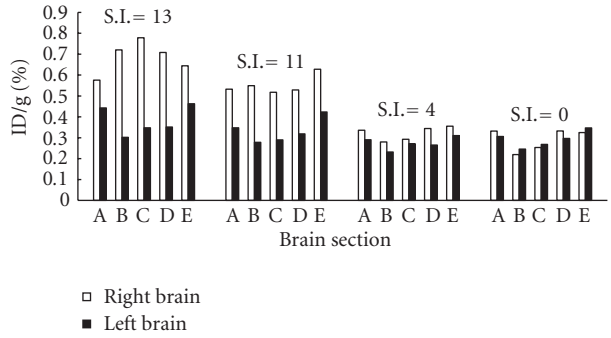


FIGURE 2: The uptake of [$^{131}$I]2NPBTA in coronal brain slices (designated A, B, C, D, E from rostral to caudal ends) from 4 gerbils subjected to right common carotid ligation after repetitive administration. The coronal slices stroke index (SI) was indicated above the histograms.

or 2.4-fold higher uptake in the midparietal region of the right hemisphere compared with the left. This confirmed that there was greater uptake of [$^{131}$I]2NPBTA in the right hemisphere compared with the left and verified that there was a trend for increased uptake with increasing stroke index. Our data supported the result reported by Hoffman et al. through the study of [$^{3}$H]misonidazole [10] that the right/left hemisphere uptake ratios correlated positively with the severity of the stroke.

For the gerbils with stroke index 11 or 13, the right/left hemisphere uptake ratios were modest at the most anterior coronal sections, that is, section A, the rostral end. The unique anterior circulation of gerbil cerebral vessels may explain this. The two anterior cerebral arteries of the gerbils fuse in the interhemispheric fissure to form a single pericallosal artery [18–20]. Ischemia may be developed in the anterior brain regions on the nonligated side following the loss of the contributing anterior cerebral flow from the opposite internal carotid circulation [10]. Thus, the rostral end of the left brain of the most symptomatic gerbil also showed an increase in uptake, compared with the corresponding coronal section in gerbil with very low stroke index. The gerbil has an incomplete circle of Willis and, after carotid ligation, may develop severe ischemia in the forebrain. The cerebellum and brain stem, which are supplied by the vertebral arteries, are included in the posterior sections of the brain. They are not ischemic after carotid ligation. Thus, the right/left difference was also modest at the caudal end, that is, the section E, and the coronal brain sections consistently showed a decreasing rostal-to-caudal binding of [$^{131}$I]2NPBTA, from B to E. Different from the result of Hoffman et al. [10] that there was no difference between right and left at the caudal ends, ours also showed difference at slice E, they were 1.5 fold and 1.4 fold for stroke indices = 11 and 13.

## 4. DISCUSSION

The unique anatomical feature of the gerbil made them widely used as a model in global ischemia [18, 19, 21]. Unlike rats, gerbils do not have a posterior communicating artery, that is, the circle of Willis is incomplete and there is incomplete anastomosis of the anterior cerebral arteries. Therefore, the blood supply of each hemisphere is isolated from the contralateral carotid and basilar arteries. Thus, global cerebral ischemia in gerbils can be induced by bilateral common carotid artery occlusion or unilateral common carotid occlusion. Ligation of one carotid artery causes ischemia in the ipsilateral hemisphere, while the other side is unaffected, providing neighboring normal tissue as an internal control. Many investigators have demonstrated that unilateral carotid occulation produces homolateral ischemia and/or infarction in approximately 30–50% of adult male gerbils [18–20].

This study indicated that [$^{131}$I]2NPBTA, [$^{131}$I]4NPBTA, and [$^{131}$I]4NPBTA-1 showed good permeation across the BBB into the brain and fast washout from the normal brain tissue. This study also demonstrated a specific location of [$^{131}$I]2NPBTA in the cerebral ischemic tissue. These results represented a first step toward cerebral ischemia markers of 2NPBTA and made it worthy of further investigation.

## ACKNOWLEDGMENTS

This work was supported by the National Basic Research Program (2006CB705700) from the Ministry of Science and Technology of China, and Grant no. 20301001 from the National Natural Science Foundation of China, Grant no. 7052015 from the Beijing Natural Science Foundation. The assistance of Dr. Weihong Cong and Professor Jianxun Liu, Xiyuan Hospital, China Academy of Traditional Chinese Medicine in the producing of the gerbil cerebral ischemia models is gratefully acknowledged.

## REFERENCES

[1] G. W. Petty, R. D. Brown Jr., J. P. Whisnant, J. D. Sicks, W. M. O'Fallon, and D. O. Wiebers, "Ischemic stroke subtypes: a population-based study of functional outcome, survival, and recurrence," *Stroke*, vol. 31, no. 5, pp. 1062–1068, 2000.

[2] N. J. Beauchamp Jr., P. B. Barker, P. Y. Wang, and P. C. M. vanZijl, "Imaging of acute cerebral ischemia," *Radiology*, vol. 212, no. 2, pp. 307–324, 1999.

[3] J. V. Guadagno, G. A. Donnan, R. Markus, J. H. Gillard, and J.-C. Baron, "Imaging the ischaemic penumbra," *Current Opinion in Neurology*, vol. 17, no. 1, pp. 61–67, 2004.

[4] C. A. Mathis, B. J. Bacskai, S. T. Kajdasz, et al., "A lipophilic thioflavin-T derivative for positron emission tomography (PET) imaging of amyloid in brain," *Bioorganic and Medicinal Chemistry Letters*, vol. 12, no. 3, pp. 295–298, 2002.

[5] Y. Wang, C. A. Mathis, G.-F. Huang, et al., "Effects of lipophilicity on the affinity and nonspecific binding of iodinated benzothiazole derivatives," *Journal of Molecular Neuroscience*, vol. 20, no. 3, pp. 255–260, 2003.

[6] W. E. Klunk, Y. Wang, G.-F. Huang, M. L. Debnath, D. P. Holt, and C. A. Mathis, "Uncharged thioflavin-T derivatives bind to amyloid-beta protein with high affinity and readily enter the brain," *Life Sciences*, vol. 69, no. 13, pp. 1471–1484, 2001.

[7] J. R. Ballinger, "Imaging hypoxia in tumors," *Seminars in Nuclear Medicine*, vol. 31, no. 4, pp. 321–329, 2001.

[8] R. J. Hodgkiss, "Use of 2-nitroimidazoles as bioreductive markers for tumour hypoxia," *Anti-Cancer Drug Design*, vol. 13, no. 6, pp. 687–702, 1998.

[9] S. S. Foo, D. F. Abbott, N. Lawrentschuk, and A. M. Scott, "Functional imaging of intratumoral hypoxia," *Molecular Imaging and Biology*, vol. 6, no. 5, pp. 291–305, 2004.
[10] J. M. Hoffman, J. S. Rasey, A. M. Spence, D. W. Shaw, and K. A. Krohn, "Binding of the hypoxia tracer [$^3$H]misonidazole in cerebral ischemia," *Stroke*, vol. 18, no. 1, pp. 168–176, 1987.
[11] R. Markus, D. C. Reutens, S. Kazui, et al., "Topography and temporal evolution of hypoxic viable tissue identified by 18F-fluoromisonidazole positron emission tomography in humans after ischemic stroke," *Stroke*, vol. 34, no. 11, pp. 2646–2652, 2003.
[12] Z. Li, T. Chu, X. Liu, and X. Wang, "Synthesis and in vitro and in vivo evaluation of three radioiodinated nitroimidazole analogues as tumor hypoxia markers," *Nuclear Medicine and Biology*, vol. 32, no. 3, pp. 225–231, 2005.
[13] S. Levine and H. Payan, "Effects of ischemia and other procedures on the brain and retina of the gerbil (*Meriones unguiculatus*)," *Experimental Neurology*, vol. 16, no. 3, pp. 255–262, 1966.
[14] K. Ohno, U. Ito, and Y. Inaba, "Regional cerebral blood flow and stroke index after left carotid artery ligation in the conscious gerbil," *Brain Research*, vol. 297, no. 1, pp. 151–157, 1984.
[15] D. I. Edwards, "Nitroimidazole drugs-action and resistance mechanisms—I: mechanisms of action," *Journal of Antimicrobial Chemotherapy*, vol. 31, no. 1, pp. 9–20, 1993.
[16] D. I. Edwards, "Nitroimidazole drugs-action and resistance mechanisms—II: mechanisms of resistance," *Journal of Antimicrobial Chemotherapy*, vol. 31, no. 2, pp. 201–210, 1993.
[17] S. J. Read, T. Hirano, D. F. Abbott, et al., "The fate of hypoxic tissue on 18F-fluoromisonidazole positron emission tomography after ischemic stroke," *Annals of Neurology*, vol. 48, no. 2, pp. 228–235, 2000.
[18] S. Levine and D. Sohn, "Cerebral ischemia in infant and adult gerbils. Relation to incomplete circle of Willis," *Archives of Pathology*, vol. 87, no. 3, pp. 315–317, 1969.
[19] D. E. Levy and J. B. Brierley, "Communications between vertebro-basilar and carotid arterial circulations in the gerbil," *Experimental Neurology*, vol. 45, no. 3, pp. 503–508, 1974.
[20] K. Kahn, "The natural course of experimental cerebral infarction in the gerbil," *Neurology*, vol. 22, no. 5, pp. 510–515, 1972.
[21] T. Kirino, "Delayed neuronal death in the gerbil hippocampus following ischemia," *Brain Research*, vol. 239, no. 1, pp. 57–69, 1982.

Hindawi Publishing Corporation
International Journal of Biomedical Imaging
Volume 2007, Article ID 17131, 5 pages
doi:10.1155/2007/17131

*Research Article*

# The Advantage of PET and CT Integration in Examination of Lung Tumors

**Guangming Lu, Zhongqiu Wang, Hong Zhu, Linfeng Chang, Yingxin Chen, Jiang Wu, and Yane Zhao**

*Department of Medical Imaging, Jinling Hospital, Clinical School of Medical College, Nanjing University, Nanjing 210002, China*

Received 25 January 2007; Revised 30 June 2007; Accepted 17 July 2007

Recommended by Jing Bai

*Purpose.* To evaluate the diagnosis value of integrated positron emission tomography and computed tomography (PET/CT) with lung masses, this study emphasized the correlation between tumor size and maximum standardized uptake value (SUVmax) in selected regions of interest (ROI) of lung masses. *Material and Methods.* A retrospective analysis was performed on 85 patients with solid pulmonary lesions, all verified by pathology. The morphology, edge (speculated margins and lobule), size, density of pulmonary masses, and on-chest CT images were reviewed. The SUVmax in ROI of pulmonary masses was calculated. *Results.* Among the 85 patients with lung masses, 59 patients presented with pulmonary malignant neoplasm and 26 patients with benign lesions. The sensitivity, specificity, and accuracy were 89.8%, 61.5%, 81.2%, respectively, for PET measurement only, 88.1%, 65.4%, 81.2% for CT only, and 96.6%, 80.8%, 91.8% for PET/CT. The size of pulmonary malignant neoplasm in the 59 patients was apparently correlated with the ROI's SUVmax ($r = 0.617$, $P < .001$). However, the size of pulmonary benign mass in the 26 patients was not correlated with the SUVmax. *Conclusion.* PET/CT is of greater value in characterization of lung masses than PET and CT performed separately. The examination of lung tumor can be further specified by the correlation between the size of pulmonary malignant neoplasm and the ROI's SUVmax.



## 1. THE ADVANTAGE OF PET AND CT INTEGRATION IN EXAMINATION OF LUNG TUMORS

In recent years, the incidence and mortality of lung cancer are always ranked as the highest among all neoplasms. Mass is the principal manifestation of lung cancer, whose diagnosis is of vital clinical significance [1–5]. Early and accurate diagnosis of lung cancer is critical to its therapy. PET/CT combines the merits of both functional and anatomical imaging techniques and has been widely used in clinical examination, with a hope to make the diagnosis of neoplasm as early as possible. The current study evaluated the diagnosis value of PET/CT.

## 2. MATERIAL AND METHODS

### 2.1. Imaging acquisition

Fluorine-18-labeled fluorodeoxyglucose (18F-FDG) was produced by EBCO cyclotron facility. Radiochemical purity (>95%) of 18F-FDG was verified by analytical HPLC. All patients fasted for at least 6 hours before PET/CT examination. After ensuring a normal peripheral blood glucose level, patients received an intravenous injection of 0.2 mCi/kg of 18F-FDG, and then rested for approximately 50–60 minutes before undergoing a PET/CT scan. Image acquisition was performed using an integrated PET/CT device (Siemens Biograph Sensation 16). CT was performed from the head to the pelvic floor using a standardized protocol (120 KV, 80 mA with a slice thickness of 5 mm). PET images in early display were acquired using 3D mode for the same scanning range as CT. The acquisition time for PET was 3 minutes per bed position and 5-6 continuous positions were scanned. Delayed images of chest were acquired at 3 hours after injection of 18F-FDG. The acquisition parameters of the two PET scans are the same. PET images datasets were reconstructed iteratively using an ordered subset expectation maximization algorithm and corrected with measured attenuation correction. The SUVmax of the selected ROI in lesions was calculated. CT, PET, and PET/CT infusion images of axial, sagittal, and coronal images were obtained through a postprocessing procedure.

### 2.2. Patient data

85 patients (54 males, 31 females; age range: 36–87 years; mean age: 58 years) with lung masses were enrolled in this

Table 1: The diagnostic value of PET only, CT only, and integrated PET/CT on 85 patients with lung masses.

| Methods | Sensitivity (%) | Specificity (%) | Positive predictive value (%) | Negative predictive value (%) | Accuracy (%) |
|---|---|---|---|---|---|
| PET only | 89.8 (53/59) | 61.5 (16/26) | 84.1 (53/63) | 72.7 (16/22) | 81.2 (69/85) |
| CT only | 88.1 (52/59) | 65.4 (17/26) | 85.2 (52/61) | 70.8 (17/24) | 81.2 (69/85) |
| Integrated PET/CT | 96.6 (57/59) | 80.8 (21/26) | 91.9 (57/62) | 91.3 (21/23) | 91.8 (78/85) |

See Figures 3(a)–5(c) for further demonstration of our cases.

study. Each patient received the early 18-FDG scan described above. 70 patients underwent a second delayed scan because either their pulmonary masses could not be determined or they had suspected pulmonary malignancies. Other 15 patients did not undergo delayed 18F-FDG scan because they already had a definite diagnosis based on CT and/or early PET scan.

### 2.3. Data analysis and processing

#### 2.3.1. Semiautomatic quantification of ROI

ROI was drawn on the slice that showed clearly radioactivity aggregation. For an early scan, the SUVmax over 2.5 was regarded as positive; and for a delayed scan, the SUVmax over 2.5 or with10% increase compared to the early scan, was recognized as positive. CT images were mainly employed to examine the morphology, edge (i.e., speculated margins and lobulation), size, and density of pulmonary lesions. Metastasis derived from PET or CT was comprehensively analyzed with other clinical profiles. If a lung mass was irregular in its shape and/or its edge was poorly defined such as being spiculated, having radiating corona, umbilicated, or lobulated without benign signs of lung masses (e.g., having characteristic calcification or fat), it was regarded as malignant neoplasm. The images were interpreted by two experienced radiologists who had obtained a position higher than the rank of attending physicians. Diagnosis was determined only when a consensus was achieved. If no consensus was achieved, it would be subject to further review by the whole department. The diagnostic sensitivity, specificity, and accuracy of PET only, CT only, and PET/CT were analyzed. The correlations between tumor sizes and ROI's SUVmax were quantitatively compared.

### 2.4. Statistics

The correlations between tumor sizes and metabolism of the lesions were performed using an SPSS software (version 11.5). Pearson correlation was calculated with $P < .05$ or $P < .001$, considered as a standard of significance level or a very significant difference, respectively.

## 3. RESULTS

There were 85 patients with solid pulmonary lesions: 59 cases of malignant neoplasms, 26 cases of benign masses. Among the malignant neoplasm cases, there were 19 squamocellular carcinomas, 25 adenocarcinomas, 3 alveolar cell carcinomas, 4 small-cell nondifferentiated adenocarcinomas, 1 eosinophilic cell carcinoid, 1 adenospuamous carcinoma, 2 dual-origin carcinomas (one right and left upper lung cavernous squamocellular carcinoma and one left upper lung adenocarcinoma with right lower lung mixed carcinoma), and 4 metastases. Among the benign mass cases, there were 9 lung tuberculoses, 7 inflammatory granulomatosis, 3 chronic inflammations, 2 acute inflammations, 1 round ateletasia, 1 fungus, and 3 other benign tumors. The diagnostic values of PET only, CT only, and PET/CT for these lung masses were shown in Table 1 and Figures 3(a)–5(a). There were 10 false positive cases and 6 false negative cases (5 neoplasms with a diameter lower than 1 cm and one highly differentiated carcinoid) for PET-only imaging. 9 false positive cases and 7 false negative cases would have been found if CT-only scan was employed. The numbers of both false positive cases (5 cases) and false negative cases (2 cases) for integrated PET/CT were smaller than those for PET alone or CT alone (see Table 1 and Figures 3–5).

Figures 1 and 2 illustrate the correlations between 18F-FDG uptake and the tumor sizes. The results from a statistical analysis showed that while the sizes of pulmonary malignant tumors were significantly correlated with the ROI's SUVmax ($r = 0.617$, $P < .001$), there was no significant correlation between the ROI's SUVmax and the sizes of masses in benign lesions measured on PET/CT.

## 4. DISCUSSION

Lung masses might be classified when they are larger than 3 cm and less than 3 cm in diameter. Among the solitary pulmonary nodules with a diameter less than 3 cm, there were 33% malignant nodules, 54% inflammatory granulomatoses, 6% hamartomas, 5% isolated metastases, and 2% bronchial adenomas [3–7]. Most lung masses with a diameter larger than 3 cm were malignant [4]. To resolve differential diagnoses of lung masses based on the different types of scans still remains a challenge to radiologists.

### 4.1. The diagnostic value of PET alone for lung mass

The extent of 18F-FDG uptake can be a good reference to the property of a certain mass. The absorbances of FDG in malignant neoplasms were significantly higher than those of benign tumors. Most radiologists employed the semiautomatic quantification of SUVmax, with 2.5 as a threshold value [1, 2, 8, 9]. Tumors with SUVmax >2.5 were classified as malignant lesions. End-stage pulmonary carcinoma can be accompanied with high metabolism metastasis to pulmonary hilar lymph nodes, mediastinal lymph nodes, and other organs [9, 10]. By applying this standard,

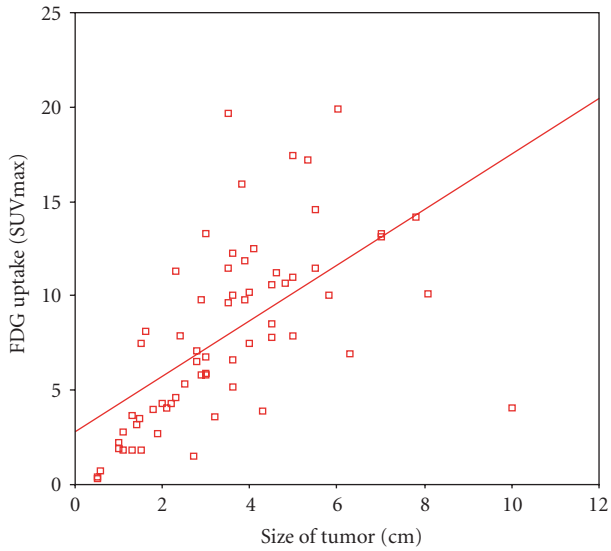


Figure 1: The correlation between FDG uptake and the sizes of 59 malignant tumors.

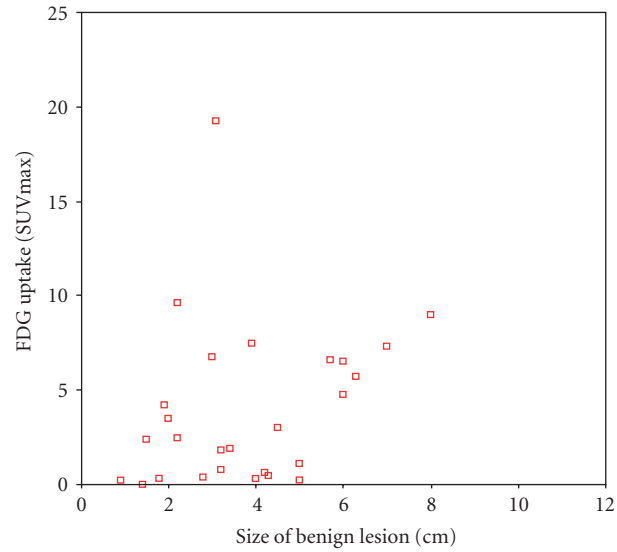


Figure 2: The correlation between FDG uptake and the sizes of 26 benign masses.

the diagnostic sensitivity, specificity, and accuracy are about 89.8%, 61.5%, and 81.2%, respectively. Dewan et al. [11] reported that the diagnostic sensitivity, specificity, and accuracy of PET for lung nodules were 95%, 87%, and 92%, respectively. In 1474 cases with solitary pulmonary nodules, the 18F-FDG PET had a diagnostic sensitivity of 96.8% and a specificity of 77.8% [12]. While discrepancy exists between our work and other reports, false positivity and false negativity exist in all groups. Tuberculosis, inflammatory pseudotumor, aspergillosis, and granulomatosis can also have an uptake of FDG and lead to false positivity. In our cases, there were 10 false positive cases, which had a lower positive predictive value of 85.2% for PET. Among the 6 false negativities, 5 were small lung cancer (diameter <10 mm), which implies that the threshold of SUVmax 2.5 needs to be modified for the diagnosis of small lung cancer with PET. In addition, dual-time-point 18F-FDG PET is necessary in order to improve the accuracy of diagnosis.

### 4.2. Diagnosis of lung mass with CT

CT scan was used to analyze the characteristics of lesions involving the location, morphology, edge (i.e., speculated margins and lobule), size, density, and enhancement manifestations after injecting contrast agent. Small lung nodules require a thin-slice CT scan protocol and/or dynamic enhancement. Although spiral CT could afford more detailed information such as intranodular calcification and blood supply of the mass, it still lacks specificity for certain lung nodules. Our results showed that the sensitivity, specificity, and accuracy of CT in the diagnosis are 88.1%, 65.4%, and 81.2%, respectively. Yi et al. [13] reported that the diagnostic sensitivity, specificity, and accuracy of lung malignant neoplasm with dynamic enhanced spiral CT are 81%, 93%, and 85%, respectively. Though its diagnostic value improved somewhat, there is still some difficulty in evaluating their cases. There were 9 false positive cases and 7 false negative cases in our CT series. The reason for this difference might be that the findings based on pathologies could have a similar CT manifestation while the same pathology might have different images. Therefore, to improve the diagnostic accuracy, other diagnostic procedures need to be integrated with CT measurements.

### 4.3. The correlation of lung mass size and its metabolism

This research showed that there was a positive correlation between the size of malignant tumor and PET/CT SUVmax ($r = 0.617$, $P < .001$). In Figure 1, there is a linear correlation between the malignant tumor size and SUVmax. Not only tumor size but also the focal metabolism should be taken into account in the diagnosis of malignant tumors with PET/CT. Especially for those with an SUVmax <2.5, lung carcinoma could not be excluded. False negativity might arise from the following reasons [6, 7, 9, 14–17].

(1) Some types of tumors, for example, bronchial alveolar cell carcinoma, carcinoid, and well-differentiated adenocarcinoma, might have a reduced metabolism, and a false negativity.

(2) Tumors smaller in diameter (<10 mm) have a low SUVmax, and they might produce partial volume effect.

(3) There are a large number of fibers inside the tumors and a low quantity of tumor cells.

(4) The patients had high blood glucose level.

Most false negativities in our series were at small foci. Great caution should be taken for the diagnostic small nodules with a diameter <10 mm since such small malignancies might have an SUVmax <2.5. Different criteria are needed to determine malignancy in nodules less than 10 mm in diameter. As shown in Figure 2, there is no correlation between the size of benign lesions and SUVmax of PET/CT. This may

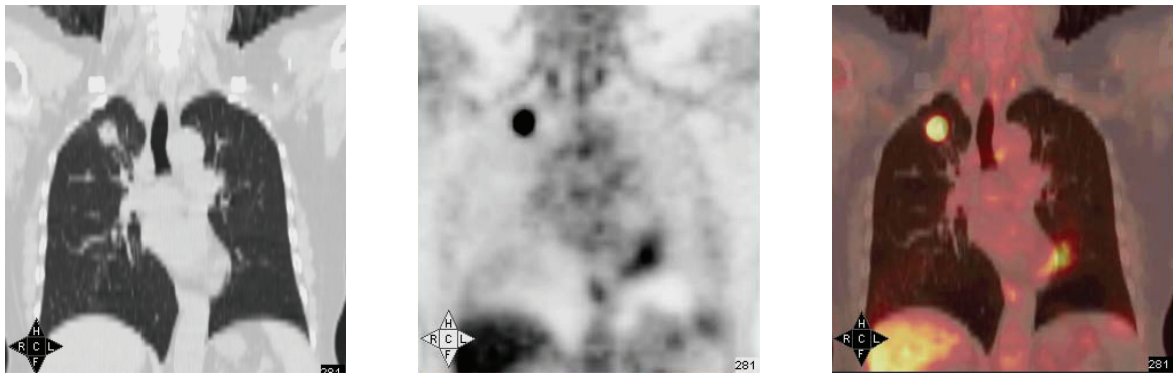

(a) (b) (c)

Figure 3: (a), (b), and (c) were from the same patient. The pathological diagnosis is right upper pulmonary squamous carcinoma. There were typical manifestations on CT, PET, and integrated PET/CT. The mass on CT is 2.4 cm × 2.5 cm. The SUVmax of early PET imaging is 7.8.

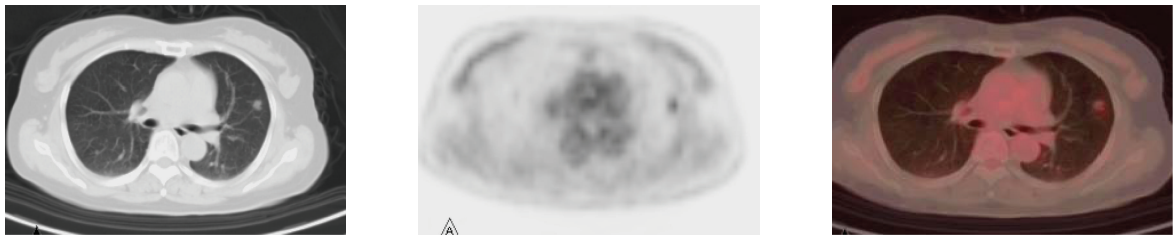

(a) (b) (c)

Figure 4: (a), (b), and (c) were from the same patient. The pathological diagnosis is left upper lung adenocarcinoma. On CT, a small module (0.9 cm × 1.0 cm) with lobulation and speculated margin was seen in the left upper lung (a). No typical manifestation was seen on PET. The SUVmax of early PET imaging was 1.9 (b). Integrated PET/CT suggested suspected lung carcinoma (c).

reflect the complexity of tumor metabolism, suggesting that the masses are not proportional to SUVmax of PET/CT. If a focus has an SUVmax >2.5, but the size of the mass is not in accordance with the SUVmax, caution should be taken to avoid false positivity. Bunyaviroch et al. [6, 7, 9, 10, 17] reported that false positivity in imaging might arise in tuberculosis, sarcoidosis, histoplasmosis, aspergillosis, and pleural mesothelioma.

### 4.4. *Diagnostic value of integrated PET/CT for lung tumor*

The diagnostic procedure of integrated PET/CT for lung masses was as follows.

(1) The metabolism of FDG should follow the standard for malignant tumors from the view of PET.

(2) Lung tumors should follow the standard of CT concerning the density, morphology, edge, and enhancement.

When either of the standards was met, lung tumor could be diagnosed. When only one of the requirements was achieved, caution should be taken. Further, inspection should pursue. When neither of the requirements was reached, lung tumor could be excluded. Yi et al. [13, 16] reported that the diagnostic sensitivity, specificity, and accuracy of integrated PET/CT for lung malignancy were 96%, 88%, and 93%, respectively, but 96.6%, 80.8%, and 91.8% in our series. Winer-Muram et al. [16, 18] reported that as compared with CT, PET/CT provided additional information, including more accurate location, differentiation of pathological and physiological uptakes, pickup of foci omitted by CT. The results from the current study showed that integrated PET/CT had higher sensitivity and specificity than CT or PET when performed separately, indicating that PET/CT may play a more important role in lung tumor diagnosis. Given the false positivity and false negativity detected, PET/CT may not be ideally specific for lung tumor [13, 15, 16, 18]. We ought to combine the information of focal metabolism, morphology, volume, and density in order to avoid false positivity and false negativity. To meet such need, the usage of different tracers, needle biopsy, or follow-up should be pursued to ensure accurate diagnosis.

## 5. CONCLUSION

The integration of PET and CT is of greater value for the diagnosis of lung masses than other methods using PET or

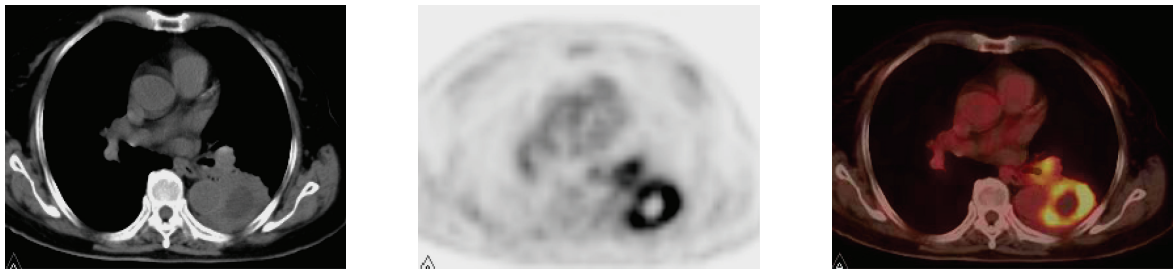

(a) (b) (c)

Figure 5: (a), (b), and (c) were from the same patient. The pathology is left lung inflammation. A big mass (5.3 cm × 5.7 cm) with lobulation and spurring was seen on CT (a). Malignant tumor was suspected on CT. False positivity was seen on PET; its early imaging SUVmax is 6.6 (b). The integrated PET/CT also suggested possible lung carcinoma (c).

CT alone. Our results showed that the size of pulmonary malignant neoplasms was correlated with ROI's SUVmax of PET/CT positively, but the size of pulmonary benign lesion was not correlated with the SUVmax. These findings indicate that PET/CT may enhance the sensitivity, specificity, and accuracy of diagnosis on lung tumors.

## ACKNOMLEDGMENT

This research was supported by the 973 program no. 2006 CB705707.

## REFERENCES

[1] M. Hickeson, M. Yun, A. Matthies, et al., "Use of a corrected standardized uptake value based on the lesion size on CT permits accurate characterization of lung nodules on FDG-PET," *European Journal of Nuclear Medicine*, vol. 29, no. 12, pp. 1639–1647, 2002.

[2] N. C. Gupta, J. Maloof, and E. Gunel, "Probability of malignancy in solitary pulmonary nodules using fluorine-18-FDG and PET," *The Journal of Nuclear Medicine*, vol. 37, no. 6, pp. 943–948, 1996.

[3] J. J. Erasmus, H. P. McAdams, and J. E. Connolly, "Solitary pulmonary nodules— part II: evaluation of the indeterminate nodule," *Radiographics*, vol. 20, no. 1, pp. 59–66, 2000.

[4] H. Nomori, K. Watanabe, T. Ohtsuka, T. Naruke, K. Suemasu, and K. Uno, "Evaluation of F-18 fluorodeoxyglucose (FDG) PET scanning for pulmonary nodules less than 3 cm in diameter, with special reference to the CT images," *Lung Cancer*, vol. 45, no. 1, pp. 19–27, 2004.

[5] C. I. Henschke, D. F. Yankelevitz, R. Mirtcheva, et al., "CT screening for lung cancer: frequency and significance of part-solid and nonsolid nodules," *American Journal of Roentgenology*, vol. 178, no. 5, pp. 1053–1057, 2002.

[6] H. Nomori, K. Watanabe, T. Ohtsuka, T. Naruke, K. Suemasu, and K. Uno, "Visual and semiquantitative analyses for F-18 fluorodeoxyglucose PET scanning in pulmonary nodules 1 cm to 3 cm in size," *The Annals of Thoracic Surgery*, vol. 79, no. 3, pp. 984–988, 2005.

[7] P. De Leyn, "Invited commentary," *The Annals of Thoracic Surgery*, vol. 79, no. 3, p. 989, 2005.

[8] A. Matthies, M. Hickeson, A. Cuchiara, and A. Alavi, "Dual time point $^{18}$F-FDG PET for the evaluation of pulmonary nodules," *Journal of Nuclear Medicine*, vol. 43, no. 7, pp. 871–875, 2002.

[9] Y. Hashimoto, T. Tsujikawa, C. Kondo, et al., "Accuracy of PET for diagnosis of solid pulmonary lesions with $^{18}$F-FDG uptake below the standardized uptake value of 2.5," *The Journal of Nuclear Medicine*, vol. 47, no. 3, pp. 426–431, 2006.

[10] T. Bunyaviroch and R. E. Coleman, "PET evaluation of lung cancer," *The Journal of Nuclear Medicine*, vol. 47, no. 3, pp. 451–469, 2006.

[11] N. A. Dewan, C. J. Shehan, S. D. Reeb, L. S. Gobar, W. J. Scott, and K. Ryschon, "Likelihood of malignancy in a solitary pulmonary nodule: comparison of Bayesian analysis and results of FDG-PET scan," *Chest*, vol. 112, no. 2, pp. 416–422, 1997.

[12] M. K. Gould, C. C. Maclean, W. G. Kuschner, C. E. Rydzak, and D. K. Owens, "Accuracy of positron emission tomography for diagnosis of pulmonary nodules and mass lesions: a meta-analysis," *Journal of the American Medical Association*, vol. 285, no. 7, pp. 914–924, 2001.

[13] C. A. Yi, K. S. Lee, B.-T. Kim, et al., "Tissue characterization of solitary pulmonary nodule: comparative study between helical dynamic CT and integrated PET/CT," *The Journal of Nuclear Medicine*, vol. 47, no. 3, pp. 443–450, 2006.

[14] G. R. Conrad and P. Sinha, "Narrow time-window dual-point 18F-FDG PET for the diagnosis of thoracic malignancy," *Nuclear Medicine Communications*, vol. 24, no. 11, pp. 1129–1137, 2003.

[15] S.-N. Yang, J.-A. Liang, F.-J. Lin, A. S. Kwan, C.-H. Kao, and Y.-Y. Shen, "Differentiating benign and malignant pulmonary lesions with FDG-PET," *Anticancer Research*, vol. 21, no. 6 A, pp. 4153–4157, 2001.

[16] R. E. Coleman, D. Delbeke, M. J. Guiberteau, et al., "Concurrent PET/CT with an integrated imaging system: intersociety dialogue from the joint working group of the American College of Radiology, the Society of Nuclear Medicine, and the Society of Computed Body Tomography and Magnetic Resonance," *The Journal of Nuclear Medicine*, vol. 46, no. 7, pp. 1225–1239, 2005.

[17] T. Hara, N. Kosaka, T. Suzuki, K. Kudo, and H. Niino, "Uptake rates of $^{18}$F-fluorodeoxyglucose and $^{11}$C-choline in lung cancer and pulmonary tuberculosis: a positron emission tomography study," *Chest*, vol. 124, no. 3, pp. 893–901, 2003.

[18] H. T. Winer-Muram, "The solitary pulmonary nodule," *Radiology*, vol. 239, no. 1, pp. 34–49, 2006.